MODELING AND DESIGN OF ULTRA-WIDEBAND ARRAYS

Matteo Ciattaglia

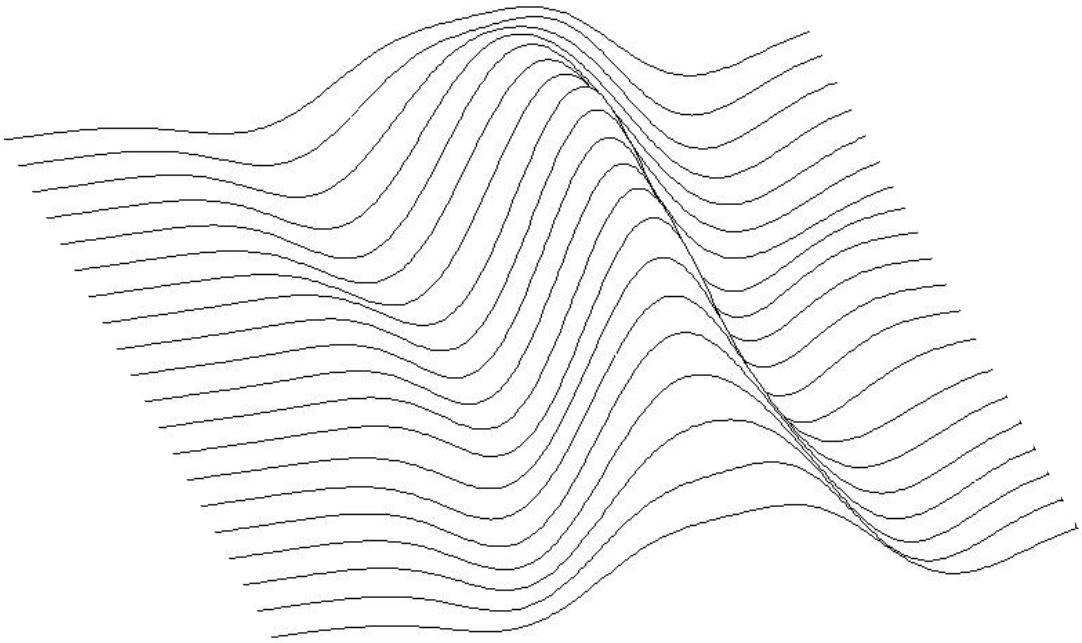

Advisor

Gaetano Marrocco

UNIVERSITÀ DEGLI STUDI DI ROMA TOR VERGATA
FACOLTÀ DI INGEGNERIA
Dipartimento di Informatica, Sistemi e Produzione

Dottorato di Ricerca in
GEOINFORMAZIONE

Modeling and Design of Ultra-Wideband Arrays

Tesi di Dottorato di

Matteo Ciattaglia

Relatore

Gaetano Marrocco

Ciclo XIX
Anno Accademico 2005-2006

[2]Vanità delle vanità, dice Qoèlet,
vanità delle vanità, tutto è vanità.
[3]Quale utilità ricava l'uomo da tutto l'affanno
per cui fatica sotto il sole?
Qoèlet 1, 2-3

…to my wife…

Contents

1 Introduction **7**

2 UWB Generalities **9**
2.1 History 9
2.2 Advantages 10
2.3 Applications 13
2.3.1 Communications and antennas networks 13
2.3.2 Position location and tracking 14
2.3.3 Radar 15
2.4 Summary 16

3 The domain of Time **19**
3.1 Domain of Analysis and Synthesis 19
3.2 Tools 20
3.2.1 Gaussian Waveforms 20
3.2.2 Hermite Functions 21
3.2.3 Radon Transform 24
3.2.4 Transient waveform representation 25
3.2.5 Convolution and Deconvolution 27

4 Pulsed arrays **29**
4.1 The principle of pattern convolution 29
4.2 Pulsed vs. Monochromatic Arrays 30
4.3 Requirements for the characterization of pulsed arrays 34

5 Efficient Characterization of Radiating Elements **37**
5.1 Introduction 37
5.2 Aperture Antennas 39
5.2.1 TD aperture effective height 39
5.2.2 Numerical representations of the aperture impulse response 40
5.2.3 Approximate calculation of time domain effective height 42
5.2.4 Discussion about numerical complexity 45
5.2.5 Numerical Analysis 46

5.3 Directive antennas 53
5.3.1 Statement of the problem 53
5.3.2 Hermite processing of the time-varying field 53
5.3.3 Impulse response 57
5.3.4 Computational Issues 57
5.3.5 Numerical Examples 59

6 TD Analysis of Couplings in Pulsed Arrays 71
6.1 Introduction 71
6.2 Basic definitions: impulse response operator and TD array factor 72
6.3 TD active array factor and active element factor 74
6.4 Investigation on coupling echoes 75
6.4.1 Coupling for Dirac pulse input signals 76
6.4.2 Coupling for finite-duration pulses 80
6.5 A fullwave example 85

7 Synthesis of Pulsed Arrays 91
7.1 Introduction 91
7.2 Definition of the TD synthesis problem 93
7.3 Intersection finding problem 95
7.4 Alternating projections 95
7.5 Radon inversion 97
7.6 Excitation Mapping 99
7.7 Numerical Examples 102
7.7.1 Single monocycle pulse 102
7.7.2 Simultaneous monocycle pulses 107

8 Conclusions 111

A Details on aperture effective height 113
A.1 Details on the definition of TD aperture effective height 113
A.2 Calculation of the $\boldsymbol{h}^R_{p,\infty}$ integral in (5.10) 113
A.3 Modal space factors 114
A.3.1 Modal space factors for rectangular apertures 114
A.3.2 Modal space factors for circular apertures 115

List of Acronyms

Acronym	Meaning
AH	Associated Hermite
AHF2	Two-Dimensional Associated Hermite Functions
CDMA	Code Division Multiple Access
CF	Complete Fitting
CRH	Circular Ridged Horn
DS	Direct Sequence
EIRP	Effective Isotropic Radiated Power
EM	Electromagnetics
FCC	Federal Communications Commission
FD	Frequency Domain
FDTD	Finite Difference Time Domain
FF	Far Field
FDMA	Frequency Division Multiple Access
GPS	Global Positioning System
HR	Hermite Rodriguez
IF	Incomplete Fitting
LTI	Linear Time Invariant
ME	Moment Expansion
N2F	Near To Far Field
NB	Narrowband
NF	Near Field
OFDM	Orthogonal Frequency DivisionMultiplexing
PSD	Power Spectral Density
RF	Radio Frequency
SEM	Singularity Expansion Method
SLL	Side Lobe Level
SVD	Singular Value Decomposition
TD	Time Domain
TE	Transverse Electric
TM	Transverse Magnetic
UWB	Ultra Wide Band

Chapter 1

Introduction

Several applications of UWB technology have been recently proposed for communications, radar, precise positioning and tracking. The development of new system components, in particular antennas, requires efficient modeling tools. The extremely large bandwidths of the systems encourage the use of time-domain formulations. In particular, the objective of my research activities has been to develop efficient methods for the transient characterization of pulsed arrays. Pulsed arrays consist of an arrangement of Ultra-Wideband antennas sourced by baseband carrier-free input signals, usually with a pure delay-line as beamforming network, in order to control the main lobe direction. Their radiating performances are pretty different from narrowband arrays and time-domain extensively replaces the conventional frequency domain way to approach the array modeling. In the previous years, this new approach has already permitted first investigations on some topics of pulsed arrays, like grating lobes cancellation, side lobes mitigation and sparse array design. However tools for the complete transient characterization of pulsed arrays still lack requiring:

1. the efficient analysis of the isolated radiating elements that constitute the array;

2. the analysis of the effects of their spatial displacement on the radiating performances of the array;

3. the synthesis of their transient excitations to realize a desired far field of the array.

Each of these subjects has been developed during my PhD activity research and reported in the following chapters. After some historical notes on UWB technology, Chapter 2 introduces the advantages of the technology as well as its current and future applications. Chapter 3 compares the two possible domains of analysis and synthesis of UWB systems and some "tools" (most

used waveforms, transformations, operators, representations), useful in time-domain analysis and frequently used in the rest of the work, are here presented. An introduction on pulsed arrays theory is provided in Chapter 4 and their main features are briefly described.

Chapters 5 to 7 present innovative methods proposed and developed in this research activity to characterize pulsed arrays following the three items previously introduced.

The scope of the study presented in Chapter 5 was to develop suitable representations of signals and electromagnetic fields to efficiently characterize UWB antennas. In particular, two techniques for the efficient modeling of radiating elements by means of suitable spatial and temporal expansions are introduced. One technique is suitable for aperture antennas, the other for antennas of more general shape, such as UWB dipoles, TEM horn and non canonical-aperture horns. These expansions permit to capture the complete spatial and temporal behavior of the antenna (its effective height) by a small set of parameters thus expressing its response by semi-analytical representations. The proposed techniques are suited to strengthen any existing time-domain numerical solver and to perform more easily UWB array analysis and synthesis.

Chapter 6 presents a simple physical model of the time domain coupling for UWB arrays aimed to identify the role of the scan angle, input signal duration, repetition rate of the input pulse train and impulse response of the single antenna. Expressions for the time domain active array and element patterns are retrieved and an investigation on coupling echoes and their distorting effect on the main signal permits to obtain conditions to reduce coupling even in compact configurations with very small inter-element distances.

Chapter 7, finally, presents a synthesis technique to compute the amplitude, the transient behavior and the relative delay of the input signals of UWB arrays in order to shape the radiated field in accordance to a given mask in the angular and temporal domains. The technique extends the method of alternating projections to the time domain array synthesis: in particular it consists of iterative projections of the radiated pattern onto the desired pattern mask and of the obtained excitations onto a physical set of excitations. Thanks to this second projection, the proposed technique provides input currents which are physically realizable by means of a beamforming network which will be shown in the chapter.

Each topic is developed presenting a theoretical section and some numerical examples to validate methods and investigate the phenomena, followed by some discussions on the results.

Chapter 2

UWB Generalities

2.1 History

The very first radio experiments of Hertz and Marconi at the end of the 19th century were, by accident, UWB because the transmitters of the time were spark-gap devices that emitted wideband and noisy signals. The receivers and the antennas in use at that time could not efficiently gather that wideband energy, hence high levels of powers were required to achieve desired ranges. Large bandwidths and high powers meant spectrum sharing problems and interference: these experiments necessarily cleared the way for narrowband (NB) electromagnetics (EM). The ideal waveform was a signal with a bandwidth as narrow as the information to be carried. Naturally the first regulations were approved and they defined rules to make radio signals as narrowband as possible. In this way radio services were separated by wavelength, and this led to the assignement of higher and higher frequencies in the radio spectrum under the pressure of new radio services. Nevertheless the advantages of wider bandwidths were gradually discovered; Shannon in 1948 formulated his famous capacity equation

$$C = B \log \left(1 + \frac{S}{N}\right) \tag{2.1}$$

stating that the capacity C of the radio channel can be increased linearly by increasing the signal bandwidth B or logarithmically by increasing the signal to noise ratio S/N. Shannon's observations led to "spread spectrum" modulation in which the signals are intentionally spread, using a special family of digital codes, to many times their information bandwidth. Spread-spectrum technology applied in recent times to cellular telephone systems, requiring a change in spectrum regulation policy: a block of spectrum needed to be allocated and shared by multiple users with overlapping signals across the entire band, separated by coding rather than by frequency channels (Code Division Multiple

Access, CDMA). The "bandwidth sharing" approach reaches its climax with the advent of UWB, "the modern art of reusing previously allocated RF bands by hiding signals under the noise floor" [3]. This kind of approach has been explored throughout the last half of the 20th century, above all with experimentations and development in wideband impulse radar transmissions, the real forerunner of modern UWB, regulated in spectrum by special waivers for their security and safety-of-life applications. The enduring interest of radar-world in wide bandwidth was motivated both to resolution and penetration capabilities of large bandwidth with low frequency components. Advances in time-domain electromagnetic and in microwave components were also required to enable a real development of UWB technology. In 1957 Esaki invented the tunnel diode which, with its extremely wide bandwidth, permitted not only subnanosecond pulse generation, but also could be used as a sensitive thresholding device for the detection of short-pulse waveforms. Some years later, in the early 1960s, the first works on time-domain electromagnetics appeared [4], where the transient behavior of certain classes of microwave networks was described by examining their characteristic impulse response, followed by works investigating the intrinsic properties of materials and experimental analysis and design of radiating and receiving elements. With all this building blocks in place, numerous applications of short-pulse technology were developed (as well as they are being developed nowadays), not only for safety applications (Ground Penetrating Radars, Through-the-wall imaging, medicine), but also for commercial applications (like short range radar sensing, communications, metrology, precision positioning and tracking), leading to the necessity of a regulation. A lot of work is going on to regulate UWB: actually almost the totality of UWB applications must have a bandwidth contained between $3.1GHz$ and $10.6GHz$ and an EIRP at power levels commensurate with those of unintentional emitters, as shown in Fig.2.2. Interference of UWB applications with existing services in the assigned bandwidth is actually the object of many studies.

2.2 Advantages

UWB technology is commonly referred to as "carrier-free", "baseband", "impulse" or "pulsed", reflecting the fact that the underlying signal generation strategy is the result of a broad-band extremely fast rise time step or impulse. An UWB transmitter is defined as an intentional radiator that, at any point in time, has a fractional bandwidth equal to or greater than 20% or has a bandwidth equal to or greater than $500MHz$, regardless of the fractional bandwidth [6]. The energy is therefore spread out over the whole bandwidth implying, typically, very low power spectral densities ($PSD = P/B$, where P

FIGURE 2.1. Illustration of Marconi in St. Johns, Newfoundland, receiving the first transatlantic radio signal from Poldhu in Cornwall in 1901.

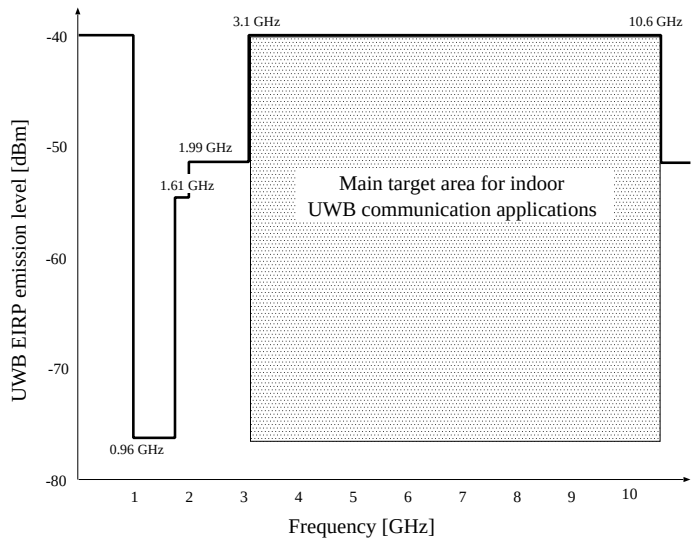

FIGURE 2.2. Spectral mask mandated by Federal Communications Commission for indoor UWB systems

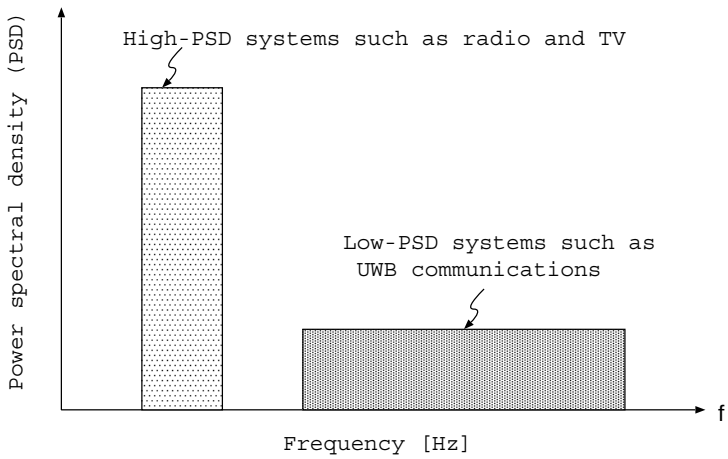

FIGURE 2.3. Power Spectral Density of NB and UWB systems

is the transmitted power and B is the signal bandwidth), as shown in Fig.2.3. All the advantages of UWB technology are associated to either, or both, the large badwidth or the low power spectral density.

A set of potential advantages of UWB technology is listed below. Obviously each advantage is not inherent in the technology, but depends on the way the signal is generated, modulated, transmitted, received and processed.

- Multipath Immunity: if the transmitted pulses can be resolved in the time domain, the effects of multipath, such as inter-symbol interference, can be mitigated, because of the extremely short pulse widths;

- Interference Resistance: the ultrawide bandwidth of the signal enhances a good immunity to narrowband interferers, since they disturb only a little portion of the information bandwidth; furthermore, as for multipath, the short duration of the radiated pulse makes the signals easily resolvable in time and separable from interference waveforms (decrease of pulse-on-pulse probabilities);

- Penetration: the attenuation factor of an electromagnetic wave in a lossy medium is frequency-dependent (typically inversely proportional to the wavelength of the signal), hence UWB pulses low-frequency components enable the signals to propagate effectively through materials, such as ground, bricks, cement;

- Range accuracy and resolution: the short spatial extent of the transmitted waveforms enables higher range measurement accuracy and range resolution ($c\tau/2$, if c is the wave velocity and τ is the signal duration);

- Speed of data transmission: From Shannon equation (2.1) one of the greatest advantages for UWB applications in communications is its high data rate. Using the traditional measure of spectral capacity [bits/Hz] (in use for narrowband systems), UWB has very low spectral capacity compared with existing systems because of its huge bandwidth; when comparing in terms of spatial capacity (defined as the maximum data rate of the system divided by the area over which the system can transmit), UWB is instead extremely efficient;
- Low interference: the signal appears to be very low-level background noise to an unintended narrowband receiver;
- Low probability of being intercepted: since the power of the UWB signal is under the noise floor, the probability that the signal is intercepted by other systems is lower than in conventional narrowband systems.

2.3 Applications

Applications of UWB technology are in continuous evolution, trying to exploit one or more of the previously described advantages. The applications of present and close-future times can be distributed among four categories:

- Communications and antennas networks
- Position location and tracking
- Radar

However, hybrid applications are possible, like for example UWEN (UWB Wireless Embedded Network), an hybrid tracking and communications network, developed for outdoor entertaining activities, consisting of a set of antennas in known positions linked to the user antenna by a peer to peer connection. In the following sections a brief description of each application is presented and, where applicable, the allowed frequency bandwidths assigned by the Federal Communications Commission (FCC) will be indicated.

2.3.1 Communications and antennas networks

UWB communications applications exploit low power and high capacity among the features of UWB technology. A group of applications which require low data rates consists in replacing with wireless links a lot of wired connections which result expensive and/or unhandy. Possible examples are: wireless connection of numerous devices in a shared and limited space (like a PC with its peripherals, see Fig.2.4), antenna networks to secure home, automobiles and

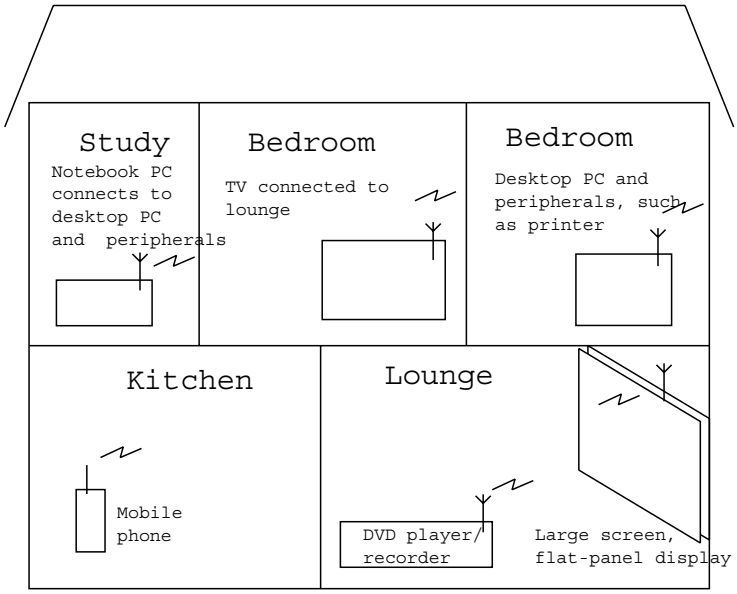

FIGURE 2.4. An example of a possible home-networking setup using UWB

other properties, wireless links in medical situations to determine pulse rate, temperature and other critical life signs. The advantages of UWB here are low cost, low interference in a crowded scenario, limited constraints derived by non line of sight communication. A second group of communications applications requires high data rates: high-density multimedia applications, such as multimedia streaming in "hot-spots" like airports, shopping centers or multi-dwelling units, downloading of video movie purchase or rental and in general wireless links among devices with low complexity, low power consumption, low multipath fading and high data rates to provide a multitude of services (the so called Personal Area Network, PAN). The devices for communications applications must operate in the frequency band $3.1 - 10.6GHz$, only indoor or for peer-to-peer operation with hand held devices.

2.3.2 Position location and tracking

Large-scale location and tracking has become very useful in a variety of applications, for example with GPS and, hopefully, with Galileo. Though UWB is not a suitable solution for outdoor location because of the too small ranges allowed by power constraints, it is an excellent solution for short-distance location applications. UWB implementations are an adjunct to global positioning systems (see Fig.2.5) that allow the precise determination of location and even-

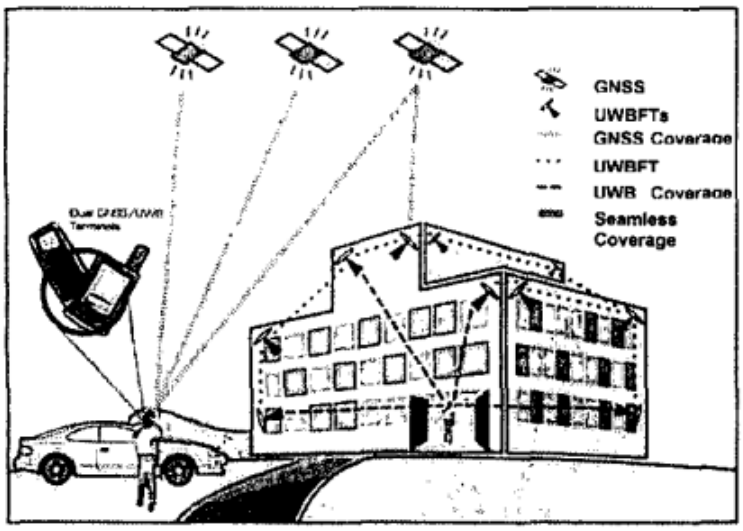

FIGURE 2.5. An example of a possible UWB positioning system

tually the tracking of moving objects within an indoor space to an accuracy of several centimeters, thanks to the large bandwidth that permits to obtain high performances even in a rich multipath channel like the indoor one. The position location applications can be safety-of-life or security applications, like finding people position in a variety of situations, including fire fighters in a burning building, police officers in distress, an injured skier on a ski slope, injured hikers in a remote area, children lost in the mall or amusement park. With advanced tracking mechanisms, not only the item locations but also their movements can be followed accurately. Possible applications are: increased inventory control in warehouses, smart homes obtained combining UWB localizers with home appliances such s TV's, ovens, lamps, etc. In general, UWB systems for position location and tracking can work in complex environments were there are many people, assets and interactions, such as hospitals, distributed workplaces, houses, training centers [7], [8]. In each application, the network roughly consists of a group of fixed antennas (directional or not) that determine the position of the mobile terminals in the indoor area.

2.3.3 Radar

The increased target information from UWB radars results from the short spatial resolution produced by the large bandwidth. The fine resolution feature resolves the target return into signals scattered by different target components to form a target image. The resulting target image carries informations about the target structure [9]. Possible applications of UWB radar imaging are:

- Ground Penetrating Radars (GPR) ($f < 960MHz$ or $3.1GHz < f < 10.6GHz$): they operate in contact with, or within close proximity of, the ground for the purpose of detecting or obtaining the images of buried objects, for law enforcement, fire and rescue organizations, scientific research institutions, commercial mining companies and construction companies;

- Wall Imaging Systems ($f < 960MHz$ or $3.1GHz < f < 10.6GHz$): they are designed to detect the location of objects contained within a wall, for the same companies, organizations and institutions of GPR;

- Through-wall Imaging Systems ($f < 960MHz$ or $1.99GHz < f < 10.6GHz$): they detect the location or movement of people or objects that are located on the other side of a structure such as a wall, law enforcement, fire and rescue organizations (Fig.2.6).

- Medical Imaging Systems: they can be used for a variety of health applications to see inside the body of a person or animal.

Other UWB non imaging radar systems are vehicular radar systems ($22GHz < f < 29GHz$), which use directional antennas on terrestrial transportation vehicles in order to detect the location and movement of objects near a vehicle, enabling features such as near collision avoidance, improved airbag activation and suspension systems that better respond to road conditions. Another UWB non imaging radar system application is for surveillance ($1.99GHz < f < 10.6GHz$), used to establish a stationary RF perimeter field to detect intrusion of people or objects.

2.4 Summary

Current research on UWB technology refers to:

- Radio channel modeling;

- Development of new technologies;

- Development of a first generation of products for most of the applications presented in the previous chapter.

The wide group of UWB antennas modeling can be included within the second set of studies, where my PhD research activity is placed. For the rest of the work, therefore, the interest will be focused on the radiating part of the UWB technology (which mainly includes antennas and arrays).

FIGURE 2.6. UWB through-wall radar can determine the likely location of building occupants

Chapter 3

The domain of Time

3.1 Domain of Analysis and Synthesis

The analysis and synthesis of a UWB radiating system (an antenna or an array) can be performed either in the time domain or in the frequency domain. Each of these methods has its own advantages and disadvantages, depending mainly on the bandwidth within which the system has to be characterized. For example, typical techniques proposed to access the radio channel in UWB commercial applications include either new strategies (DS-UWB, Time Division/FDMA) or variants of more conventional (OFDM) one [1].

Direct-Sequence (DS) UWB and Time Division / Frequency Division techniques access the radio with true UWB signals, with at least a bandwidth of $1.5GHz$ for the first and $700MHz$ for the second. The Orthogonal Frequency Division Multiplexing, instead, accesses the medium through 128 channels each occupying about $4MHz$ of spectrum. Despite the differences in the occupation of the bandwidth, all of these techniques are included in the broad definition promulgated by FCC for the UWB technology. A UWB system that uses the first two techniques can be efficiently characterized using a time-domain approach, because of both the large bandwidth occupation and of probable requirements of knowledge of the transient response of the system. The advantages of the time-domain approach are in fact the availability of the complete transient response of the system (providing a physically transparent representation of the system) and, by Fourier Transformation, of the complete frequency-domain behavior of the system, at the cost of more complex formulations and larger sets of data to be stored (typically the time domain formulation involves integral operators). Conversely, the frequency domain approach is useful for the characterization of limited portions of the spectrum of the system, typically taking advantage in terms of computational times and simpler formulations, for example for the near to far field transformation, for the array analysis and synthesis or for a transmit/receive system evaluation.

As well known, the time and frequency domains are related by the Fourier transformation and anti-transformation. Given a time-domain function $f(t)$, the transformation pair with its frequency-domain representation $F(\omega)$ are

$$F(\omega) = \int_{-\infty}^{\infty} f(t)e^{j\omega t}dt \tag{3.1}$$

$$f(t) = \frac{1}{2\pi}\int_{-\infty}^{\infty} F(\omega)e^{-j\omega t}d\omega$$

3.2 Tools

In the following sections some mathematical "tools" (most used waveforms, transformations, operators, representations), useful in time-domain analysis and frequently used in the rest of the work, are presented.

3.2.1 Gaussian Waveforms

The Gaussian waveforms are a class of waveforms with a definition similar to the Gauss function

$$G(x) = \frac{1}{\sqrt{2\pi\sigma^2}}e^{-x^2/2\sigma^2} \tag{3.2}$$

where σ is the standard deviation. The generator of the Gaussian waveforms is a Gaussian pulse

$$g_1(t) = K_1 e^{-(t-\tau)^2/2T^2} \tag{3.3}$$

where $-\infty < t < \infty$, T is a time scaling factor affecting the signal duration, τ determines the signal temporal position and K_1 is a constant which determines the energy of the signal. Further waveforms can be created by differentiation of the Gaussian pulse. A Gaussian monocycle is the first derivative of $g_1(t)$, while the Gaussian doublet is the second derivative. The three presented Gaussian waveforms are shown in Fig.3.1 together with their Fourier Transforms, with parameters $T = 0.35ns$ and $\tau = 2ns$.

The Gaussian waveforms are useful for

- Modeling the excitation of UWB systems: the Gaussian pulse and its derivatives can be simply realized using a pulse generator and some differentiator circuit;

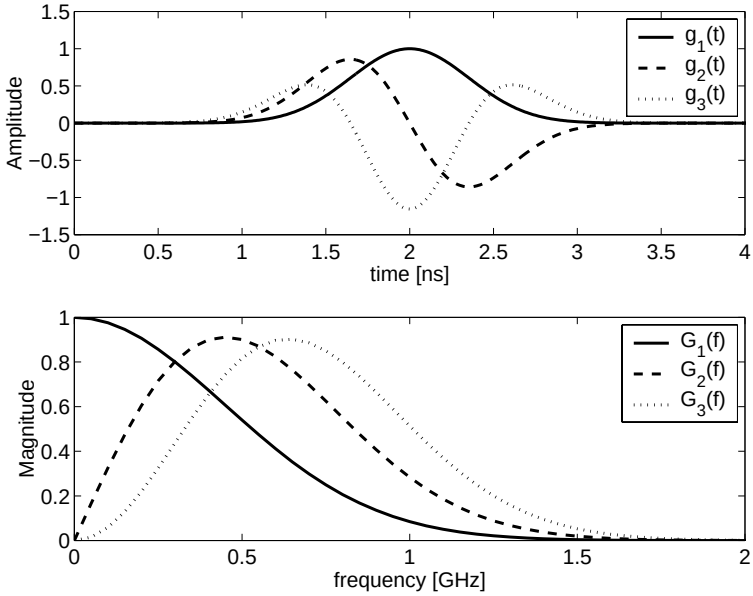

FIGURE 3.1. top: Gaussian pulse, moncycle and doublet in the time domain; bottom: Gaussian waveforms in the frequency domain. The three waveforms have equal energy

- Numerical analysis of radiating elements: a Gaussian waveform is the typical signal excitation of commonly used electromagnetic simulation tools, such as the FDTD [10], because of its large bandwidth that permits a broadband analysis of the antenna response.

3.2.2 Hermite Functions

The weighting and scaling of Hermite polynomials [12] with an appropriate Gaussian waveform produces two possible families of parametric orthogonal basis functions with essentially compact time support, the Hermite-Rodriguez (HR) and the Associated Hermite (AH). These functions have been used for the compact representation of multi-dimensionale signals (in image processing [13], in biomedical research [14], in electromagnetism [15]), for the excitation signal of UWB systems ([16], [2]) as well as for the representation of spatial behavior of electromagnetic far and near fields, as it will be shown in the following chapters. A monodimensional signal $f(t)$ can be expanded into a series by means of HR or AH representation as

$$f(t) = \sum_{n=0}^{\infty} \alpha_{\lambda,n} w_{\lambda,n}(t) \tag{3.4}$$

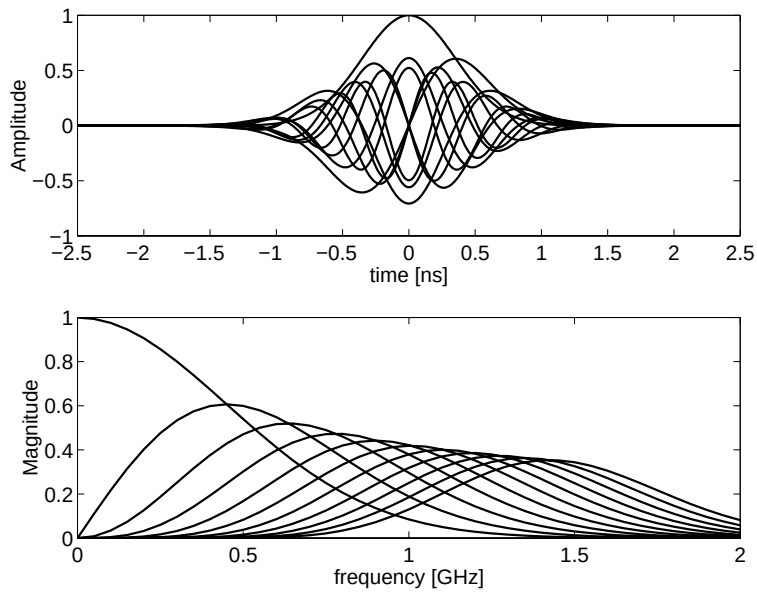

FIGURE 3.2. top: Hermite-Rodriguez functions of order 0 to 10, $\lambda = 0.5ns$; bottom: Magnitude of their Fourier Transforms. The plots are normalized to the maximum of the 0-order function

where $w_{\lambda,n}(t)$ can be the set of the HR or AH functions, as defined in the next sections.

Hermite-Rodriguez Series Expansion

The family of Hermite-Rodriguez functions is defined as

$$w_{\lambda,n} = \frac{1}{\sqrt{2^n n!}} H_n(t/\lambda) \frac{1}{\sqrt{\pi}\lambda} e^{-t^2/\lambda^2} \qquad n \in [0, \infty) \tag{3.5}$$

where n is the order of the function, λ is a width parameter and $H_n(t)$ are the Hermite polynomials. This set of functions constitues an orthogonal basis with respect to the inner product

$$< w_{\lambda,n}, w_{\lambda,k} >= \sqrt{\pi}\lambda \int_{-\infty}^{+\infty} w_{\lambda,n}(t) w_{\lambda,k}(t) e^{t^2/\lambda^2} dt \tag{3.6}$$

which is zero for $n \neq k$. The functions of order zero to three and their Fourier Transform are shown in Fig.3.2, normalized to the maximum of the 0-order function and with $\lambda = 0.5ns$.

The width parameter λ has to be carefully chosen to obtain a good approximation of the signal with a minimum number of terms. The more important

properties are

- HR functions can be computed recursively;
- HR functions have compact support;
- All the functions of order $n > 0$ have zero mean;
- if $f(t)$ is expanded using the parameter λ and coefficient $\alpha_{\lambda,n}$, then $g(t) = f(kt)$ is expanded using $\mu = \lambda/k$ and $\beta_{\mu,n} = \alpha_{\lambda,n}/k$;
- the HR function of order n is proportional to the $n-th$ derivative of a Gaussian function, as can be noted by comparing Fig.3.2 with Fig.3.1.

For a detailed description of the properties refer to [14].

Associated Hermite Series Expansion

The family of Associated Hermite functions is defined as

$$w_{\lambda,n} = \frac{1}{\sqrt{2^n n!}} H_n(t/\lambda) \frac{1}{\sqrt{\sqrt{\pi}\lambda}} e^{-t^2/2\lambda^2} \qquad n \in [0, \infty) \tag{3.7}$$

This set of functions constitues an orthonormal basis with respect to the inner product

$$< w_{\lambda,n}, w_{\lambda,k} >= \sqrt{\pi}\lambda \int_{-\infty}^{+\infty} w_{\lambda,n}(t) w_{\lambda,k}(t) dt \tag{3.8}$$

which is zero for $n \neq k$. The first functions of order zero and their Fourier Transform are shown in Fig.3.3.

The more important properties are

- AH functions can be computed recursively;
- The support of the AH functions is a function of the order N (see top of Fig.3.3);
- The AH functions of order zero and all AH functions of even order have nonzero mean value;
- the AH functions are isomorphic with respect to their Fourier Transform $\mathcal{F}\{u_{\lambda,n}(t)\} = (-j)^n u_{\mu,n}(f)$, as can be noted from Fig.3.3.

For a detailed description of the properties refer to [14].

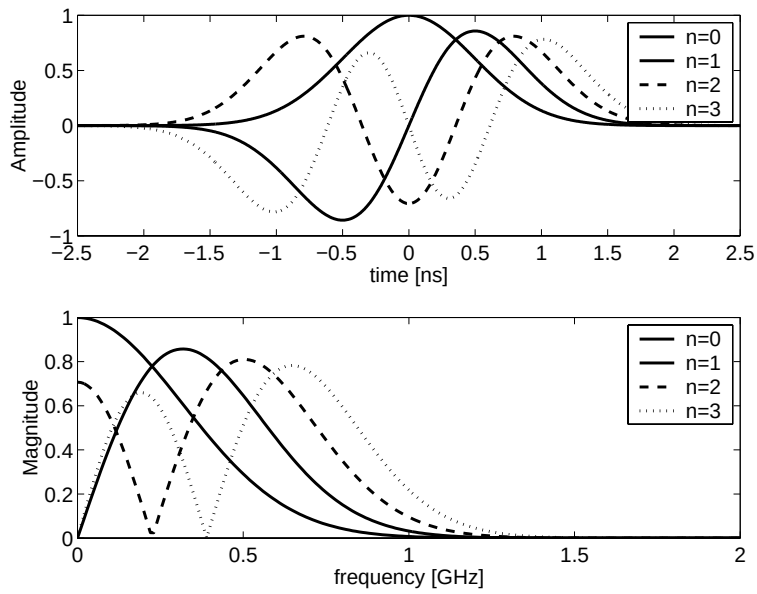

FIGURE 3.3. top: Associated Hermite functions of order 0 to 3, $\lambda = 0.5ns$; bottom: Magnitude of their Fourier Transforms. The plots are normalized to the maximum of the 0-order function

3.2.3 Radon Transform

The Radon Transform [17] $\check{g}(p,\tau)$ of a continuous two-dimensional function $g(x,y)$ is found by stacking or integrating values of g along slanted lines. The location of the lines is determined from the line parameters: slope p and line offset τ.

$$\check{g}(p,\tau) = \int_{-\infty}^{+\infty} g(x, px+\tau)dx \tag{3.9}$$

The transform (3.9) represents the projection of the function $g(x,y)$ on the set of parallel lines $px+\tau$ (Fig.3.4); $\check{g}(p,\tau)$ can be interpreted as the superposition of several events with energy concentrated along a set of parallel lines: the Radon Transform performs a mapping of these events onto a new space [18], thus allowing identification and separation.

The definition of Eq.3.9 is used with seismics applications and is also known as Slant Stack Transform. The Radon Transform is well suited for image processing, and it will be used here because it represents the radiation equation in the far field of a continuous source or of an array of radiating elements, when written in its discrete version

$$\check{g}(p_k,\tau_h) = \sum_{m=0}^{M-1} g(x_m, p_k x_m + \tau_h) \tag{3.10}$$

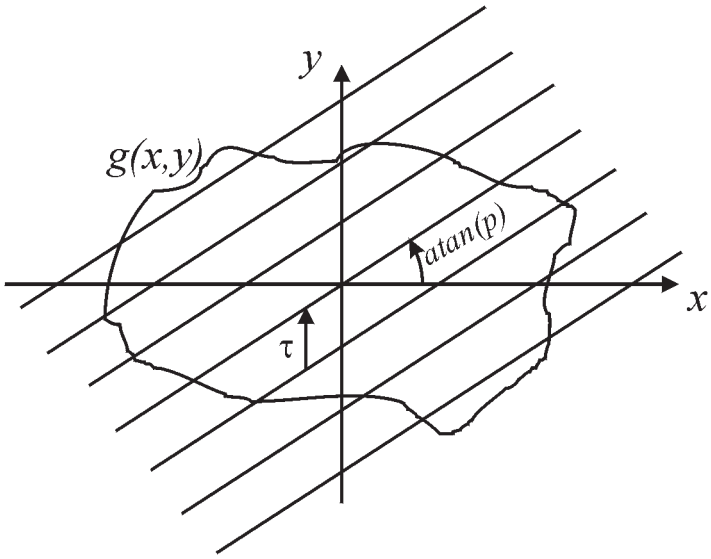

FIGURE 3.4. Radon Transform of the function $g(x, y)$

The role of the Fourier Transform in the frequency domain can hence be associated to the role of the Radon Transform in the time domain. The Radon Transform satisfies the following properties:

- linearity: the Radon transform of a weighted sum of functions is the same weighted sum of the individually Radon transformed functions
- shifting: the Radon Transform of the function $g(x-x_0, y-y_0)$ is $\check{g}(p, \tau - y_0 + px_0)$
- scaling: the Radon Transform of the function $g(x/a, y/b)$ is $a\check{g}(pa/b, \tau/b)$

As for every projection operator, also the Radon Transform satisfies the Projection Slice Theorem [19], which relates the Fourier Transform of a projection with a slice of the two-dimensional Fourier Transform of the input function $g(x, y)$.

$$\mathcal{F}_{2(x,y)}\{g(x, y)\} = \mathcal{F}_{1(\tau)}\{\check{g}(p, \tau)\} \tag{3.11}$$

where $\mathcal{F}_{n(x)}$ represents the $n-th$ dimensional Fourier Transform in the x domain. This property will be used for the synthesis of the excitations in pulsed arrays.

3.2.4 Transient waveform representation

The Singularity Expansion Method [32] uses a superposition of damped oscillating functions to describe the late transient of a time-domain function $y(t)$

and an entire function accounting for its early transient.

$$y(t) \approx R_\infty \delta(t) + \sum_{i=1}^{M} R_i e^{s_i t} \tag{3.12}$$

where the Dirac-pulse and the corresponding real-valued R_∞ coefficient describe the instantaneous effect of the source (the wavefront contribution). The complex poles and residues $\{s_i, R_i\}$ take into account the oscillating contributions due to the complex natural resonances of the source and multiple diffractions by the system.

The values of the poles and residues for a good representation of the transient signal can be retrieved by means of the Prony Method [30] or of the Matrix Pencil Method, that is computationally more efficient and more robust to noise. The latter has been proposed by Sarkar ([31], [71]) and is shortly described in this section.

If the entire function is neglected, the function $y(t)$ can be expressed as a sum of complex exponentials

$$y(t_k) = \sum_{i=1}^{M} R_i e^{s_i k \Delta t} \tag{3.13}$$

where s_i and R_i are respectively the poles and the residues of the representation of order M, $k \in (0, K)$, Δt is the sampling interval and K is the number of sampled data.

Eq. (3.13) can be expressed as

$$y(t_k) = \sum_{i=1}^{M} R_i z_i \tag{3.14}$$

and the K elements of the discrete version of y can be displaced in the data matrix $[Y]$ as

$$[Y] = \begin{bmatrix} y(0) & y(1) & \dots & y(L) \\ y(1) & y(2) & \dots & y(L+1) \\ \vdots & \vdots & \vdots & \vdots \\ y(L) & y(L+1) & \dots & y(2L) \end{bmatrix}_{(L+1)X(L+1)}$$

with $L = K/2$.

The singular value decomposition of the matrix $[Y]$ is

$$[Y] = [U][\Sigma][V] \tag{3.15}$$

The parameter M is chosen such that the singular values in Σ beyond M are small and can be neglected. The choice of M can be performed using the ratio between the maximum singular value and the other singular values:

$$\frac{\sigma_M}{\sigma_{max}} = 10^{-p} \tag{3.16}$$

where p is the number of significant decimal digits in the data. A reduced matrix $[V']$ is hence constructed by using only the rows correnspondig to the M dominant singular values

$$[V'] = \begin{bmatrix} v_1 \\ v_2 \\ \vdots \\ v_M \end{bmatrix}$$

discarding the vectors that correspond to small singular values. Submatrices $[V_1]$ and $[V_2]$ are defined from $[V]$ by deleting the last and first column of $[V']$, respectively. The problem is now the solution of the eigen-value problem

$$v[V_2] = zv[V_1] \tag{3.17}$$

where the eigenvalues z correspond to the poles of the system. The residues R_i are then found as the least square solution to

$$\begin{bmatrix} y(0) \\ y(1) \\ \vdots \\ y(K-1) \end{bmatrix} = \begin{bmatrix} 1 & 1 & \dots & 1 \\ z_1 & z_2 & \dots & z_M \\ \vdots & \vdots & \vdots & \vdots \\ z_1^{K-1} & z_2^{K-1} & \dots & z_M^{K-1} \end{bmatrix} \cdot \begin{bmatrix} R_1 \\ R_2 \\ \vdots \\ R_M \end{bmatrix}$$

If $y(t)$ is the response of an electromagnetic system to a time-limited excitation, the representation of Eq.3.13 performs well in the late transient but it does not in the early transient. In the present work the singularity expansion method has been extensively used, either including the entire function or neglecting it.

3.2.5 Convolution and Deconvolution

In the time-domain approach, a UWB passive, linear, causal and time-invariant network can be characterized as a linear time-invariant (LTI) system with impulse response $h(t)$ (the antenna effective height). In particular, the output $y(t)$ of such a system to any arbitrary input $x(t)$ could be uniquely determined

by the convolution integral

$$y(t) = h(t) \star x(t) = \int_{-\infty}^{+\infty} h(u)x(t-u)du \tag{3.18}$$

where $x(t)$ is the input signal, $h(t)$ is the impulse response of the network and $y(t)$ is the corresponding output waveform. The inverse operation is defined deconvolution and indicated by $\otimes$

$$h(t) = x(t) \otimes y(t) \tag{3.19}$$

In the characterization of a UWB system, the deconvolution operation is extremely important for the retrieval of the impulse response of the system. In fact, electromagnetic simulators typically enable excitation signals of finite temporal duration, thus not allowing the direct computation of the impulse response. Various methods have been proposed in literature to perform efficient deconvolution, based for example on Moment Expansion [20] or on Matrix Pencil Technique [21].

Chapter 4

Pulsed arrays

4.1 The principle of pattern convolution

Given a linear array of N identical elements sourced by a set of currents $\{i_n(\tau)\}_{n=1..N}$, the TD radiated far field can be expressed as [23]

$$\boldsymbol{E}^A(\boldsymbol{r},t) = -\frac{\eta_0}{4\pi rc}[\boldsymbol{h}^T(\hat{\boldsymbol{r}},\cdot) * \mathcal{F}_{\mathcal{A}}(\hat{\boldsymbol{r}},\cdot)](t-\frac{r}{c}) \tag{4.1}$$

where $\hat{\boldsymbol{r}}$ is the observation point unitary vector referred to the geometrical center of the array, c is the velocity of the electromagnetic wave, $\boldsymbol{h}^T(\hat{\boldsymbol{r}},\tau)$ is the *transmitting effective height* of the common isolated radiating element and $\mathcal{F}_{\mathcal{A}}(\hat{\boldsymbol{r}},\tau)$ is the active array factor expressed in the time domain, dependent on the spatial distributions and temporal excitations of the radiating elements, which also takes into account the mutual couplings among radiating elements. The previous equation corresponds to the principle of pattern multiplication in the frequency domain formulation, which can be thus reformulated in the time-domain as a principle of pattern convolution:

total field = (element effective height) $*$ (active array factor)

If the mutual couplings among radiating elements are neglected, the array factor $\mathcal{F}(\hat{\boldsymbol{r}},t)$ (without the pedix A which relates to the active formulation) can be expressed as

$$\mathcal{F}(\hat{\boldsymbol{r}},\tau) = \sum_{n=1}^{N} i_n^+(\tau + t_n(\hat{\boldsymbol{r}})) \tag{4.2}$$

where "+" denotes the inward component of the input currents, the time delays $t_n(\hat{\boldsymbol{r}}) = \frac{\boldsymbol{r}_n \cdot \hat{\boldsymbol{r}}}{c} + t_n$ include the delayed contributions to radiation due either to physical displacement of sources ($\frac{\boldsymbol{r}_n \cdot \hat{\boldsymbol{r}}}{c}$) or to the desired scanning angle (t_n) and $\boldsymbol{r}_n$ tags the n-th antenna position. In the time domain the

array factor of a pulsed array is the field radiated by an array of isotropic elements with impulsive effective height in transmission $\boldsymbol{h}^T(\hat{\boldsymbol{r}}, \tau) = \delta(\tau)$. It is known (from [37] and from the following chapter of this thesis) that radiating elements with such an effective height can not exist, since the transmission implies at least a derivative effect, independently from the adopted antenna element. In fact, any impulse radiating antenna has to be considered as an angular-temporal filter, in the sense that it not only distributes the power along the observation angles, but it also introduces a signal distortion on the input pulse depending on the antenna shape and on the observation angle. The characterization of the transient behavior of the radiating elements is hence important in the design of pulsed arrays, since it strongly affects the shape of the radiated pulse. This is not true for monochromatic arrays, since derivative effects of radiation and of the radiating elements don't affect the shape of the radiated waveform. The array factor, in this case, is effectively the field radiated by an array of isotropic elements. The distorting effects of radiating elements on pulse radiation will be addressed deeply through the next chapters; in the next section the behavior of the array factor of pulsed arrays is presented.

4.2 Pulsed vs. Monochromatic Arrays

In conventional narrowband applications, the excitation of the array is considered quasi-monochromatic and the analysis and synthesis are performed in the frequency domain, using the well-known expression of the FD array factor

$$\mathcal{F}(\hat{\boldsymbol{r}}, \omega) = \sum_{n=1}^{N} A_n(\omega) e^{(j\omega \frac{\boldsymbol{r}_n \cdot \hat{\boldsymbol{r}}}{c})} \tag{4.3}$$

where A_n are the excitation coefficients of the array elements, typically indipendent from frequency.

The typical lobed structure of the array factor derives from the combination of the complex contributions $A_n exp(j\omega \frac{\boldsymbol{r}_n \cdot \hat{\boldsymbol{r}}}{c})$ of the radiating elements, as shown in the insets in Fig.4.1, for $N = 4$ elements equispaced at $\lambda/2$ and excited uniformly with a phase shift to steer the main beam at 22.5 degrees.

The four phasors contribute in phase for $\theta = 22.5°$, which consequently is the direction of the main lobe. The interference is totally destructive for $\theta = -7°$, the direction of the first null. For $\theta = -20.5°$ the four elements contribution reaches a local maximum, which corresponds to a side lobe of the radiation pattern. If the array factor of the same array is expressed in the time domain, using Eq.4.2 with $\{i_n^+(\tau) = sin(\omega\tau)\}_{n=1...N}$, the interference phenomenon is evident directly from the transient behavior of the waveforms, as shown graphically in Fig.4.2.

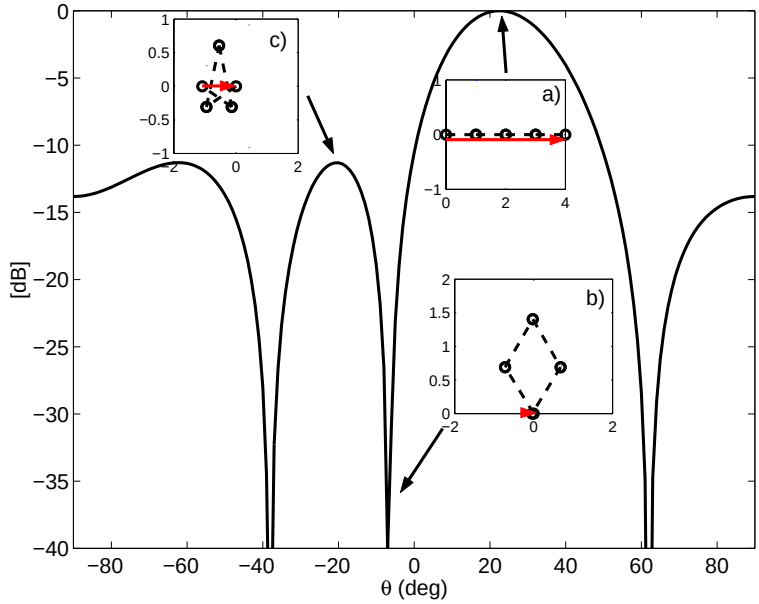

FIGURE 4.1. Array factor of four elements spaced by $\lambda/2$. The insets show the phasor contributions on a complex plane of each element at $-20.5°, -7° and 22.5°$

Fig.4.2 obviously shows the same interference phenomenon of Fig.4.1: monochromatic input waveforms, once radiated by the array elements, keep their transient behavior and sum up, creating a direction of maximum radiation and a series of local maxima and minima. This representation is useful for the analysis of pulsed arrays, namely when the excitation signals have extremely short durations and when the major interest is in the transient radiated field rather than in the steady-state pattern at one frequency. If the array elements are fed by four gaussian pulses (Eq.3.3 with $T = 0.12ns$ e $\tau = 1ns$) delayed by $63.8ps$ to maximize radiated energy at $\theta = 22.5°$, the computation of Eq.4.2 permits to obtain Fig.4.3 to 4.4. In the computation, ideal isotropic radiating elements with $\boldsymbol{h}^T(\hat{\boldsymbol{r}}, \tau) = \delta'(\tau)$ have been considered, as is evident from the derivative relationship among excitations and radiated field in Fig.4.3.

The extremely short duration of the input pulses avoids the strong interference phenomena present in the far field of monochromatic arrays. This implies the absence of grating lobes, since there are no directions, beyond that of maximum radiation, where the signals arrive exactly at the same time. In monochromatic arrays this is instead possible due to the periodicity and long duration of the input waveforms, which, under particular coupling conditions, cause also the phenomenon of blind spots. As it will be shown in Chapter 6, the coupling among antennas in pulsed arrays have reduced impact on radiation,

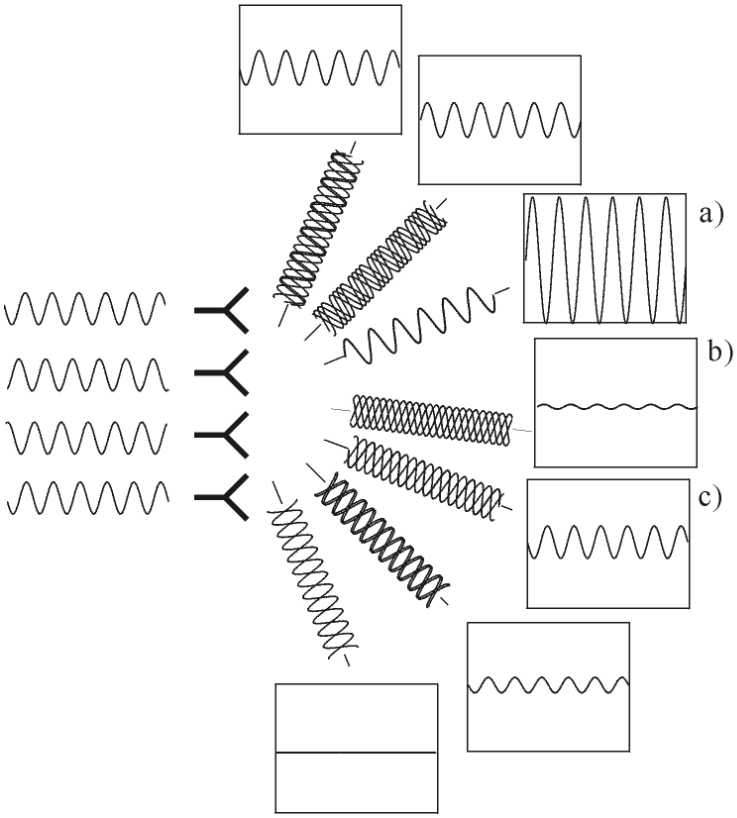

FIGURE 4.2. Array of four isotropic antennas equispaced by $\lambda/2$: excitation, elements contributions and transient radiated field

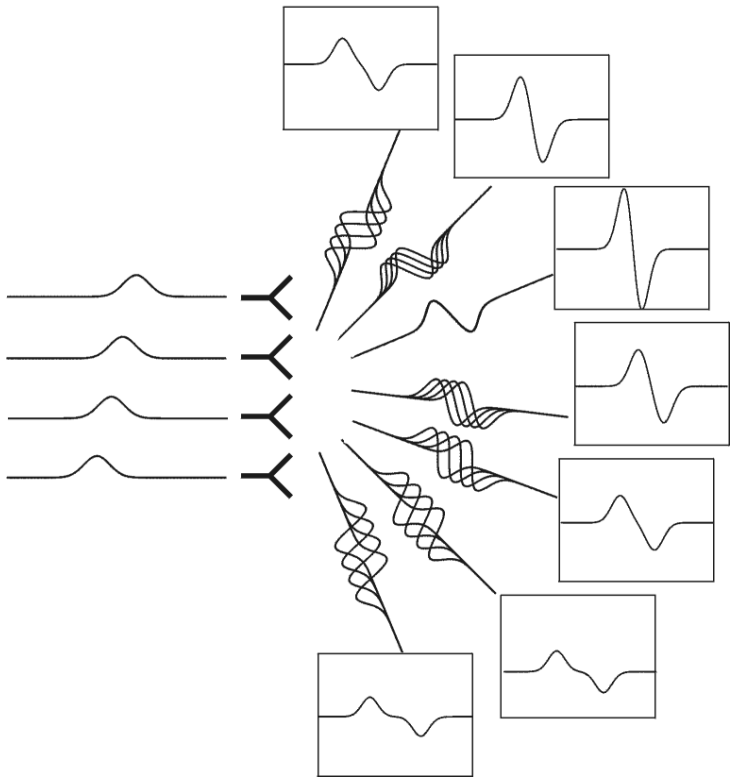

FIGURE 4.3. Array of four antennas equispaced by $\lambda/2$: excitation, elements contributions and transient radiated field

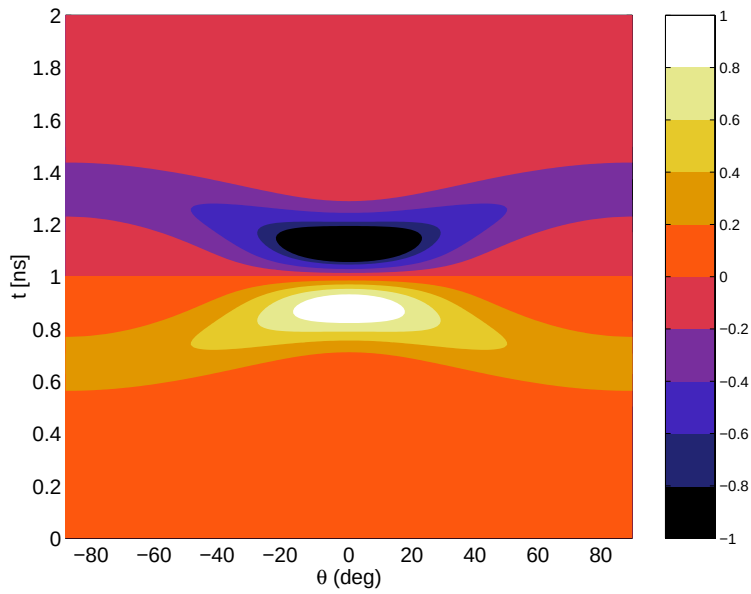

FIGURE 4.4. Transient array factor of the array of four elements

and the blind spot effect is luckily lost. Fig.4.4 shows the array factor behavior as a function of the temporal and angular domains. It is evident the absence of the lobed structure of the patterns of monochromatic arrays. However lobes do not completely disappear, since smoothed phenomena of interference can happen: in particular, the radiation of trains of input pulses can imply the appearence of spurious lobes (cross-pulse lobes) caused by "pulse interference" (in contrast with canonical sidelobes caused by "phase interference")

Fig.4.4 and Fig.4.5 are typical examples of the graphical representation of the transient far field that will be used throughout the thesis.

Fig.4.5 uses a polar system of coordinates where the radial coordinate is τ and the angular one is θ. It is useful for the representation of the effective height of radiating elements, since it contains the whole radiation information along a plane for one polarization.

4.3 Requirements for the characterization of pulsed arrays

From the short introduction presented in this chapter, it can be derived that the characterization of a pulsed array requires:

1. the efficient transient characterization of the isolated radiating element that constitutes the array (its effective height $\boldsymbol{h}^T(\hat{\boldsymbol{r}}, \tau)$);

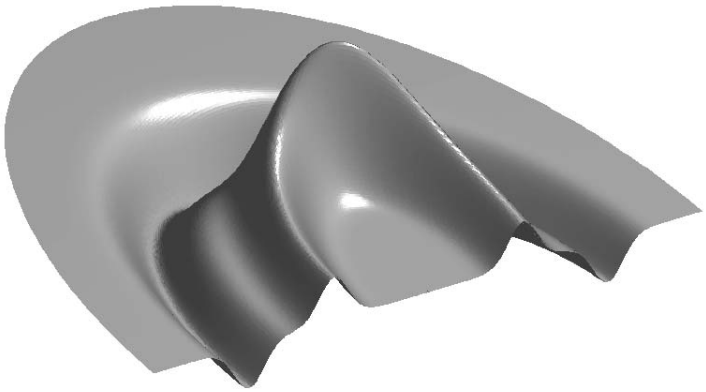

FIGURE 4.5. Transient array factor of the array of four elements: surface plot

2. the analysis of the effects of their spatial displacement and transient excitations (mutual coupling behavior);

3. the design of their spatial displacement and transient excitations in order to radiate a desired far field (a synthesis technique).

Each of these subjects has been developed during the previous three years and reported in the following chapters of this thesis.

Chapter 5

Efficient Characterization of Radiating Elements

5.1 Introduction

The time-domain effective height $\boldsymbol{h}^T(\hat{\boldsymbol{r}}, \tau)$ [64] - [67] plays the role of impulse response operator linking the transient radiated field to the real antenna input waveform by a convolution integral. According to the theory in [37], TD effective height is defined in terms of the Radon transform of the (electric or magnetic) antenna current impulse response (corresponding to a feeding Dirac voltage pulse). In the frequency domain the transfer function $\boldsymbol{\mathcal{H}}(\hat{\boldsymbol{r}}, \omega)$, which is directly related to the realized gain (and hence includes the antenna-source mismatch) is the Fourier transform of the effective height. Except for a few cases, mainly concerning large antennas, [68], [69], analytical modelling of the time-domain effective height is not easily achievable due to the antenna geometrical and electrical complexity.

Therefore local numerical tools, and first of all the Finite-Difference Time-Domain (FDTD) method [39], are commonly used to calculate and store the TD surface current and finally, the Radon transform is evaluated numerically, including a near to far field (N2F) transformation and a deconvolution operation. The application of these methods undergoes some critical aspects. Interpolations over spatial and temporal variables and time buffers are required, during FDTD calculation, to comply with the field staggering within the elementary cell and with the delay time from each surface point source to the observation points. "*Off-line*" processing, e.g. the N2F transformation after the FDTD run has finished, is generally forbidden due to the not manageable amount of data produced by the transient near field storage. Moreover, spatial and temporal variables are strongly coupled by radiation integrals and a new numerical evaluation is required for each observation time and observation point. Calculation and application of TD effective height is therefore

a tedious and time-consuming process that produces a large four-dimensional data set. This fully numeric representation is not very suitable to be used for the evaluation of pulsed array performances. In recent papers, new approaches have been presented to overcome some of the above method drawbacks. In [41] the multipole expansion is proposed where the weighting coefficients are computed in the time domain by the enforcement of boundary conditions. A rather different algorithm has been presented in [42] which employes a system identification method to extrapolate transient far field at each observation point. The simplification of the N2F transformation in the case of radiation from apertures on an infinite screen is described in [43] involving the only electric field processing. In the same paper, wavelet analysis has been used to compress time domain data at each aperture point. Finally, in [44] the frequency and transient behavior of an antenna is described by a small set of parameters using the singularity expansion method applied to measurements. Some of these works have been presented during the period in which this thesis was developed, showing the interest in the field and also the diversity of approaches which can be used. It is straightforward that a TD analytical or semi-analytical model would simplify the antenna and array characterization over a wide band.

The chapter presents two approaches that permit semi-analytical representations of the effective height.

One method addresses aperture antennas and employes a data fitting strategy where the aperture field distribution is represented by means of summation over suitable space- and time-variant basis functions. The waveguide eigenvectors are used for the spatial dependence, while the time dependence is interpolated over a set of complex exponentials. The expansion coefficients are computed in the time domain, during the FDTD run. The method is based on previous papers [45], [46] concerning the broadband radiation from cavity backed aperture antennas by the *Modal* near to far field transformation in the frequency and in the time domain.

The second method that is presented in this chapter addresses antennas of more general shapes, such as UWB dipoles, TEM horn and non canonical-aperture horns. This technique uses a compact UWB field representation employing the two-dimensional Associate Hermite Functions (AHF2). This base has been already introduced many years ago for the modeling of optical resonators and beam-waveguides [74], [75] and then applied in the microwave region [15] for the frequency-domain modeling of large apertures exploiting the possibility to approximately calculate the Fresnel and Fraunhofer radiation by simple formulas. Further interesting multiscale applications can be found in [12] where the Hermite formalism was adopted for image coding and computer visual systems. Such a base is here applied to time-varying electromagnetic images, by means of an automatic a-priori choice of the most critical parame-

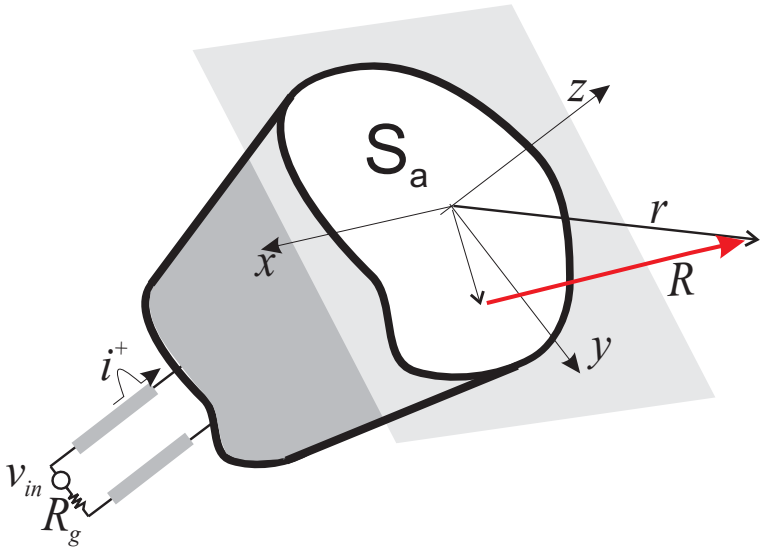

FIGURE 5.1. Coordinate system for aperture antenna problems. A real voltage source exciting the input signal is connected to the aperture antenna (slot, open waveguide or horn) by means of a transmission line. To simplify the model, the aperture is supposed to radiate from an infinite screen.

ters such as the scaling factors. The model is useful for directive antennas, but it is much more general than the model involving an aperture on an infinite screen.

5.2 Aperture Antennas

5.2.1 TD aperture effective height

An antenna with a radiating aperture S_a laying on the plane $z = 0$ ($\hat{\boldsymbol{z}}$ is the normal unitary vector on S_a) is driven through a transmission line (Fig.5.1) by a real voltage generator of internal resistance R_g, which excites the input waveform $v_{in}(t)$. According to the formulation in [37], a linear-system-type representation of any antenna time-dependent far field is:

$$\boldsymbol{E}(\boldsymbol{r}, t) = -\frac{1}{8\pi rc}\frac{\eta_0}{R_g}[v_{in}(\cdot) * \boldsymbol{h}^T(\hat{\boldsymbol{r}}, \cdot)](t - \frac{r}{c} - t_g) \tag{5.1}$$

where c is the speed of light, η_0 is the free-space impedance, t_g is the time delay along the line, "$*$" denotes convolution, and $\boldsymbol{h}^T(\hat{\boldsymbol{r}}, \tau)$ is the time-domain antenna effective height in transmitting mode.

Denoting with $\boldsymbol{E}_a^\delta(\boldsymbol{\rho},\tau)$ (units in $[\Omega m^{-1}s^{-1}]$) the tangential component of aperture field corresponding to a Dirac-pulse input current, the TD effective height of the aperture (see Appendix for details), supposed to radiate from an infinite screen, is:

$$\boldsymbol{h}^T(\hat{\boldsymbol{r}},\tau) = 2\left[-\frac{1}{\eta_0}\hat{\boldsymbol{r}} \times \iint_{S_a} \boldsymbol{E}_a^\delta(\boldsymbol{\rho},\tau+\frac{\hat{\boldsymbol{r}}\cdot\boldsymbol{\rho}}{c})ds \times \hat{\boldsymbol{z}}\right] * \delta^{(1)}(\tau) \tag{5.2}$$

where, for simplicity, it has been supposed $t_g = 0$. The function $\delta^{(1)}(\tau) = \frac{\partial}{\partial\tau}\delta(\tau)$ accounts for the derivative effect on the input signal. The Radon transform within square brackets (units in m/s) is the effective height in the receiving mode, $\boldsymbol{h}^R(\hat{\boldsymbol{r}},\tau)$.

The knowledge of TD effective height requires the application of a local method, such as FDTD, to calculate the aperture field when the antenna is sourced by a broadband test signal $v_0(t)$, typically a gaussian pulse, since the Dirac pulse is not suitable as input signal for numerical codes. The corresponding aperture field $\boldsymbol{E}_a(\boldsymbol{\rho},t)$ has to be stored within the whole transient and numerical deconvolution is then applied to each aperture radiating pixel to calculate the impulse response $\boldsymbol{E}_a^\delta(\boldsymbol{\rho},\tau)$. Finally, the effective height is obtained by numerical evaluation of surface integral in (5.20) which has to be repeated at any required time and observation direction because of the coupling between angular and spatial variables. The numerical effective height will be a baseband approximation, within the band of $v_0(t)$, of the true effective height.

5.2.2 Numerical representations of the aperture impulse response

A great simplification in the above numerical procedure is achieved in this work by introducing an approximated space-time uncoupling model of the impulsive aperture field $\boldsymbol{E}_a^\delta(\boldsymbol{\rho},\tau)$:

$$\boldsymbol{E}_a^\delta(\boldsymbol{\rho},\tau) \approx \sum_{p=1}^{N} g_p(\tau)\boldsymbol{e}_p(\boldsymbol{\rho}) \tag{5.3}$$

$\{\boldsymbol{e}_p(\boldsymbol{\rho})\}$ are time-independent aperture basis functions, here the transverse eigenvectors (modes) of the waveguide having S_a cross-section. $\{g_p(\tau)\}$ (units in $[\Omega/s]$) are unknown time-variant coefficients, hereafter denoted as *scalar impulse responses,* which have to be computed numerically from the aperture field $\boldsymbol{E}_a$ excited by v_0. At this purpose, the computed $\boldsymbol{E}_a$ is fitted, at runtime, onto the same basis by coefficients $\frac{\gamma_p(t)}{2R_g} = \iint_{S_a} \boldsymbol{E}_a(\boldsymbol{\rho},t)\cdot\boldsymbol{e}_p(\boldsymbol{\rho})ds$. The

unknown scalar impulse responses are finally obtained by deconvolution of scalar functions instead of surface vector functions:

$$\gamma_p(t) = \int_0^t g_p(t-\tau)\, v_0(\tau)\, d\tau \tag{5.4}$$

The solution of above integral equation in a form suitable for the calculation of the effective height in (5.20) is achieved by introducing two different models of scalar impulse response $g_p(\tau)$ within the hypothesis that the test signal $v_0(t)$ is a practically time-limited excitation signal in $[0, T_0]$. The first model, denoted as Complete fitting (CF) model gives a more efficient representation of the early transient, while the second one, referred to as Incomplete fitting (IF) model, is less accurate in the early transient but permits to derive simple semi-analytical expressions for the TD effective height.

Complete Fitting (CF) model

According to the Singularity Expansion Method [32], the response of an electromagnetic system to a time-limited excitation can be represented by a superposition of damped oscillating functions, which describe the late transient, and an entire function accounting for the early transient. Therefore the following model for the scalar impulse responses $g_p(\tau)$ is introduced:

$$g_p^{CF}(\tau) \approx g_{p,\infty}\delta(\tau - t_p) + \sum_{k=-K_p}^{K_p} g_{pk} e^{s_{pk}\tau} U(\tau - t_p) \tag{5.5}$$

where the shifted Dirac-pulse and the corresponding real-valued $g_{p,\infty}$ coefficient describe the instantaneous effect of the driving voltage source on the aperture modes. The complex poles and residues $\{s_{pk}, g_{pk}\}$ take into account the oscillating contributes due to the complex natural resonances of the source, and multiple diffractions by the guiding section (or cavity) and by the aperture.

Introducing (5.5) in (5.4):

$$\gamma_p(t) = g_{p,\infty} v_0(t - t_p) + \sum_k g_{pk} e^{s_k t} \int_0^{T_0} e^{-s_{pk}\tau} v_0(\tau)\, U(t - \tau - t_p)\, d\tau \tag{5.6}$$

Although the averaged delay time t_p is estimated numerically as shown later on, it is first assumed that $t_p \approx z_A/c$ where z_A is the distance of the source point from the aperture centre.

The impulse response parameters are calculated by a two-steps procedure. First, poles and residues $\{g_{pk},\ s_{pk}\}$ are computed from the late transient of shifted signal $\gamma_p(t - \frac{z_A}{c} - T_0)$ by the method in [57]. Then the coefficients

of the Dirac functions are estimated by processing of γ_p within the early time interval $\frac{z_A}{c} < t' < \frac{z_A}{c} + T_0$. Denoting with $\gamma_p^{(p)}(t')$ the poles's contribute to γ_p:

$$\gamma_p^{(p)}(t') = \sum_k g_{pk} e^{s_{pk} t'} \int_0^{t' - \frac{z_A}{c}} e^{-s_{pk}\tau} v_0(\tau)\, d\tau \tag{5.7}$$

the *non-pole* contribute is calculated as $\gamma_p^{(np)}(t') = \gamma_p(t') - \gamma_p^{(p)}(t')$. Parameters $\{t_p,\ g_{p,\infty}\}$ are hence evaluated by best fitting of $\gamma_p^{(np)}(t')$ to $g_{p,\infty} v_0(t' - t_p)$. In particular, a refinement of t_p is such to maximize the correlation $\int_p \gamma^{(np)}(t')\, v_0(t' + t_p)\, dt'$ and parameter $g_{p,\infty}$ is then calculated by least square method. However, numerical simulations have shown that the estimated delay t_p is nearly coincident with z_A/c.

Incomplete Fitting (IF) model

A simplified representation of the scalar impulse response, $g_p^{IF}(\tau)$, can be obtained by using only the complex exponentials set. However poles and residues are now expected to be different than the corresponding parameters of the CF-model. The IF expansion is extremely fast convergent in the late transient, while a larger number of exponentials are required to fit the very early transient.

The fitting parameters are computed by a different procedure. The scalar impulse response $g_p(\tau)$ is numerically deconvolved from (5.4) by the fourth-order Moment Expansion (ME) deconvolution [70] and then $g_p(\tau)$ is fitted on $g_p^{IF}(\tau)$ for $\tau > t_p$ by means of the Matrix Pencil method [71].

In both the deconvolution schemes, the set of poles and residues to be really retained and stored for the calculation of the radiated field can be thinned according to the strength of the *energy* indicator ξ_{pk} associated to each $pk-$th pole.

$$\xi_{pk} = \int_0^\infty |g_{pk} e^{s_{pk} t}|^2 dt \tag{5.8}$$

In particular, only poles with energy higher than one per thousand of the maximum energy will be retained for the effective height computation. The choice of the threshold follows the guidelines discussed in [46].

5.2.3 Approximate calculation of time domain effective height

Consider first the CF-model of the impulsive aperture field, by combining (5.5) with (5.3) and (5.20), the effective height is there written in the following approximate form:

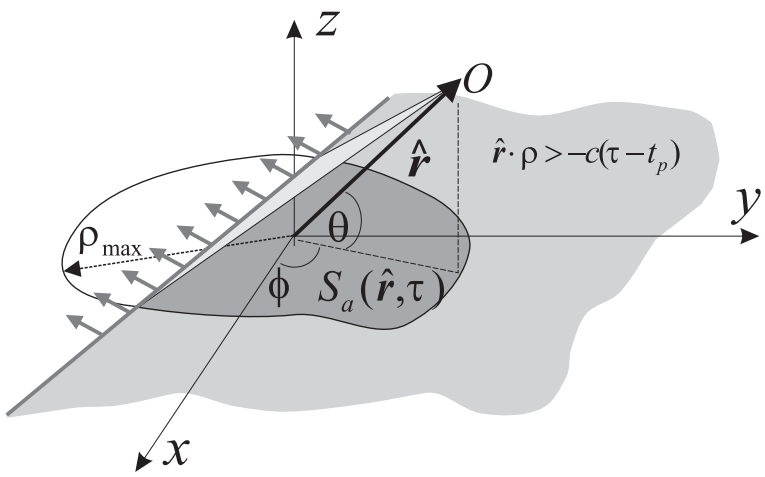

FIGURE 5.2. Portion $S_a(\hat{\boldsymbol{r}},\tau)$ of the aperture whose radiation contributes at times $\tau < t_p + \frac{\rho_{\max}}{c}$ to the effective height at observation direction $\hat{\boldsymbol{r}}$.

$$\boldsymbol{h}^T(\hat{\boldsymbol{r}},\tau) = 2\sum_{p=1}^{N}\left\{\ g_{p,\infty}\boldsymbol{h}^R_{p,\infty}(\hat{\boldsymbol{r}},\tau) + \textstyle\sum_{k=-K_p}^{K_p} g_{pk}\boldsymbol{h}^R_{pk}(\hat{\boldsymbol{r}},\tau)\ \right\} * \delta^{(1)}(\tau) \tag{5.9}$$

where the following integrals need to be solved:

$$\begin{bmatrix}\boldsymbol{h}^R_{p,\infty}(\hat{\boldsymbol{r}},\tau)\\ \boldsymbol{h}^R_{pk}(\hat{\boldsymbol{r}},\tau)\end{bmatrix} = -\frac{1}{\eta_0}\hat{\boldsymbol{r}}\times \iint_{S_a}\begin{bmatrix}\delta(\tau - t_p + \frac{\hat{\boldsymbol{r}}\cdot\boldsymbol{\rho}}{c})\\ U(\tau - t_p + \frac{\hat{\boldsymbol{r}}\cdot\boldsymbol{\rho}}{c})e^{s_{pk}(\tau+\frac{\hat{\boldsymbol{r}}\cdot\boldsymbol{\rho}}{c})}\end{bmatrix}\boldsymbol{e}_p(\boldsymbol{\rho})ds\times\hat{\boldsymbol{z}} \tag{5.10}$$

A trivial solution can be obtained at boresight radiation (e.g. $\theta = 0$, and $\hat{\boldsymbol{r}}\cdot\boldsymbol{\rho} = 0$) where the angular and temporal variables are fully decoupled. In this case it is easy to prove that the effective height can be expressed, for both CF- and IF-model, as:

$$\boldsymbol{h}^T(\tau) = 2\sum_{p=1}^{N}\boldsymbol{e}_p^{(0)}g_p(\tau) * \delta^{(1)}(\tau) \tag{5.11}$$

The constant vector $\boldsymbol{e}_p^{(0)} = -\frac{1}{\eta_0}\hat{\boldsymbol{r}}\times\iint_{S_a}\boldsymbol{e}_p(\boldsymbol{\rho})ds\times\hat{\boldsymbol{z}}$ is calculated exactly for canonical apertures such as rectangular and circular and vanishes for odd aperture patterns.

In the more general case of off-boresight observation, $\boldsymbol{h}^R_{p,\infty}$ is transformed into a line integral applied to the basis function $\boldsymbol{e}_p(\boldsymbol{\rho})$ along a time varying boundary by the properties of Dirac functions, as discussed in Appendix, for the particular case of rectangular apertures. Concerning the integral $\boldsymbol{h}^R_{pk}$, it can be observed that the presence of Heaviside function $U(\tau - t_p + \frac{\hat{\boldsymbol{r}}\cdot\boldsymbol{\rho}}{c})$ accounts for the very early transient when only the portion $S_a(\hat{\boldsymbol{r}},\tau)$ of the aperture, intercepted by the half-plane $\tau - t_p + \frac{\hat{\boldsymbol{r}}\cdot\boldsymbol{\rho}}{c} > 0$, gives contribution to the observation point (see Fig.5.2). After a time $\tau > t_p + \frac{\rho_{\max}}{c}$, $\rho_{\max}$ being the maximum distance between aperture rim and its centre, the observation point starts to collect radiation from the whole aperture and the Heaviside function approach to unity. Integral $\boldsymbol{h}^R_{pk}$ can be therefore decomposed as:

$$\boldsymbol{h}^R_{pk}(\hat{\boldsymbol{r}},\tau) = -\frac{1}{\eta_0}\begin{cases} \hat{\boldsymbol{r}} \times e^{s_{pk}\tau} \displaystyle\iint_{S_a(\hat{\boldsymbol{r}},\tau)} e^{s_{pk}(\frac{\hat{\boldsymbol{r}}\cdot\boldsymbol{\rho}}{c})}\boldsymbol{e}_p(\boldsymbol{\rho})ds \times \hat{\boldsymbol{z}} & \\ & \text{if} \quad |\tau - t_p| \leq \frac{\rho_{\max}}{c} \\ \cos\theta \boldsymbol{F}_{pk}(\hat{\boldsymbol{r}})e^{s_{pk}\tau} & \\ & \text{if} \quad \tau > t_p + \frac{\rho_{\max}}{c} \end{cases} \tag{5.12}$$

where $\boldsymbol{F}_{pk}(\hat{\boldsymbol{r}})$ is the $p-$th modal space factor

$$\boldsymbol{F}_{pk}(\theta,\phi) = \iint_{S_a} \boldsymbol{e}_p(\boldsymbol{\rho})e^{\frac{s_{pk}}{c}\hat{\boldsymbol{r}}\cdot\boldsymbol{\rho}}\boldsymbol{d\rho} \tag{5.13}$$

which is the spectral Fourier transform of the $p-$th aperture field pattern evaluated at singular frequency $\omega = -js_{pk}$ and it is known in closed form for both rectangular and circular apertures (see [46] and Appendix).

The numerical integration of $\boldsymbol{h}^R_{pk}$ is therefore only required within the very short time interval $\frac{\rho_{\max}}{c}$ which leads to a modest increase in the computational effort compared with a true closed form. However, exact integrals, just like $\boldsymbol{F}_{pk}$, can be derived even in the very early transient for the principal cuts $\phi = \{0, \frac{\pi}{2}\}$, at least for rectangular apertures.

For the case of IF-model of the aperture field only integrals $\boldsymbol{h}^R_{pk}(\hat{\boldsymbol{r}},\tau)$ need to be solved for off-boresight radiation. However, it is interesting to discuss within which condition the closed form expression, appearing in the lower branch of (5.12), may be used as *early-time extrapolator* also within the interval $|\tau - t_p| \leq \frac{\rho_{\max}}{c}$ therefore avoiding the numeric evaluation of the integral on the time-dependent surface $S_a(\hat{\boldsymbol{r}},\tau)$. In this case the effective heights can be simply calculated with full separation of time and angular variables as

$$\boldsymbol{h}^R(\hat{\boldsymbol{r}},\tau) = -\frac{1}{\eta_0}\cos\theta \sum_{p,k} g_{pk}\boldsymbol{F}_{pk}(\hat{\boldsymbol{r}})e^{s_{pk}\tau} \tag{5.14}$$

TABLE 5.1. Computational costs of main processing tasks

Task	Complexity
Deconv. of $\boldsymbol{E}_a^{\delta}(\boldsymbol{\rho},\tau)$	$2O^{DE}(N_t)N_c$
Deconvolution of $g_p(\tau)$	$O^{DE}(N_t)N$
Calculation of Radon Transform	$2N_aN_tN_c$
Modal decomposition on the aperture	$2NN_tN_c$
Parameter estimation (SVD)	$O^{SVD}(N_{t1})N$
Early-time calculation of $\boldsymbol{h}_{pk}^R$	$2NN_{t2}N_aN_c$
Early-time calculation of $\boldsymbol{h}_{p,\infty}^R$	$2N\sqrt{N_c}N_{t2}N_a$

and $\boldsymbol{h}^T(\hat{\boldsymbol{r}},\tau) = 2\boldsymbol{h}^R(\hat{\boldsymbol{r}},\tau) * \delta^{(1)}(\tau)$. Since the above approximation only interests the very early transient, it will mainly affect the high frequency content of the effective height and its accuracy is expected to depend on the aperture size $\rho_{\max}$. It is therefore reasonable that, for a given $\rho_{\max}$, the early-time extrapolation will be accurate up to a maximum frequency $f_{\max}$ and the following heuristic guideline for the extrapolation usage is assumed:

$$\rho_{\max} f_{\max} \leq Kc \tag{5.15}$$

where c is the speed of light and K a constant. This expression will be verified by numeric analysis in the next section.

5.2.4 Discussion about numerical complexity

The numerical complexity of the proposed method, compared with the standard calculation which involves the deconvolution of the aperture field and then the numerical Radon transform, is here discussed. The following notation is adopted: N_t means the number of FDTD time samples of the antenna response, N_c the number of space samples on the aperture, N_a the number of observation angles and again N the number of basis functions on the aperture. The main processing tasks that will be considered for the CF- and IF-modes evaluation are the modal decomposition, the deconvolution of scalar impulse responses, the Matrix Pencil method, which is essentially based on the SVD, and the numerical calculation of time-dependent integrals in (5.10) and (5.12) by finite summations. Relevant computational costs are listed in Tab.1.

The numerical complexity of deconvolution (having supposed to adopt fourth order Moment Expansion as in [70]) is $O^{DE}(N_t) = 4N_t$; the SVD complexity is [72] roughly $O^{SVD}(N_{t1}) = (\frac{N_{t1}}{2})^3$ where $N_{t1} = N_t/n_d$ denotes a resampled set of the FDTD oversampled data (generally $n_d = 3 \div 5$); $N_{t2} \approx \frac{2\rho_{\max}}{c} \approx \sqrt{N_c}/c$ is the number of early-time samples. By simple mathematical manipulations and some approximations, the following expressions for the complexity are obtained:

$$O^{ST} = 2N_a N_c N_t \tag{5.16}$$

$$O^{CF} = N[2N_t N_c + \frac{N_t^3}{8n_d^3} + 2N_a N_c^{3/2}/c] \tag{5.17}$$

$$O^{IF} = 2N[N_t N_c + \frac{N_t^3}{8n_d^3} + N_a N_c^{3/2}] \tag{5.18}$$

where O^{ST} is for the complexity of the standard method. The speed-up of the two proposed procedures respect to standard calculation, namely $SU^{CF} = O^{ST}/O^{CF}$ and $SU^{IF} = O^{ST}/O^{IF}$, are represented in Fig.5.3 vs. the number of time samples, for typical parameters' values. It can be observed that the benefit of the CF- and IF-models are as much relevant as the number of the required aperture basis functions is small. The CF-model appears more efficient than the IF-model, even for a same number of aperture functions, since it avoids the numerical deconvolution by Moment Expansion and permits to perform deconvolution and parameters' estimation within a same task. The speed-up gets worse, in both the models, as the number of time samples increases due to the larger computational time wasted in the aperture field expansion. However, for typical 10^3 time samples and $N = 5$, the speed-up is about 10 for both the methods. Much more relevant benefits are achieved when the effective height needs to be evaluated at a larger set of angles.

5.2.5 Numerical Analysis

Radiation from a rectangular aperture

A rectangular $a \times b$ slot on a perfect electric screen is excited by a dipole placed in front of the aperture (inset in Fig.5.4). The structure has been meshed on a uniform rectangular FDTD grid, with voxel size $\Delta = 0.5cm$, which includes the antenna and a small region in the close surrounding of the aperture. Denoting with $f^{FDTD} = c/(10\Delta) = 6GHz$ the maximum frequency permitted by a such FDTD grid, the dipole has been sourced by a test gaussian signal $v_0(t) = e^{-\frac{(t-a)^2}{2\beta^2}}$ whose parameters α, β, are adjusted so that the frequency, $f_{\max}$, where the spectrum amplitude $|V_0(f)|$, ($V_0(f)$ is the Fourier transform of $v_0(t)$), attenuates to the 10% of its maximum value (in symbols: $|V_0(f_{\max})| = \frac{1}{10}\max|V_0(f)|$) is exactly f^{FDTD}. Accordingly, the effective height computed by means of the proposed methods will permit to process only those input signals $v_{in}(t)$ whose spectrum is within $[0, f^{FDTD}]$.

To obtain $\boldsymbol{h}(\hat{\boldsymbol{r}}, \tau)$ parameters, the transient aperture field has been then processed by the proposed methods, involving both CF- and IF-models. The

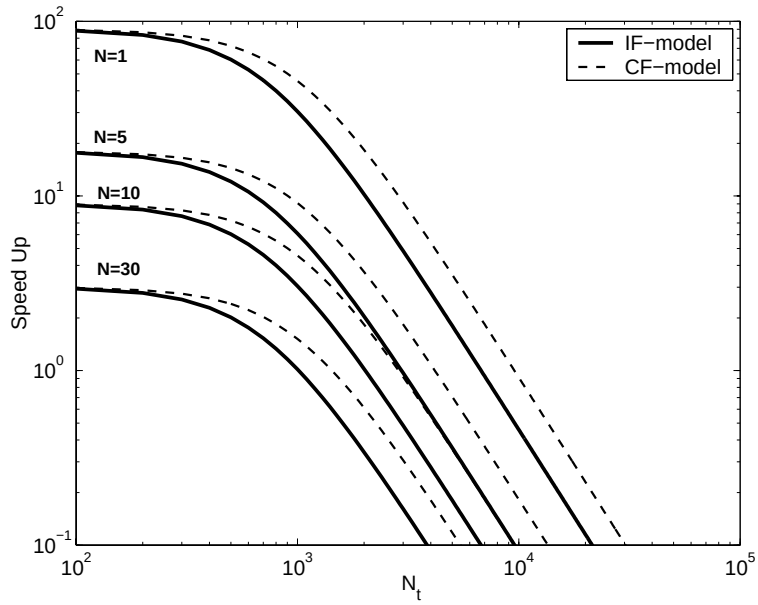

FIGURE 5.3. Speed-up of the proposed methods in the calculation of the effective height along a single angular cut with 2° increments ($N_a = 90$) and typical values $N_c = 10^3$, $n_d = 4$.

only TE_{10} mode has been considered for the effective height calculation. Results mainly differ (Fig.5.4) in the early transient where the IF-model requires a larger number of poles.

To discuss the accuracy of the effective height formulas depending on the number of poles used in the time-domain model of the impulsive aperture field, the transient electric far field, denoted with $E^{conv}(\boldsymbol{r}, t)$, has been calculated by means of the convolution in (5.1) when the input signal is a gaussian pulse with $f_{\max} = 4.5GHz$ (e.g. within the numerical effective height band). That field is compared with a reference solution, denoted with $E^{FDTD}(\boldsymbol{r}, t)$, obtained, here and in the next examples, by an independent time-consuming FDTD simulation sourced by $v_{in}(t)$ and extending within a larger domain including also the far field test points. The following instantaneous error at observation point $\boldsymbol{r}_0$ for the E_ϕ component has been further considered:

$$\delta E(\boldsymbol{r}_0, t) = \frac{|E_\phi^{FDTD}(\boldsymbol{r}_0, t) - E_\phi^{conv}(\boldsymbol{r}_0, t)|}{\left\|E_\phi^{FDTD}(\boldsymbol{r}_0, t)\right\|_\infty} \tag{5.19}$$

As expected, the error is higher in the early transient and decreases as the time goes on (Fig.5.5). Moreover, CF-model's outcomes are more accurate than those obtained with IF-model which requires a larger number of poles to guarantee the same accuracy. In particular, by using 3 and 6 poles for

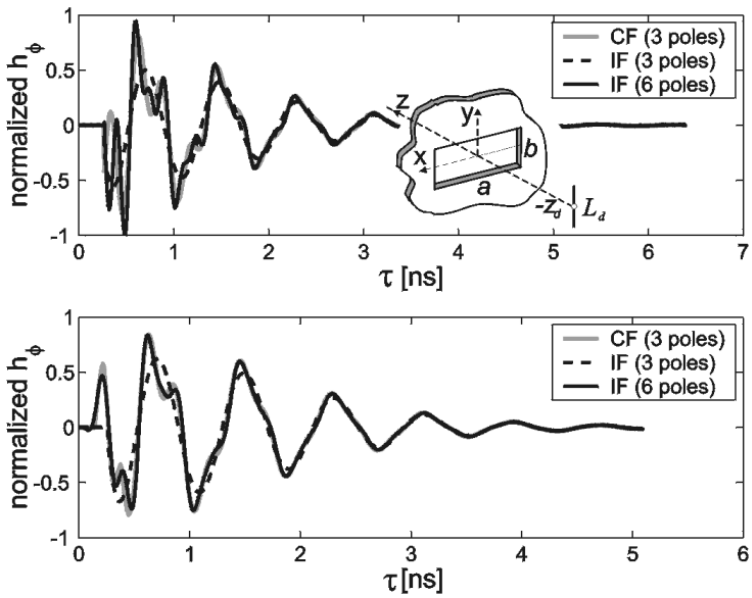

FIGURE 5.4. Characterization of a dipole-fed rectangular slot: size (in cm) $a = 10$, $b = 5$, $L_d = 11.5$, $z_d = 8$. Effective height in transmitting mode along the boresight (up) and (down) off the boresight at $\theta = 42°$, $\phi = 45°$. Dirac pulses at $\tau = t_p \approx z_A/c$ are not shown.

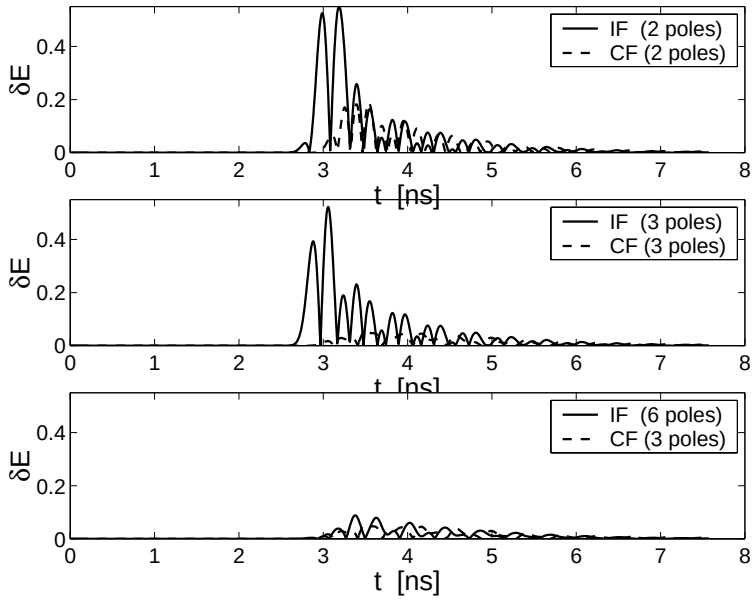

FIGURE 5.5. Radiation from the dipole-slot system: instantaneous error in the far field calculation, at point ($r = 74cm$, $\theta = 42°$, $\phi = 45°$), for an input gaussian pulse with 3dB-frequency of $4.5GHz$. The convolution equation in (5.1) has been applied for different orders of CF- and IF-models.

the CF and IF model, respectively, the estimated radiated field compares well (Fig.5.6) with the reference solution.

In a further experiment, the accuracy degradation of the simplified IF-model caused by the early-transient approximation, e.g. by the direct use of the semi-analytical formula (5.14), is investigated. To this purpose a set of input gaussian pulses with different maximum frequencies $f_{\max} = \{3GHz, 4GHz, 6GHz\}$ are convolved with the effective height computed by the different models and compared with the corresponding reference solutions. In particular, only the early transient $t < \frac{z_A+r}{c} + \frac{3\rho_{\max}}{2c}$ ($\rho_{\max} = \sqrt{a^2+b^2}/2 = 5.6cm$) is considered for an off-boresight observation point and the relative peak error $\delta\tilde{E}(\boldsymbol{r}_0) = \max_t \delta E(\boldsymbol{r}_0, t)$ is evaluated. As depicted in Fig.5.7, errors increase with the upper frequency of the input signal and the accuracy of the extrapolated IF effective height is a few points worse than the conventional complete model. The maximum frequency of the input signal up to which the further simplified effective height in (5.14) still applies with an accuracy comparable to the true IF-model, is hence chosen such that the error difference with that model exceeds 1%. The heuristic guideline in (5.15) is hence verified with $f_{\max} = 4.5GHz$, and therefore $K \simeq 0.85$. The early time extrapolation within

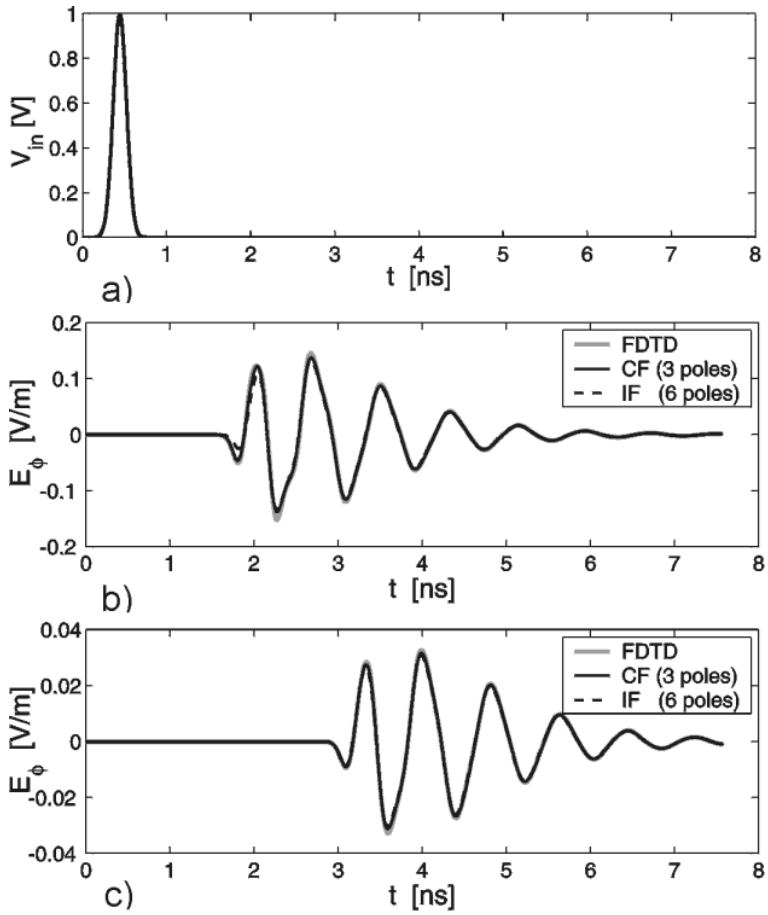

FIGURE 5.6. Radiation from a dipole-slot system: a) input gaussian pulse sourcing the dipole with highest frequency $f_{\max} = 4.5GHz$. Comparison of far field at (b) point ($r = 35cm$, $\theta = 0°$, $\phi = 0°$) and (c) point ($r = 74cm$, $\theta = 42°$, $\phi = 45°$) obtained by full FDTD analysis and convolution between v_{in} and the numerical effective height.

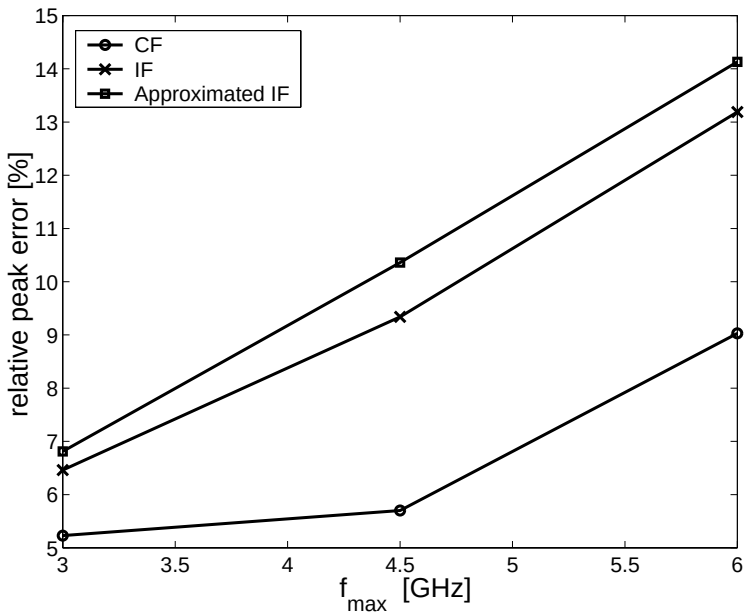

FIGURE 5.7. Radiation from a rectangular slot: relative peak error for different input gaussian signals of upper frequencies $f_{\max}$ and different models of effective height.

$|\tau - t_p| \leq \frac{\rho_{\max}}{c}$, by the simplified IF formula (5.14), can be therefore roughly applicable up to frequency $f \leq c/\rho_{\max}$.

UWB Ridged pyramidal horn

The proposed method is now applied to characterize the effective height of a wideband pyramidal ridged horn. The transmitting effective height computed in the band [0 -6.5GHz] is shown in Fig.5.8 at two different observation angles. The estimated delay time t_p is nearly identical to z_A/c ($t_p = 1.11ns$ for the TE_{10} mode and $z_A/c = 1.12ns$). Also in this case the simplified IF-model in (5.14) is still able to extrapolate the not negligible effective height oscillations in the very early time.

As an example of how the computed effective height can be useful in the evaluation of real transmitted signal distortion, the following excitation signal for the horn antenna is considered: $v_{in}(t) = x_{DG}(t) - \frac{1}{2}x_{DG}(t - 1.6ns)$, where x_{DG} is a derivated gaussian pulse, $x_{DG}(t) = \frac{t-\alpha}{\beta}\exp(-(t-\alpha)^2/(2\beta^2))$, with maximum frequency (defined as in the previous example) $f_{\max}$ =3.5 GHz (Fig.5.9). The corresponding radiated field has been computed via the convolution in (5.1) with the effective height. Comparisons in Fig.5.9 show a good agreement between reference solution and the data computed by the new

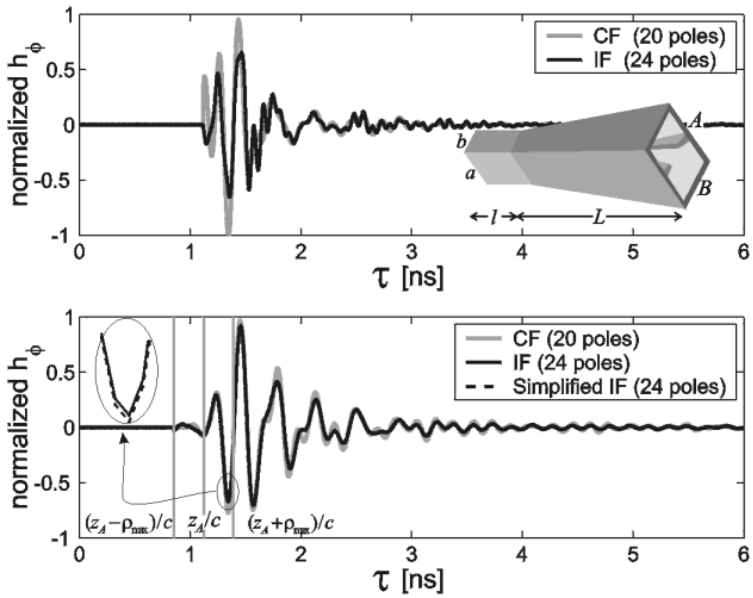

FIGURE 5.8. Pyramidal ridged-horn (sizes in cm: a=7.75, $b = 3$, $l = 3.6$, $A = 13$, $B = 9.25$, $L = 30.4$.): transmitting-mode effective height calculated by the CF and IF-model with different numbers of poles corresponding to a threshold thinning of 10^{-3}; (up) observation at the aperture boresight; (down) observation at ($\theta = 30°$, $\phi = 0°$). Dirac pulses at $\tau \approx z_A/c$ are not shown.

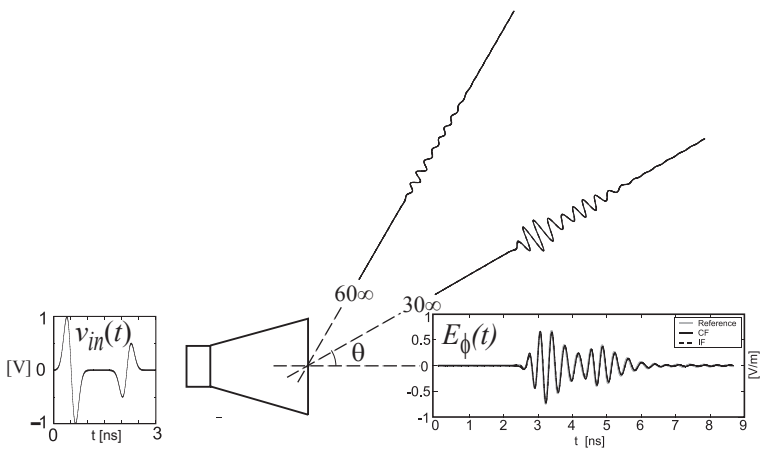

FIGURE 5.9. Pyramidal ridged-horn: far field radiation at distance from the aperture $r = 31cm$, computed by full FDTD and convolution in (1) when the input signal is a couplet of derivated gaussian pulses.

method provided that 20 and 24 pole-residue couplets are used for CF- and IF-model respectively.

5.3 Directive antennas

5.3.1 Statement of the problem

As previously stated, the computation of the time domain effective height requires the knowledge of the antenna current impulse response. An approximation, commonly adopted in the measurement context, replaces the knowledge of the antenna current with the field on a plane, say π_0 of normal vector $\hat{\boldsymbol{z}}$, placed at close proximity to the antenna (Fig.5.10). Relevant far field functions, such as the impulse response and the transfer function, are then obtained by a two-dimensional Radon transform (time-domain) (see previous section) or spectral Fourier transform (frequency domain) as

$$\boldsymbol{h}^T(\hat{\boldsymbol{r}},\tau) = -\frac{2}{\eta_0}\hat{\boldsymbol{r}} \times \iint_{\pi_0} \boldsymbol{E}_0^{\delta}(\boldsymbol{\rho},\tau + \frac{\hat{\boldsymbol{r}}\cdot\boldsymbol{\rho}}{c})ds \times \hat{\boldsymbol{z}} * \delta^{(1)}(\tau) \tag{5.20}$$

$$\boldsymbol{\mathcal{H}}(\hat{\boldsymbol{r}},\omega) = -2\frac{j\omega}{\eta_0}\hat{\boldsymbol{r}} \times \iint_{\pi_0} \tilde{\boldsymbol{E}}_0^{\delta}(\boldsymbol{\rho},\omega)e^{j\frac{\omega}{c}\hat{\boldsymbol{r}}\cdot\boldsymbol{\rho}}ds \times \hat{\boldsymbol{z}} \tag{5.21}$$

where the symbol '*tilde*' denotes the Fourier transform between $t \to \omega$ domains, $\boldsymbol{E}_0^{\delta}(\boldsymbol{\rho},t)$ with $\boldsymbol{\rho} = x\hat{\boldsymbol{x}}, y\hat{\boldsymbol{y}} \in \pi_0$, is the time-varying electric tangential field on π_0 in front of the antenna corresponding to a Dirac voltage pulse entering the antenna terminals. The latter function may be generally obtained by means of any time domain fullwave solver or by measurements. Such a representation obviously represents the antenna dynamics only in $z > 0$ (or $z < 0$) half space and it is really accurate only for directive antennas. Further approximations truncate the integration within a finite region of π_0 in the front of the antenna.

As previously stated, equations (5.20) and (5.21) need to be generally computed numerically except for very simple antenna geometries or unless that the near field is interpolated over proper time-independent functions having known Fourier transform. More general interpolating functions need to be introduced.

5.3.2 Hermite processing of the time-varying field

Provided that the plane π_0 (Fig.5.10) is placed at a close proximity to the antenna, the electric (or also the magnetic) field will be mostly concentrated within a small region of π_0. In other words we can suppose that the near field exhibits a compact support on π_0. In this hypothesis, an efficient choice

for the interpolating basis is the two-dimensional Associate Hermite Functions (hereafter denoted as AHF2) defined as

$$h_{mn}(x, y, w_x, w_y) = \frac{1}{\sqrt{\pi w_x w_y}\sqrt{2^{m+n} m! n!}} H_m(\tfrac{x}{w_x}) H_n(\tfrac{y}{w_y}) e^{-(\frac{x^2}{2w_x^2}+\frac{y^2}{2w_y^2})} \tag{5.22}$$

Here $H_m(\xi)$ is the mth Hermite polynomial. AHF2s (Fig.5.11) form a scalar orthonormal basis, they are spatially separable and show a compact support around ($x = 0$, $y = 0$) which can be controlled by the scaling factors $\{w_x, w_y\}$. Even functions, such as h_{00}, are useful to represent the co-polar field component, while the cross-polar is modeled by odd functions, for instance h_{11}. As the functions order (n, m) increases, the resulting support enlarges. The extreme values of a Hermite function have about equal amplitudes which is a rather useful feature to model close-to-the-edge field singularities and large radiating objects such as arrays.

Beside this choice, also the Hermite Rodriguez functions [14] could be considered for the interpolation of compact-support images, but it has been verified that the corresponding interpolation converges not uniformly and slower [12] than the AHF2 and that the interpolation accuracy is more sensible to the scale factor than in the case of AHF2.

The AHF2 share the same properties of the more conventional 1D associate Hermite functions and, in particular they are isomorphic with their Fourier transform, e.g.

$$\iint h_{mn}(x, y, w_x, w_y) e^{-j2\pi(\xi x+\eta y)} dxdy = (-j)^{m+n} h_{mn}(\xi, \eta, \tfrac{1}{2\pi w_x}, \tfrac{1}{2\pi w_y}) \tag{5.23}$$

The time-varying coefficients $\boldsymbol{g}_{mn}(\tau) = g_{x,mn}(\tau)\hat{\boldsymbol{x}} + g_{y,mn}(\tau)\hat{\boldsymbol{y}}$ for the near field approximation

$$\boldsymbol{E}_0^\delta(x, y, t) \simeq \sum_{m,n=0}^{N} \boldsymbol{g}_{mn}(\tau) h_{mn}(x, y, w_x, w_y) \tag{5.24}$$

are formally defined as the *two-dimensional Hermite transform* of the impulsive aperture field on π_0

$$\boldsymbol{g}_{mn}(\tau) = \iint_{\pi_0} \boldsymbol{E}_0^\delta(x, y, \tau) h_{mn}(x, y, w_x, w_y) dxdy \tag{5.25}$$

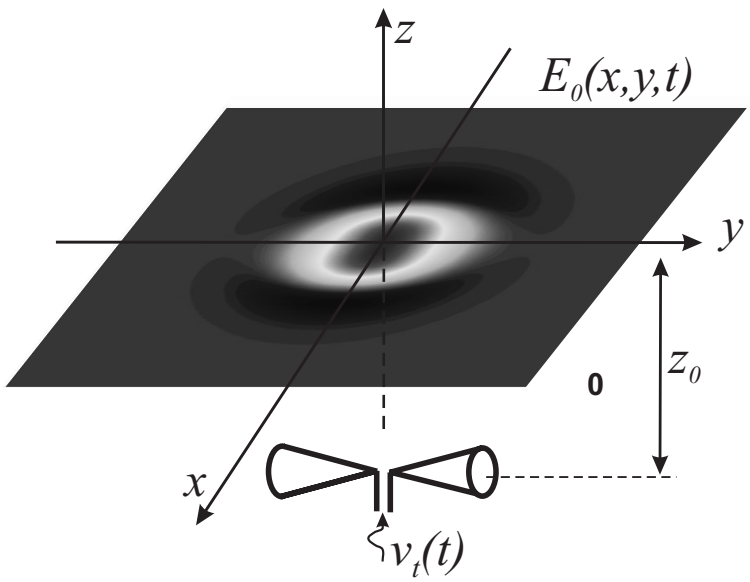

FIGURE 5.10. The relevant geometry for the Hermite processing of a time-varying near field.

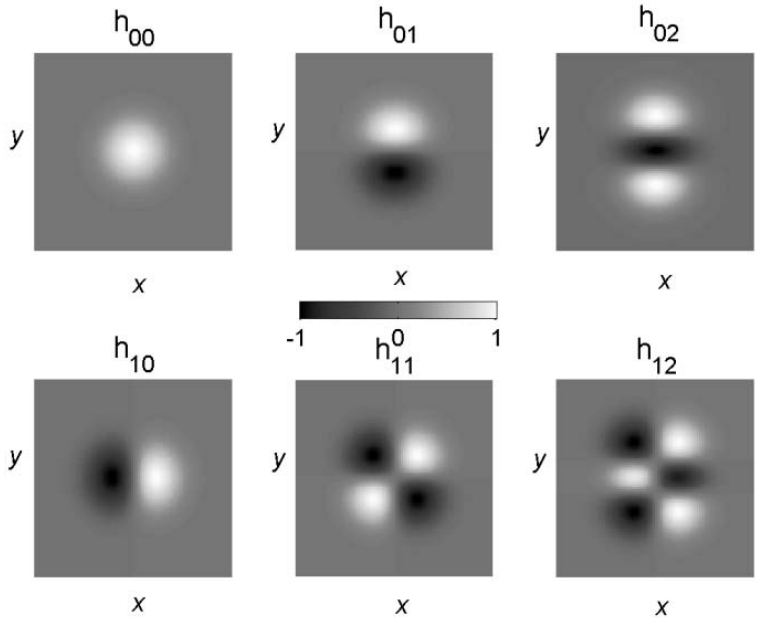

FIGURE 5.11. Some two-dimensional Associate Hermite functions having equal scaling factors $w_x = w_y$.

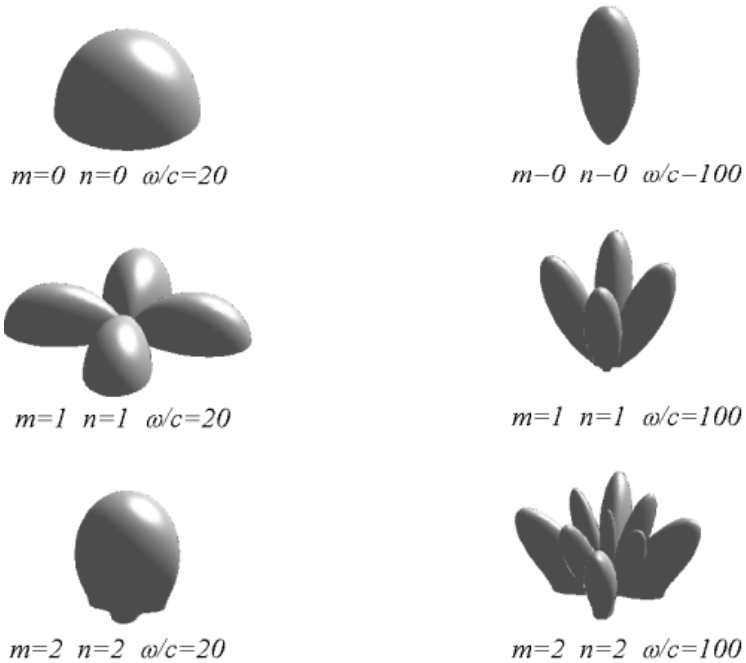

FIGURE 5.12. Examples of the $k-$domain AHF2 functions $|h_{mn}(-\frac{k_x}{2\pi}, -\frac{k_y}{2\pi}, \frac{1}{2\pi w_x}, \frac{1}{2\pi w_y})|$ of different orders plotted at some frequencies in angular coordinates (θ, ϕ).

Transfer function

According to expansion in (5.24), and thanks to the isomorphism in (5.23), it is easy to show that the antenna transfer function is given by

$$\boldsymbol{\mathcal{H}}^T(\hat{\boldsymbol{r}}, \omega) \simeq -2\frac{j\omega}{\eta_0}\hat{\boldsymbol{r}} \times \sum_{m,n=0}^{N} \tilde{\boldsymbol{g}}_{mn}(\omega) F_{mn}(k_x, k_y) \times \hat{\boldsymbol{z}} \tag{5.26}$$

The plane wave spectrum of the mnth AHF2 is $F_{mn}(k_x, k_y) = (-j)^{m+n} h_{mn}(-\frac{k_x}{2\pi}, -\frac{k_y}{2\pi}, \frac{1}{2\pi w_x}, \frac{1}{2\pi w_y})$, $k_x = \frac{\omega}{c}\hat{\boldsymbol{r}} \cdot \hat{\boldsymbol{x}}$ and $k_y = \frac{\omega}{c}\hat{\boldsymbol{r}} \cdot \hat{\boldsymbol{y}}$.

Because of the existence of a visibility region for the radiated field, e.g. $|k_{x,y}| \leq \omega/c$, only a portion of $F_{mn}(k_x, k_y)$ will contribute to the radiated fields. Fig.5.12 shows some examples of F_{mn} plots in spherical coordinates at some frequencies. Increase in the order (m, n) yields a larger number of lobes, while increasing the frequency forces the lobes to move toward the broadside.

The expansion coefficients, $\{\tilde{\boldsymbol{g}}_{mn}(\omega)\}$, are the only data to store at the purpose to regenerate the whole frequency-domain antenna dynamics. Moreover, as it will be recalled in the next paragraph, a further data compression can be achieved by pole-residue processing.

5.3.3 Impulse response

Denoting with S_{π_0} the compact support of $\boldsymbol{E}_0^{\delta}(x,y,t)$ on the π_0 plane, for instance a circle of $\rho_{\max}$ radius, the time-domain effective height can be approximated (see previous section) for signals with maximum frequency $f_{\max} \leq \rho_{\max}/c$ in terms of the plane-wave spectrum of each AHF2 pattern evaluated at the singular values of its own time-variant expansion coefficients. Therefore, denoting for instance with $\{s_{x,mnk}, g_{x,mnk}\}$ the pole-residue signature of the $g_{x,mn}(\tau)$ function, e.g. such that $g_{x,mn}(\tau) \simeq \sum_k g_{x,mnk} e^{s_{x,mnk}\tau}$, the $x-$component of the TD effective height is given by

$$h_x^T(\hat{\boldsymbol{r}},\tau) \simeq= -2\frac{1}{\eta_0}\hat{\boldsymbol{r}}\times \tag{5.27}$$

$$\sum_{m,n=0}^{N}\sum_{k=0}^{K_{mn}} T_{x,mnk} h_{mn}(\tfrac{js_{x,mnk}}{2\pi c}r_x, \tfrac{js_{x,mnk}}{2\pi c}r_y, \tfrac{1}{2\pi w_x}, \tfrac{1}{2\pi w_y}) e^{s_{x,mnk}\tau}$$

where $T_{x,mnk} = (-j)^{m+n} s_{x,mnk} g_{x,mnk}$, and $r_x = \hat{\boldsymbol{r}} \cdot \hat{\boldsymbol{x}}$ and $r_y = \hat{\boldsymbol{r}} \cdot \hat{\boldsymbol{y}}$. The pole-residue processing has the additional advantage to produce both time- and frequency-models of the UWB antenna by the same set of data since $\tilde{g}_{x,mn}(\omega) = \sum_k \frac{g_{x,mnk}}{j\omega - s_{x,mnk}} e^{-j\omega + s_{x,mnk} z_0/c}$.

5.3.4 Computational Issues

Since the Dirac pulse is not suited as input signal for numerical tools, a practically band-limited test signal $v_t(t)$, such as a Gaussian or derivated-Gaussian pulse, is considered for the computation of the time-varying near field $\boldsymbol{E}_0(x,y,t)$ on π_0. Denoting with $\{v_{mn}(t)\}$ the Hermite transform of $\boldsymbol{E}_0$ as in (5.25), the required $\{g_{mn}(\tau)\}$ coefficients of $\boldsymbol{E}_0^{\delta}$ are then obtained from $\{v_{mn}(t)\}$ by deconvolutions as explained in [70] and in the previous section. The pole-residue extraction can be executed by the Matrix Pencil method [71].

A critical task in the field approximation over the AHF2 set is the choice of the scaling factors $\{w_x, w_y\}$ which generally depends on the local scene context and strongly affects the expansion accuracy and efficiency. According to the theory in [15], a good rule to optimize the choice of the scale factor is that the radiated power of the interpolated distribution best matches the radiated power of the real field distribution. However this strategy is an *a-posteriori* one, since it requires the knowledge of the whole near-field dynamic and therefore it is not suitable to be incorporated into a time-domain solver for a run-time execution. Instead, it is desirable an *a-priori* selection of the scale factors which is related to the observable geometrical parameters, such as the antenna size and the distance between the antenna and the near-field observation plane. Since the support of $\boldsymbol{E}_0^{\delta}$ enlarges as the π_0 plane moves

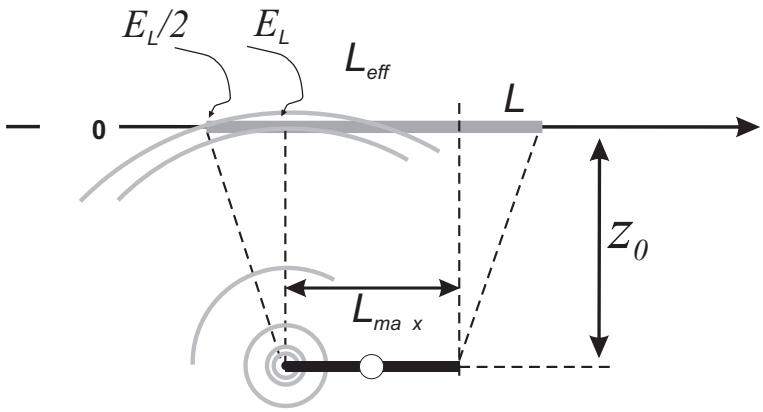

FIGURE 5.13. Geometry for the definition of the *antenna effective footprint* L_{eff} on π_0 according to a spherical radiation model from the antenna edges. E_L is the field amplitude on π_0 at the projections of the antenna boundary.

far from the antenna, at least in the near field, a robust *a-priori* choice of the scaling factor requires to account for both the antenna size and the distance z_0 from the expansion plane. At this purpose we preliminarily define an *effective antenna footprint* L_{eff} on π_0 under the simplifying hypothesis of spherical-wave radiation mechanism from the antenna edges (see Fig.5.13).

Denoting with $\Delta l \simeq 2z_0$ the distance on the π_0 plane between the projection of the antenna boundary and the point where the spherical wave emerging from the antenna edges attenuates to one half its maximum amplitude, we set

$$L_{eff}(z_0) = L_{\max} + 4z_0 \tag{5.28}$$

It is here assumed that the scaling factor is a function of the sole L_{eff}. Among several options, we experimentally found that a good choice can be

$$w_x = w_y = \frac{\lambda_{\min}}{4} \log(10\frac{L_{eff}}{\lambda_{\min}}) \tag{5.29}$$

where $\lambda_{\min}$ is the lowest interested frequency in the modeling. Under this assumption, the accuracy of the Hermite expansion is rather insensitive to the position of the π_0 plane as it will be shown in the Examples Section.

The Hermite Transformation integrals in (5.25) theoretically extend to infinity, however near-field data are available only within a finite sub-domain of π_0. Such a truncation of the observation domain yields a limitation on the order of those AHF2s which can be retained in the field interpolation since the support of each AHF2 is roughly bounded by the first and the last roots of the corresponding Hermite polynomial and enlarges along with the function order. The following argument may be followed. An accurate strategy to

numerically compute the Hermite transform in (5.25) could be the N-points Gauss-Hermite integration rule [72]

$$\int_{-\infty}^{+\infty} f(u)e^{-u^2}du \simeq \sum_{j=1}^{N} A_j f(u_j^{(N)}) \tag{5.30}$$

where $\{u_j^{(N)}\}$ are the roots of the Nth order Hermite polynomial and $\{A_j\}$ are proper integration weights. By applying this formula to (5.25), and accounting for the presence of scaling factors, it is easy to show that

$$\boldsymbol{g}_{mn}(\tau) \simeq \sum_{i=1}^{M}\sum_{j=1}^{N} A_i A_j \left[\boldsymbol{E}_0^{\delta} h_{mn} e^{\frac{x^2}{2w_x^2}+\frac{y^2}{2w_y^2}}\right]_{\substack{x=\sqrt{2}w_x u_i^{(M)} \\ y=\sqrt{2}w_y u_j^{(N)}}} \tag{5.31}$$

In order to apply the above formula to a truncated $L_0 \times L_0$ domain, $(-\frac{L_0}{2} \leq x, y \leq \frac{L_0}{2})$, all the required roots need to lay within that region. Therefore the highest-order, N and M, of AHF2s are such that the largest roots of the corresponding Hermite polynomials are constrained to

$$u_i^{(M)} \leq \frac{L_0}{2\sqrt{2}w_x} \qquad u_j^{(N)} \leq \frac{L_0}{2\sqrt{2}w_y} \tag{5.32}$$

Fig.5.14 shows the largest roots of the first $N = 50$ orders Hermite polynomials. Due to the non linearity of the curve, the number of Hermite functions to be retained in the near field interpolation is as more sensible to the size of the observation region as this becomes larger (e.g. roughly for $u_N^{(M)} > 5$). In other words, the roots come closer (approach) as the order of Hermite function increases.

Another well investigated consequence [78] of the observation region truncation is that the far field data are meaningful only within the solid angle formed by the edges of the antenna and the edge of the finite observation region. By parametrizing the size L_0 of near-field data domain on π_0 as $L_0 = L_{eff} + 2pz_0$ (p is an integer number), the antenna transfer function $\boldsymbol{\mathcal{H}}^T(\hat{\boldsymbol{r}}, \omega)$ will be considered only for angles $-\theta_0 \leq \theta \leq \theta_0$ where θ_0 is such that $\tan\theta_0 = \frac{L_0 - L_{\max}}{2z_0} = (p+2)$. From this formula it is possible to select the size of the numerical computation region in order to obtain the desired angular domain of the transfer function.

5.3.5 Numerical Examples

The applicability and the accuracy of the method are now investigated with reference to two examples with different angular spreading of the radiated field, e.g. an aperture-type antenna, and an UWB planar dipole-like antenna.

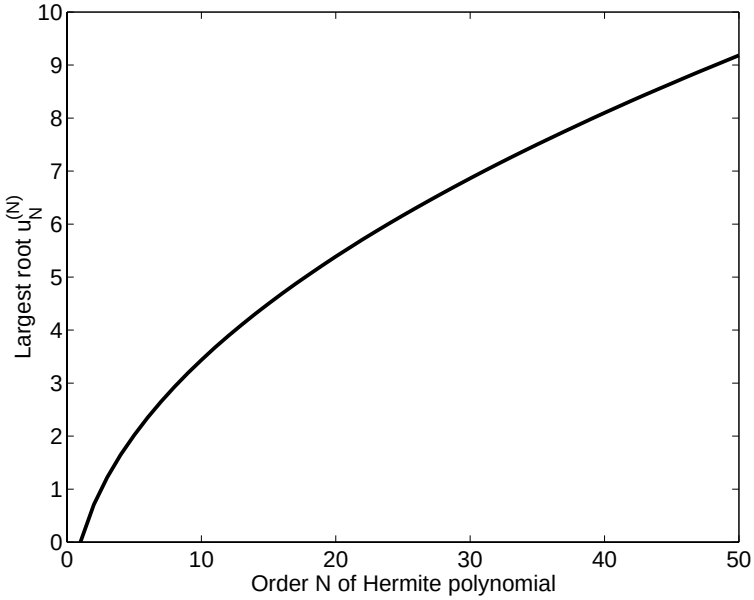

FIGURE 5.14. Largest roots $u_N^{(N)}$ of the Hermite polynomials $H_N(u)$.

In both the examples, time-varying relevant fields for the 2D Hermite transform are computed by a Finite-Difference Time-Domain (FDTD) tool. Far-field solutions obtained with the proposed model will be compared with a reference solution obtained by an independent FDTD simulation whose computational domain is large enough to include some field test points in front of the π_0 plane. Differences among reference fields ($\boldsymbol{E}_1$) and reconstructed fields ($\boldsymbol{E}_2$) by the Associate Hermite functions are discussed according to the normalized root mean square (r.m.s.) error $\varepsilon(E_1, E_2) = \sqrt{||E_1 - E_2||_2/||E_1||_2}$, (with $||\cdot||_2$ denoting the L_2 norm respect to (x, y) coordinates).

Aperture-radiating antenna

A reference ultra-wideband ridged horn (CRH) antenna having (4GHz - 10GHz) band, already used as a test case in previous papers [46], is here considered.

The test signal to stimulate the antenna response in the required band is a Gaussian pulse $v_t(t) = V_0 \exp[\frac{-(t-\tau_0)^2}{2T_0^2}]$ with parameters, $V_0 = 1V$, $T_0 = 35ps$ and $\tau_0 = 200ps$. The π_0 plane is placed at a distance $z_0 = 2.1cm$ from the horn aperture (corresponding to half a wavelength in the mid-band). The maximum size of the aperture is $L_{\max} = 10.5cm$ and therefore the effective aperture footprint on π_0 computed by (5.28) is $L_{eff} \simeq 19cm$. The observation region on π_0, e.g. the domain where the antenna near-field will be processed, is a square of side $L_0 \simeq 2L_{\max}$. Under this choice, the transfer function could

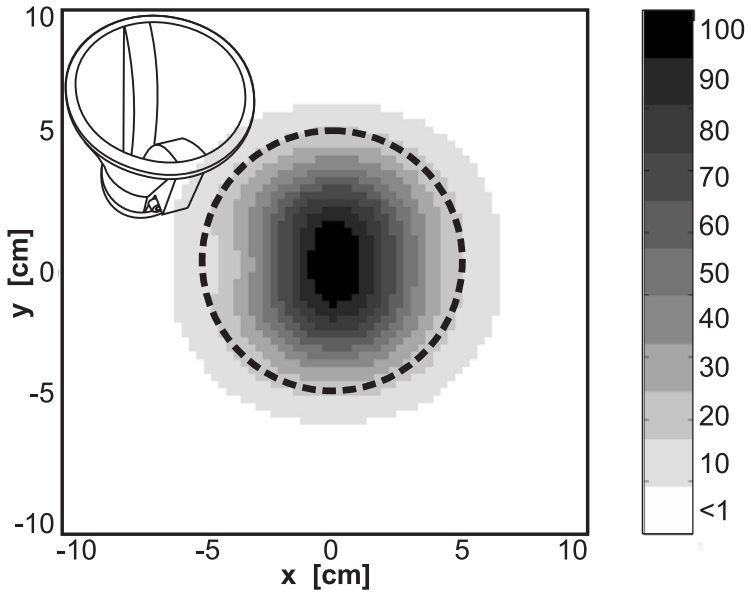

FIGURE 5.15. Normalized energy $e(x,y) = ||\boldsymbol{E}(\cdot,t)||_2$ radiated by the circular ridged horn on the plane π_0 placed at distance $z_0 = 2.1cm$ from the antenna aperture. The circle indicates the antenna rim positon.

be virtually computed within the angular domain $|\theta| < 68°$.

The near field energy, e.g. the L_2 norm respect to time, $e(x,y) = ||\boldsymbol{E}(\cdot,t)||_2$, is expected to be well concentrated over the expansion plane π_0 right in front of the aperture (Fig.5.15).

The scaling factors for the Hermite processing are chosen according to (5.29) as $w_x = w_y = 3.1cm$. In this case it is shown in Fig.5.16 that the relative mean square error of the reconstructed field $\boldsymbol{E}'_0(x,y,t) \simeq \sum_{m,n=0}^{N} \boldsymbol{v}_{mn}(\tau) h_{mn}(x,y,w_x,w_y)$ compared with the original field $\boldsymbol{E}_0(x,y,t)$ is rather insensitive to the position z_0 of the observation plane. It was experienced that the same condition roughly holds also for different kinds of antennas.

The energy spectrum $||v_{x,mn}(\tau)||_2$ of the Hermite coefficient for E_{0x} and E_{0y} components of orders $n, m \leq 10$ (Fig.5.17) shows a chessboard-like distribution, interleaved among x- and y-components, with a high localization of the most excited AHF2s in the lower part of the band (small n and m). In particular, h_{00} and h_{11} functions dominate for $y-$ (co-polar) and $x-$components (cross-polar) respectively. By considerations in Section 5.3.4 (see equation (5.32)) the near-field domain size is such that $2.35(u_6^{(6)}) < \frac{L_0}{2\sqrt{2}w_x} < 2.65(u_7^{(7)})$ and therefore the highest order of AHF2 to be considered is roughly $N = M = 7$.

According to this expansion, the transient near field on π_0 is reconstructed

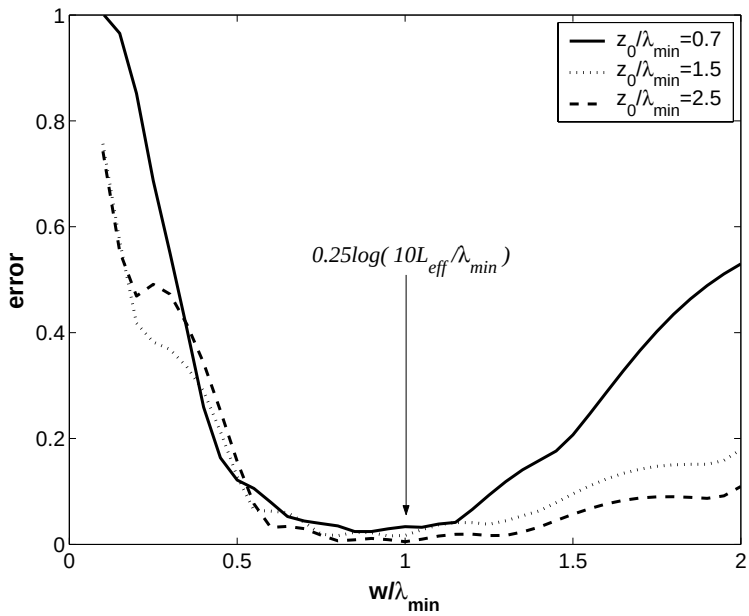

FIGURE 5.16. CRH antenna: reconstruction r.m.s. error $\varepsilon(E_{0,y}, \sum_{m,n} v_{y,mn} h_{mn,y})$, at time $t = 0.75ns$ vs. the scaling factor $w_x = w_y = w$ for different distances z_0 of the observation plane to the antenna and therefore of the effective antenna footprint L_{eff} on π_0. In this case $\lambda_{\min} = 3cm$.

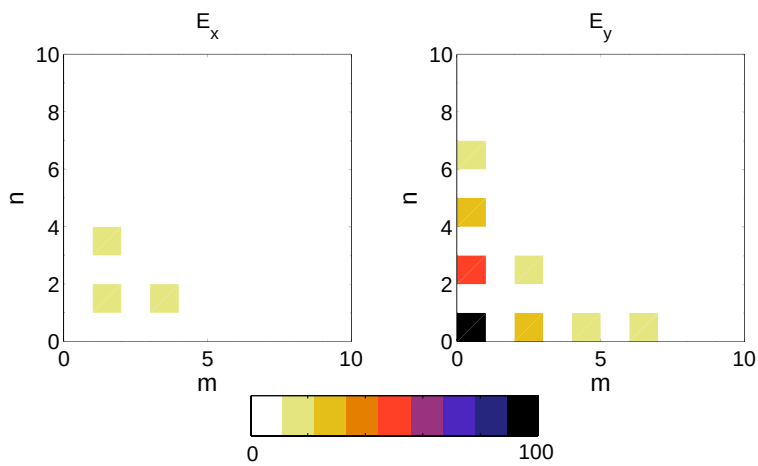

FIGURE 5.17. CRH antenna: energy spectrum of the Hermite coefficients for the field interpolation on π_0.

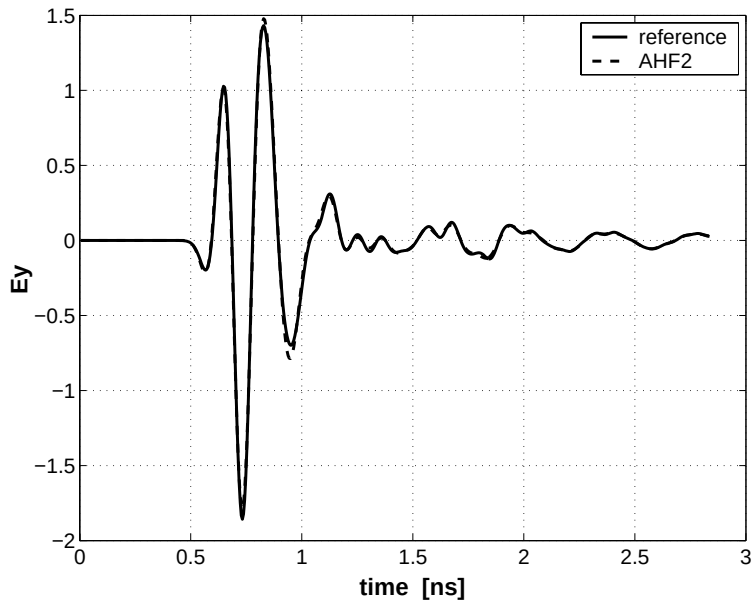

FIGURE 5.18. CRH antenna: interpolation of the near-field (in normalized units) on the π_0 plane at point $x_0 = y_0 = 4.5cm$ by the two-dimensional Associate Hermite series $E_y(x_0, y_0, t) = \sum v_{y,mn}(t) h_{mn}(x, y, w)$ with $N = M = 7$.

with good accuracy both in the early transient and in the signals tail as shown in Fig.5.18.

The angle-frequency transfer function plot, as computed by the proposed Hermite processing at $\phi = 90°$ plane is presented in Fig.5.19. The high-pass nature of the antenna is clearly evident as well as the nearly constant group delay at the boresight which indicates a reduced distortion of the transmitted pulse.

Values of transfer function at boresight observation and off the boresight have been further used to regenerate the far field dynamics corresponding to $\tilde{v}_t(\omega) = F[v_t(t)]$ input function according to $\tilde{\boldsymbol{E}}(\boldsymbol{r}, \omega) \propto \tilde{v}_t(\omega) \boldsymbol{\mathcal{H}}^T(\hat{\boldsymbol{r}}, \omega) \frac{e^{jkr}}{r}$. Results in Fig.5.20 are compared with reference solutions and it can be appreciated a good reconstruction of the field even when the only h_{00} and h_{20} functions are considered on the boresight observation, and the h_{00} plus h_{11} off the boresight.

UWB dipole

An Ultra-wideband planar dipole with elliptical branches (Agrawall dipole [79]) is placed in front of a finite reflecting plane (Fig.5.21) with the purpose to concentrate the radiation mainly in $z > 0$ half space.

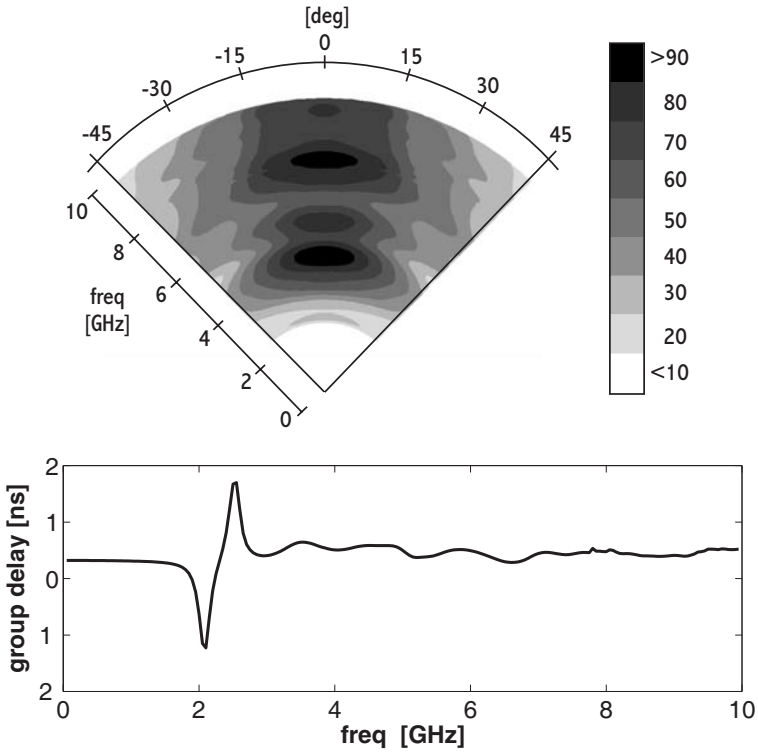

FIGURE 5.19. CRH antenna: transfer function (in normalized units) at $\phi = 0°$, amplitude of the θ-component and group delay along the boresight.

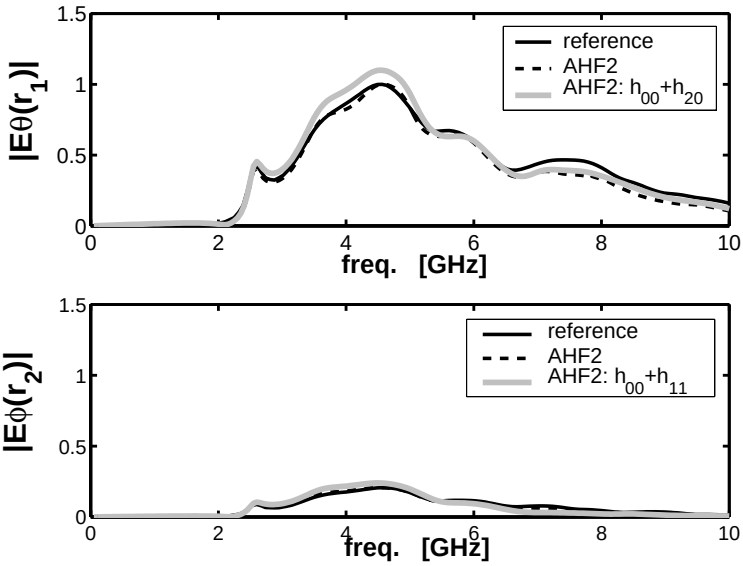

FIGURE 5.20. CRH antenna: comparison between reference solution and AHF2 reconstructions for the far-field data (normalized units) at the boresight, $P_1 = (r_1 = 15cm, \theta = 0°, \phi = 0°)$, and off-the-boresight, $P_2 = (r_2 = 48.8cm, \theta = 18°, \phi = 45°)$.

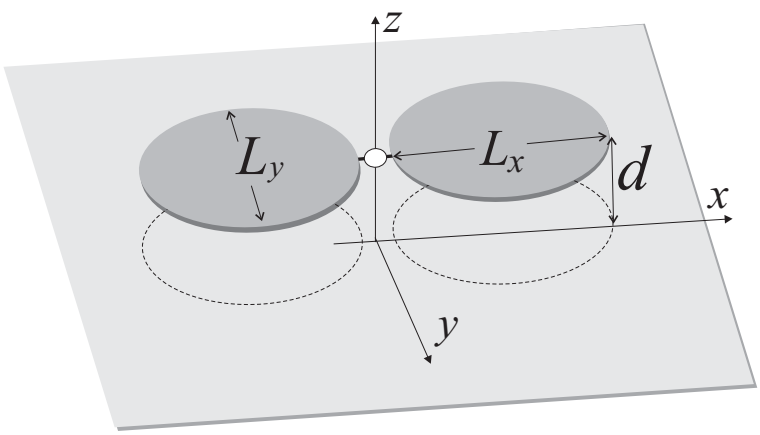

FIGURE 5.21. Agrawall dipole: geometry size: $L_x = 5cm$, $L_y = 4.6cm$, $d = 2.4cm$. Reflecting panel size: $20 \times 20cm^2$.

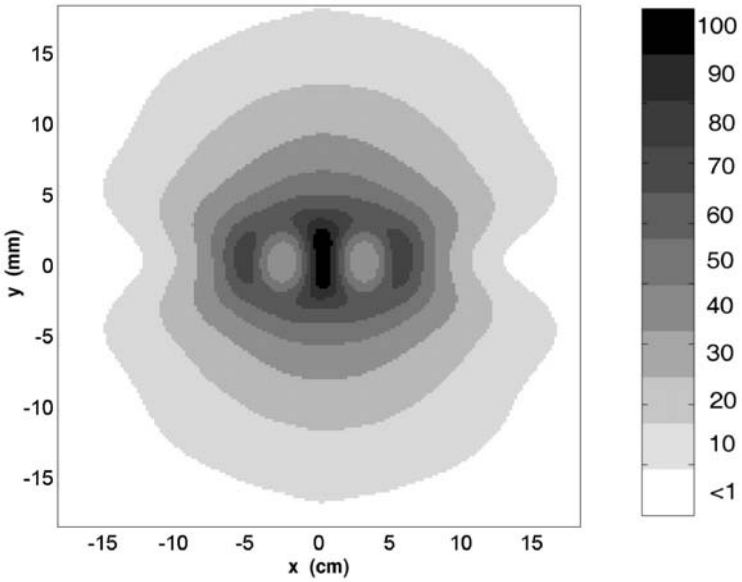

FIGURE 5.22. Agrawall dipole: near field energy on the plane π_0 at a distance $z_0 = 18mm$ from the antenna when it is sourced by a gaussian pulse with parameters $To = 24ps$ and $\tau_0 = 130ps$.

The antenna is sourced by a Gaussian pulse with parameters $T_0 = 24ps$ and $\tau_0 = 130ps$. This kind of geometry is a hard test for the AHF2 interpolation since, unlike the case of aperture-like antennas, the radiated near-field sensibly spreads on the π_0 plane as the time goes on. Departing interference fringes therefore leave a null in front of the antenna gap at some time intervals. As a consequence, it is expected that the radiated energy is less concentrated in front of the antenna (see Fig.5.22), the field support on π_0 will enlarge along with the time and a big set of AHF2 could be involved in the field processing.

By placing a square observation plane π_0, of size $L_0 = 40cm$, at a distance $z_0 = 1.8cm$ from the antenna and choosing equal scaling factors $w_x = w_y = 2.46cm$, the maximum order of the AHF2 which could be computed by the Hermite Transform (according to equation (5.32)) will be $N = M = 22$. Fig.5.23 shows the energy spectrum of the first $n, m < 15$ time-variant interpolation coefficients. As expected, the diagram is less concentrated than in the CRH example and therefore a larger number of terms will be required for an accurate reconstruction of the antenna dynamics. Snapshots of the near-field, interpolated on the π_0 plane by the Hermite base (Fig.5.24), show a good agreement with the original data even when the radiated waveforms move far from the domain centre. Some difficulties begin to arise when the wavefront approaches the boundary of the observation plane.

The far-field (Fig.5.25) is reconstructed, as in the previous example, with

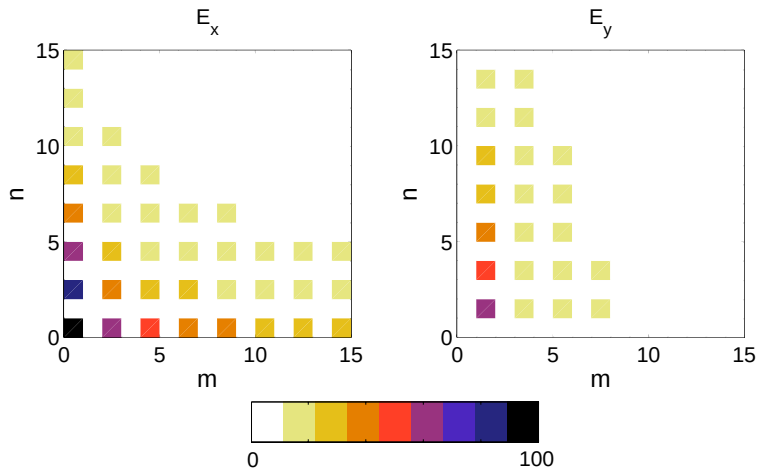

FIGURE 5.23. Agrawall dipole: energy spectrum of the Hermite coefficients for near-field interpolation.

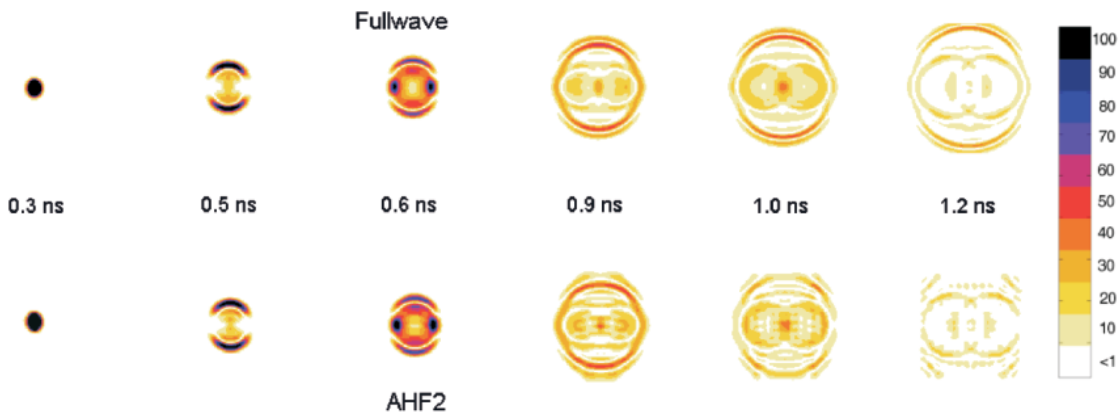

FIGURE 5.24. Agrawall dipole: some snapshots of the near field ($|E_x(x, y, t)|$ component) on the observation plane π_0 placed at a distance $z_0 = 18mm$ from the antenna as computed by FDTD (upper line) and interpolated by AHF2s (lower line).

good accuracy up to 4GHz, (e.g. in the antenna band-width), after which the reconstructed field presents some discrepancies with the reference data.

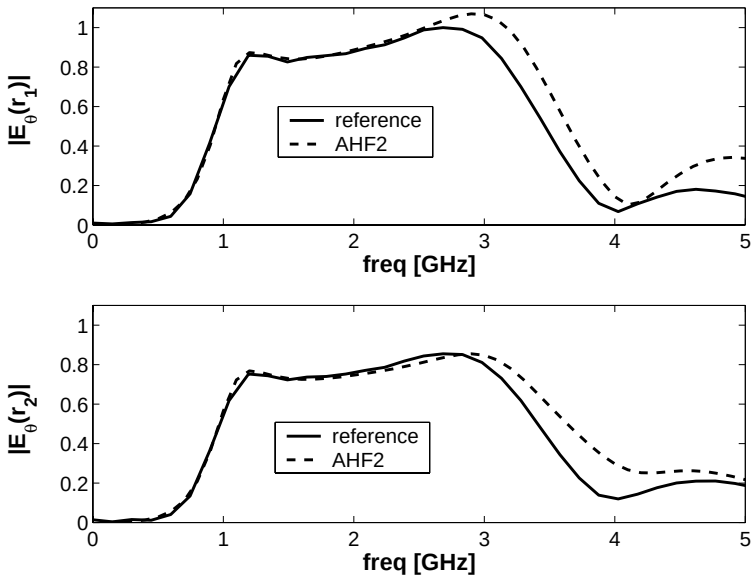

FIGURE 5.25. Agrawall dipole: comparison between reference solution and AHF2 reconstructions for the far field $r|E_\theta|$ at angles $(\theta = 0°, \phi = 0°)$ -up- and $(\theta = 12°, \phi = 0°)$ -down. Data in normalized units.

The time-domain effective height is computed according to (5.27) by using the same data of the transfer function. It can be observed in Fig.5.26 an approximate second-order derivative behavior of the UWB dipole, e.g. three distinct finite-width pulses with alternated polarity.

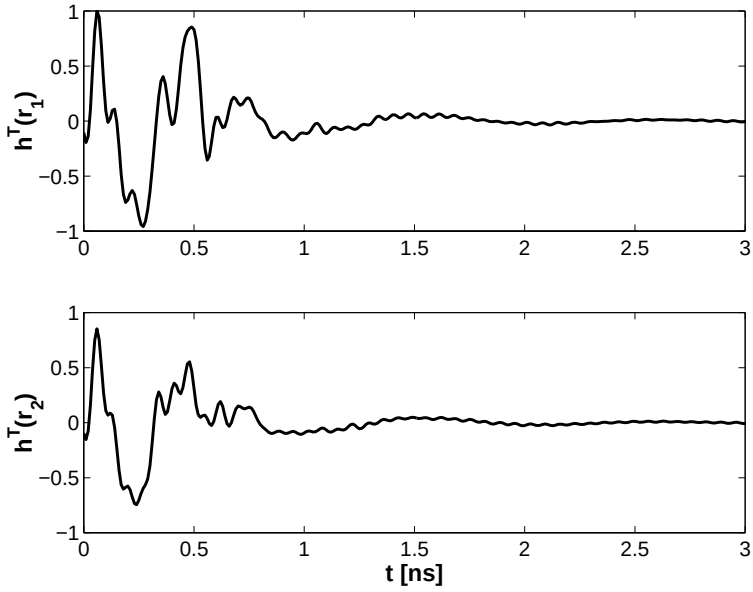

FIGURE 5.26. Agrawall dipole: time-domain effective height (in normalized units) at angles ($\theta = 0°, \phi = 0°$) -up- and ($\theta = 12°, \phi = 0°$) -down- as computed by AHF2 processing.

Chapter 6

TD Analysis of Couplings in Pulsed Arrays

6.1 Introduction

Preliminary physical investigations on pulsed arrays have been reported in [23], [24], [25], [27], where coupling between radiating elements is usually neglected and emphasis is mainly devoted to conditions for grating lobe cancellation, permitting the design of sparse arrays. The additional reduction in sidelobe levels is due to the combined angular and temporal spreading of the energy radiated by the antenna, as explained in a previous chapter.

The presence of the *temporal* dimension in the radiation phenomenology [25] plays an important role also in the coupling estimation, as it will be explained in this chapter.

In the frequency domain, for the case of narrow-band antennas, the well-established theory of the active element factor [80] permitted to predict the malicious effect of antenna mismatch and scan blindness in phased arrays.

In the time domain, any impulse radiating antenna has to be considered as an angular-temporal filter, in the sense that it not only distributes the power along the observation angles, but it also introduces a signal distortion on the input pulse [37] depending on the antenna shape and on the observation angle. In array configurations, the latter distortion effect can be potentially emphasized at some scanning direction and according to the duration of the input signal.

Fullwave models of real TD arrays including coupling have been recently proposed [81], [82] for the particular case of infinite periodic geometries where the inter-antenna interaction is directly taken into account by the excitation of time-domain Floquet waves. In finite arrays, like those proposed for ultra-wideband applications in complex scenarios, the Floquet-waves framework does not apply and the time domain coupling phenomenology is hidden in the overall

system response.

This chapter presents a simple physical model of the time domain coupling for impulse-radiating finite arrays aimed to identify the role of the scan angle, the input signal duration, the repetition rate of the input pulse train and finally the impulse response of the single antenna. Expressions for the time domain (TD) effective height and effective array factor are retrieved, and an investigation on coupling echoes and their distorting effect on the main signal permits to obtain conditions to reduce coupling, even in compact configurations with very small inter-element distances.

6.2 Basic definitions: impulse response operator and TD array factor

The antenna model of Fig.1a is considered for the following discussion. The antenna input port is connected, through a transmission line of characteristic impedance R_0, to a real voltage source $v_{in}(t)$ with internal resistance R_g=R_0. The time-dependent port variables are the TD reflection coefficient $\gamma_a(t)$ or, alternatively, the TD input impedance or admittance $z_a(t)$, $y_a(t)$. These functions have the meaning of input impulse responses working as convolution operators on nodal or on travelling wave functions such as: $v^-(t) = \gamma_a(t) * v^+(t)$, or $v(t) = z_a(t) * i(t)$, where '*' denotes convolution, $v^+(t) = \frac{1}{2}v_{in}(t - t_g)$ and $v^-(t)$ are the travelling inward and outward voltage waves, t_g is the time delay along the line (supposed zero, for simplicity) and $v(t), i(t)$ are the antenna nodal voltage and current ($v = v^+ + v^-$, $i = i^+ + i^-$, $i^+(t) = \frac{1}{R_0}v^+$). As already stated in the previous chapter, time-dependent radiation is generally described by the *transmitting-mode TD effective height* [37] $\boldsymbol{h}^t(\hat{\boldsymbol{r}}, t)$ which accounts for the antenna-source mismatch.
A set of N identical antennas, each excited by an inward travelling current $i_n^+(\tau)$ is now considered. As already described in Chapter 4, the total field radiated by the array, when the coupling effects are neglected ($\boldsymbol{h}_n^t = \boldsymbol{h}^t$) is

$$\boldsymbol{E}^A(\boldsymbol{r}, t) = -\frac{\eta_0}{4\pi rc}[\boldsymbol{h}^t(\hat{\boldsymbol{r}}, \cdot) * \mathcal{F}(\hat{\boldsymbol{r}}, \cdot)](t - \frac{r}{c}) \tag{6.1}$$

where $\mathcal{F}(\hat{\boldsymbol{r}}, \tau) = \sum_{n=1}^{N} i_n^+(\tau + t_n(\hat{\boldsymbol{r}}))$ is the TD *array factor* with $t_n(\hat{\boldsymbol{r}}) = \frac{\boldsymbol{r}_n \cdot \hat{\boldsymbol{r}}}{c}$ and $\boldsymbol{r}_n$ tags the m-th antenna position [23].

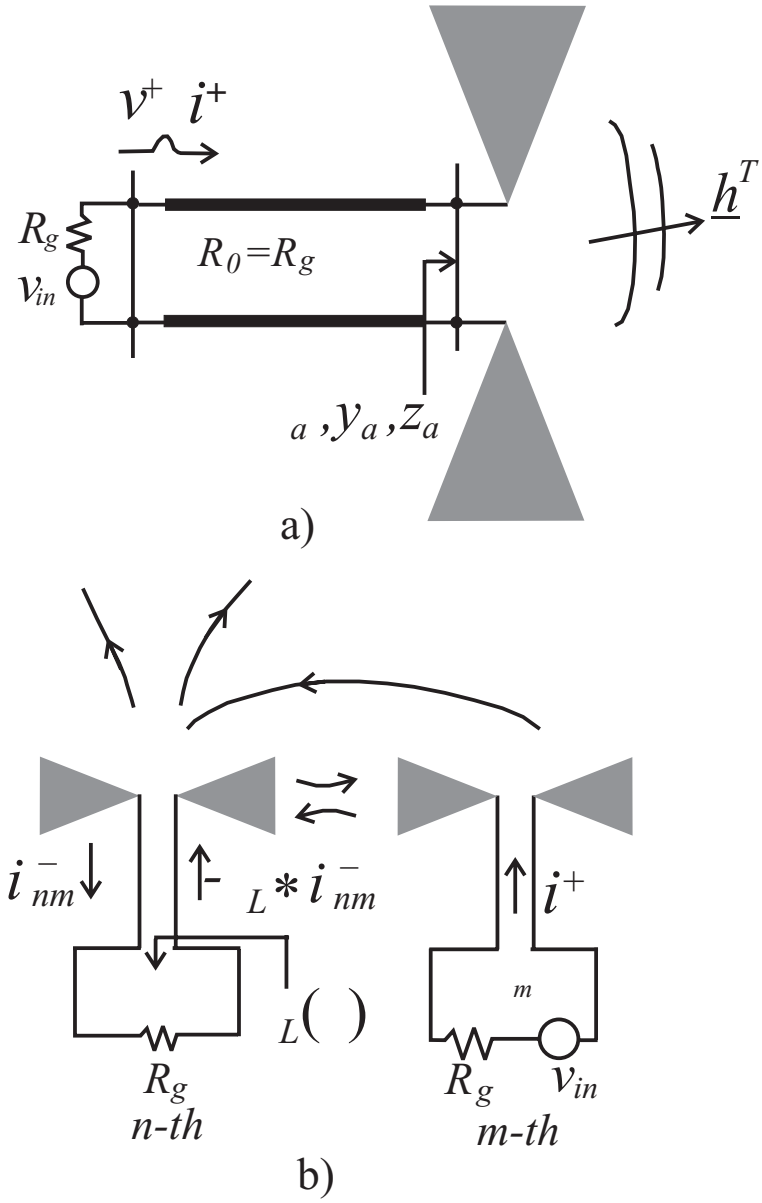

FIGURE 6.1. a)Time-dependent antenna input and radiation functions; b) Current wave components at the nth antenna port due to the coupling with the $i_m^+(t)$ current at the mth antenna.

6.3 TD active array factor and active element factor

The conventional array coupling model in the frequency domain [80] needs to be properly modified to obtain the time-dependent coupling scheme. The above model requires the total port current, e.g. the superposition of direct and reflected currents, and supposes a perfect matching between the antenna and the source. This last condition, as discussed in [37], needs to be dropped when considering an UWB antenna since the multiple reflections between antennas and loads are already embedded into the TD effective height. Therefore, with reference to Fig.1b, the total nodal port current $i_{T,n}(t)$ at the n-th antenna, when coupled with all the others, is

$$i_{T,n}(t) = i_n^+(t) - \gamma_{a,n}(t) * i_n^+(t) + \sum_{\substack{m=1 \\ m\neq n}}^{N} [i_{nm}^-(t) - \gamma_{L,n}(t) * i_{nm}^-(t)] \tag{6.2}$$

where $\gamma_{a,n}(\tau)$ is the *embedded* time-dependent reflection coefficient operator of the n-th antenna accounting for the presence of the passive external environment, e.g. of other antennas, each connected to its own load. $\gamma_{L,n}(\tau)$ is the embedded reflection coefficient of the same antenna but looking toward voltage source ($\gamma_{L,n} = -\gamma_{a,n}$, if the source is directly connected to the antenna); $i_{nm}^-(t)$ is the received outward-traveling current at n-th antenna port (from the antenna to the load) due to the m-th antenna direct current wave $i_m^+(t)$, under the hypothesis that the antenna is terminated by a matched load corresponding to the embedded input impedance $z_L = z_{a,n}(t)$. By linearity, outward coupling currents $i_{nm}^-(t)$ can be related to the source currents $i_m^+(t)$ at the m-th antenna by the convolution integral $i_{nm}^-(t) = -s_{nm}(t) * i_m^+(t)$, when all the antennas, other than the m-th, are connected to the internal load R_g of their source. The function $s_{nm}(\tau)$ is a time-dependent coupling operator which accounts for the multiple bouncing among radiators under perfect matching condition of the "victim" (m-th) antenna. The antenna effective height operator needs to be applied only to total inward waves $i_{T,n}^+ = i_n^+ - \gamma_{L,n} * \sum_{\substack{m=1 \\ m\neq n}}^{N} i_{nm}^-$. The resulting time-dependent *active* array factor, including inter-antenna coupling, is therefore

$$\mathcal{F}_A(\hat{\boldsymbol{r}}, \tau) = \sum_{n=1}^{N} i_n^+(\tau + t_n(\hat{\boldsymbol{r}})) - \tag{6.3}$$
$$\sum_{n=1}^{N} \gamma_{L,n}(\tau) * \sum_{\substack{m=1 \\ m\neq n}}^{N} s_{nm} * i_m^+(\tau + t_n(\hat{\boldsymbol{r}}))$$

The last summation shows the spatial and temporal distortion of the input signals due to the coupling among antennas. Note that this expression differs from the corresponding frequency domain function for the presence of the $\gamma_{L,n}(\tau)$ operator and since it applies to travelling waves rather than to nodal functions.

The field radiated by the array, when only the k-th element is driven, is obtained from (6.3) and (6.1) as

$$\boldsymbol{E}_k(\boldsymbol{r},t) = -\frac{\eta_0}{4\pi rc}[\boldsymbol{h}_k^t(\hat{\boldsymbol{r}},\cdot) * i_k^+(\cdot)](t-\frac{r}{c}) \tag{6.4}$$

where $\boldsymbol{h}_k^t$ is the TD *active* effective height of the k-th radiating element

$$\boldsymbol{h}_k^t(\hat{\boldsymbol{r}},\tau) = \boldsymbol{h}^t(\hat{\boldsymbol{r}},\tau) - \tag{6.5}$$
$$\sum_{\substack{n=1\\n\neq k}}^{N} \gamma_{L,n}(\tau) * s_{nk}(\tau) * \boldsymbol{h}^t(\hat{\boldsymbol{r}},\tau + t_n(\hat{\boldsymbol{r}}) - t_k(\hat{\boldsymbol{r}}))$$

The distortion function, e.g. the summation in (6.3), depends on the source-antenna mismatch as well as on the mutual distances among radiators through the term $t_n(\hat{\boldsymbol{r}}) - t_k(\hat{\boldsymbol{r}})$.

6.4 Investigation on coupling echoes

Some qualitative information about the distortion effect and in particular about the role played by the scan direction, the pulse width, the pulse repetition rate and the array density, can be earned by introducing some simplifying hypothesis. With reference to (6.3), it is supposed a regular alignment of antennas along $\hat{x}$ axis with inter-element spacing d. The sourcing currents are trains of equi-amplitude delayed waveforms $g(t)$, e.g. $i_n^+(\tau) = g(t) * \sum_{l=1}^{N_L} \delta(\tau - nt_s - lT_p)$ where T_p is the repetition rate and $t_s = \frac{d}{c}\sin\theta_0$ a linear delay to achieve beam scanning along θ_0. It can be convenient to further suppose that:

i) the coupling factors s_{nm}, which can not be generally expressed into analytical forms, may be approximated by the expression $s_{mn}(\tau) \sim S_0 \frac{\delta(\tau - r_{nm}/c)}{r_{nm}}$ where $r_{nm} = |r_n - r_m|$ is the distance between elements and S_0 a constant factor. It is therefore assumed that the coupling current i_{nm}^- on the n-th antenna is an undistorted shifted replica of the driving current on the m-th antenna which is attenuated according to the far field rule $1/r_{nm}$;

ii) each antenna has a same embedded reflection coefficient. This is reasonably true for large arrays. Additionally, this function is supposed to be frequency independent, at least within the band of interest, e.g. $\gamma_{L,n}(\tau) = \Gamma_o\delta(\tau)$. It will be shown in the Example section that such simplified assumptions however permit to model the response of real array.

6.4.1 Coupling for Dirac pulse input signals

Within the additional assumption that the driving signal is a Dirac pulse, e.g. $g(t) = \delta(t)$, the active array factor becomes

$$\mathcal{F}_A(\hat{\boldsymbol{r}}, \tau) = \sum_{n=1}^{N} \sum_{l=1}^{N_L} \delta(\tau + t_n - nt_s - lT_p) - \sum_{n=1}^{N} \sum_{\substack{m=1 \\ m \neq n}}^{N} \frac{G_0}{|n-m|} \sum_{\ell=1}^{N_L} \delta(\tau + t_n - mt_s - \ell T_p - |n-m| \frac{d}{c}) \tag{6.6}$$

where $G_0 = S_0 \Gamma_0 / d$. The second summation accounts for the echoes generated by the coupling, e.g. by antenna diffractions. Echoes' delays depend on observation angle, element position, scanning direction and pulse position in the train, and they are superimposed to the direct pulses (first summation).

The above formula could be useful to predict a real coupling when the parameters S_0/d and Γ_0, and hence G_0, are retrieved as average values from measurements or from antenna simulations. To emphasize the visualization of the echoes, the parameter G_0 is now set to 1. A more realistic value will be considered in the next section. Within this assumption, and for the case of $N = 4$ elements, $N_L = 1$ and inter-element spacing $d = 4cm$, Fig.6.2 shows the arrival time of the direct pulses and of the echoes for some scanning angles and different observation directions. It is possible to see that echoes emerging from different antennas may be partially superimposed, depending on the scan angle and observation point.

In particular, along the main lobe $t_n(\theta_0) = nt_s$ and therefore

$$\mathcal{F}_A(\hat{\boldsymbol{r}}, \tau) = N\delta(\tau) - \sum_{n=1}^{N} \sum_{\substack{m=1 \\ m \neq n}}^{N} \frac{G_0}{|n-m|} \delta(\tau + [(n-m)\sin\theta_0 - |n-m|] \frac{d}{c})$$

It can be proved that the earliest echo in the scan direction is emitted at time

$$t_{e,1} = (1 - |\sin\theta_0|) d/c \tag{6.8}$$

Fig.6.3 and Fig.6.4 display the arrival time of the echoes with respect to the direct pulse along the main beam at two different angles. In accordance to (6.8), as the scan angle approaches the endfire direction, the delay of the first echoes reduces to zero. In that case the first echoes and the direct pulses are fully synchronized and the coupling may produce sensible distortion to the radiated signal.

If $N_L > 1$, e.g. in the case of multiple transmitting pulses, an incoming signal belonging to the direct pulse train can be distorted by the coupling

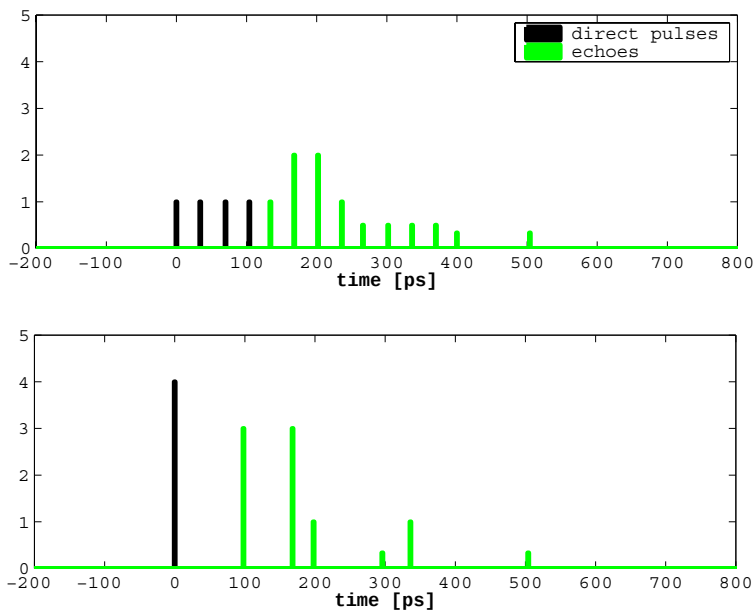

FIGURE 6.2. Delay time of the direct pulses and of the coupling echoes for a $N = 4$ element array with spacing $d = 4cm$, main lobe in $\theta_0 = 15°$ and observation in $\theta = 0°$ (up) and $\theta = 15°$ (bottom). It has been assumed $G_0 = 1$. In this latter graph, different echoes appear at a same time.

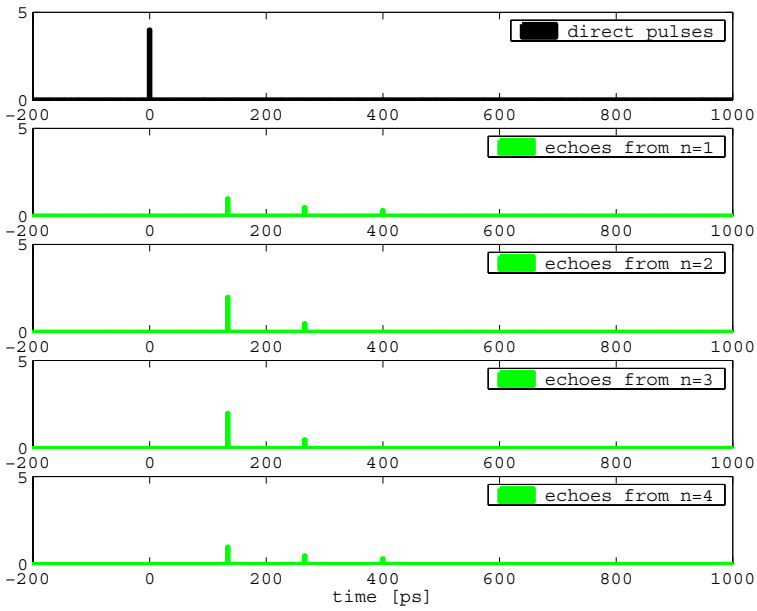

FIGURE 6.3. Delay time of the coupling echoes along the main lobe oriented at $\theta_0 = 0°$ for an array of $N = 4$ elements and spacing $d = 4cm$ and $G_0 = 1$.

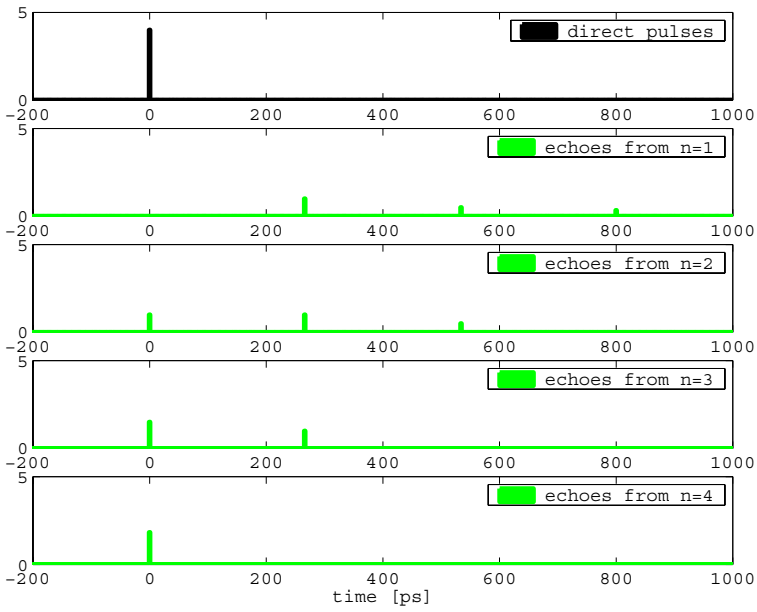

FIGURE 6.4. Delay time of the coupling echoes along the main lobe oriented at $\theta_0 = 90°$ for an array of $N = 4$ elements and spacing $d = 4cm$ and $G_0 = 1$.

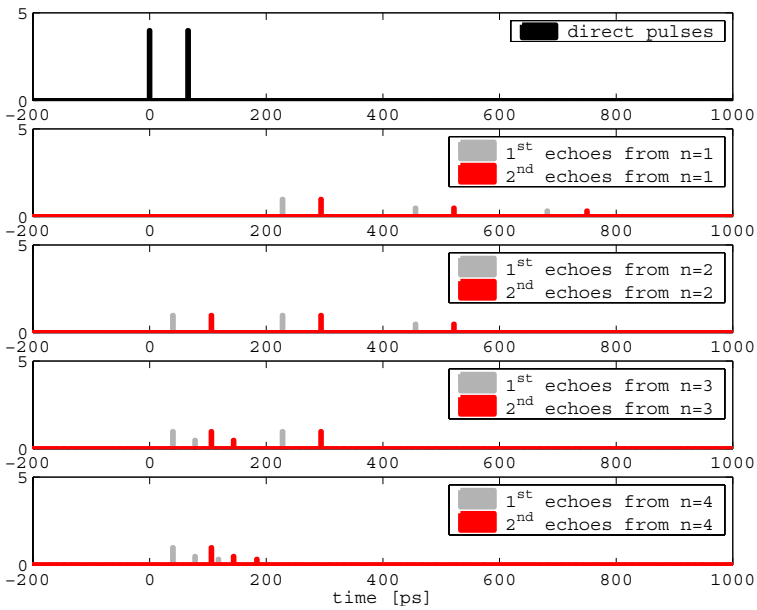

FIGURE 6.5. Delay time of the coupling echoes along the main lobe oriented at $\theta_0 = 45°$ for an array of $N = 4$ elements and spacing $d = 4cm$, $G_0 = 1$. The input signal is a train of $N_L = 2$ pulses with repetition rate $d/T_p = 2c$. It is clearly visible how the first echoes, e.g. those originated by $\ell = 1$ direct pulses are nearly superimposed to the $\ell = 2$ direct pulses. Observation angle at $\theta = 45°$.

contributions of a previous pulse ("cross-pulse coupling ") even for a scanning angle different from the endfire. In [23], spurious lobes (cross-pulse lobes) caused by "pulse interference" (in contrast with canonical sidelobes caused by "phase interference") are examined and the condition for their presence, $d/T_p >> c$, was retrieved. As in [23], sourcing signals with high pulse repetition rates or arrays with sparse configurations can potentially produce interferences between the ℓ'-th direct pulse and echoes originated from $(\ell < \ell')$-th direct pulses. For instance Fig.6.5, referring to $N_L = 2$ and $d/T_p = 2c$, shows how the echoes generated by the $\ell = 1$ pulses tend to be superimposed to the $\ell = 2$ direct pulses.

The condition on the pulse repetition rate which ensures the separation of the contributions of different pulses is

$$T_p > L_a/c(sin\theta_0 + 1) \tag{6.9}$$

where L_a is the array length. It can be seen again that the endfire scan is the most penalized one, since it requires the longest temporal separation, T_p, among pulses.

6.4.2 Coupling for finite-duration pulses

A more realistic even still qualitative analysis can be performed by taking into account, rather than a Dirac pulse, an input waveform $g(t)$ of finite duration T_0. It is expected that the coupling strength will be also dependent on T_0: if the pulse duration is longer than the time delay of the first echo, e.g. $T_0 > t_{e,1}$, direct pulses and echoes will be partially superimposed even at scan angles different from the endfire.

Additionally, to account for the limited bandwidth of real antennas, which sensibly affects the shape of the echoes and therefore the coupling mechanism, the time-domain effective height of the antenna is hereafter directly considered in the interference pattern of the array. The following simple mathematical model of the effective height, accounting for antenna distortion, is introduced in (6.5)

$$\boldsymbol{h}^t(\hat{\boldsymbol{r}}, \tau) = H_0(\theta)\delta^q(\tau)\hat{\boldsymbol{p}} \tag{6.10}$$

where $\delta^q(\tau)$ is the differential operator of q-th order, the factor H_0 is an angular-spreading factor and the only co-polar contribution to the radiated field $\hat{\boldsymbol{p}}$ is considered. For instance $q = 2$, $H_0 = -L^2 sin\theta/(2c)$ and $\hat{\boldsymbol{p}} = \hat{\boldsymbol{\theta}}$ yield the time dependence of a short dipole of length L as in [37]. According to this definition, and under the same hypothesis on mutual coupling of the previous section, the field radiated by the array of isotropic radiators ($H_0 = 1ms^{n-1}$) of order n is

$$rE^A(\boldsymbol{r}, \tau) = -\frac{\eta_0}{4\pi rc}\sum_{n=1}^{N}\sum_{l=1}^{N_L}\partial_\tau^q g(\tau + t_n - nt_s - lT_p) - \tag{6.11}$$
$$\sum_{n=1}^{N}\sum_{\substack{m=1\\ m\neq n}}^{N}\frac{G_0}{|n-m|}\sum_{l=1}^{N_L}\partial_\tau^q g(\tau + t_n - mt_s - lT_p - |n-m|\frac{d}{c})$$

It is now considered an array of radiators of ($q = 2$)-type excited by gaussian-pulse waveform $g(t) = \exp[-\frac{(t-\alpha)^2}{2\beta^2}]$, whose parameters α and β are set to control its practical duration $T_0 = ||tg(t)||_2/||g(t)||_2$, where $||\cdot||_2$ is a L_2 norm. Hereafter, the radiated fields will be observed on the $\phi = 0$ plane. Fig.6.6 and Fig.6.7 show the angle-time plot of the field radiated by an array of $N = 4$ elements, with and without coupling, which have been timed to produce endfire radiation. It is here assumed a coupling factor $G_0 = 0.15$ which corresponds to reasonable values $\Gamma_0 = -10dB$ and $S_0/d = -6dB$.

It can be noted the coherence point at $\theta = 90°$, and the four distinct contributions from the radiating elements at observation angles far from the boresight.

The effect of coupling between radiating elements is visible (see Fig.6.7) as oscillations in the late transient of the radiated field, even in the main body of the waveform, since $T_0 > t_{e,1}$ ($T_0 = 0.3ns$ and $t_{e,1} = 0$).

The variation of the coupling with the scanning angle can be evaluated introducing a square error indicator which quantifies the effect of inter-element coupling vs. the scanning angle and vs. the duration T_0 of the input signal. The last one is considered within a temporal range which includes the main part of the radiated signal.

$$a(\theta_0, T_0) = \frac{||\boldsymbol{E}_c^A(\theta = \theta_0, t, T_0) - \boldsymbol{E}_{nc}^A(\theta = \theta_0, t, T_0)||_2}{||\boldsymbol{E}_{nc}^A(\theta = \theta_0, t, T_0)||_2} \tag{6.12}$$

where the L_2 norm $||\cdot||_2$ is evaluated with respect to time for $t_0 - T_0/2 < t < t_0 + T_0/2$ and t_0 is such that $\boldsymbol{E}_c^A(\theta_0, t_0)$ is the peak value. Only the main part of the signals is therefore considered.

The dashed line in Fig.6.8 represents the relationship $T_0 = t_{e,1}$ e.g. $cT_0/d = (1 - |\sin\theta_0|)$, deduced from (6.8), which separates the overlapping and non-overlapping of the coupling echoes to direct pulses. In particular, for array density and duration of signals such that $cT_0/d < 1$, the $a(\theta_0, T_0)$ indicator increases along with the scanning angle since in this case $t_{e,1}$ reduces. Similarly, for scanning angles smaller than 30° the indicator increases either with the signal duration T_0 or with the reduction of the array spacing. In both the cases, an increasing value of signal duration, array density or scanning angle leads to coupling contributions with greater distortion of the main signal.

In the region $cT_0/d > 1$ and $\theta_0 > 30°$, the monotonic behavior of the indicator with respect to the scanning angle and signal duration is generally lost.

Finally, it can be observed that the mostly relevant distortion of the direct waveform is produced for large-duration input signals in broadside arrays ($\theta_0 = 0°$). Because of the symmetry imposed by this scanning angle with respect to the array geometry, the coupling echoes produced by symmetric radiators are fully synchronized (see again Fig.6.3) and therefore the strength of coupling echoes is reinforced.

For different scanning directions, instead, mutual coupling contributions produced from radiator pairs lose their temporal synchronization and spread over the whole duration of the direct signal, giving reduced distortion.

Mutual coupling always affects the signal in the endfire direction, quite apart from of the signal duration.

To compare the effect of coupling for two different durations of the driving signals, Fig.6.9 shows the field radiated by an array of N=4 isotropic radiating elements with main beam at $\theta_0 = 30°$. It can be observed that (Fig.6.9, bottom) for small values of $T_0/t_{e,1}$ (short-duration signals), the main part of the radiated signal is not sensibly distorted (Fig.6.9, bottom) since the echoes

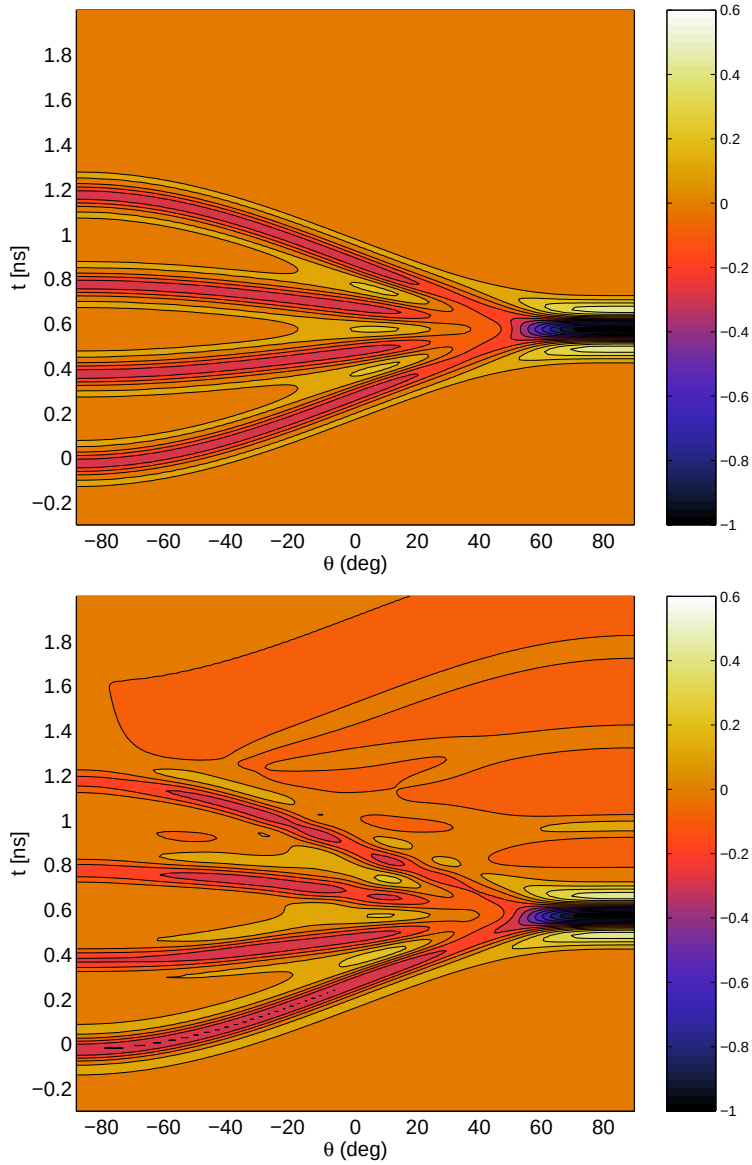

FIGURE 6.6. Transient field with coupling (bottom) and without coupling (up) for an array of four isotropic radiating elements with $n = 2$, $T_0 = 0.3ns$, $N = 4$, $d = 6cm$, $G_0 = 0.15$, $\phi = 0°$.

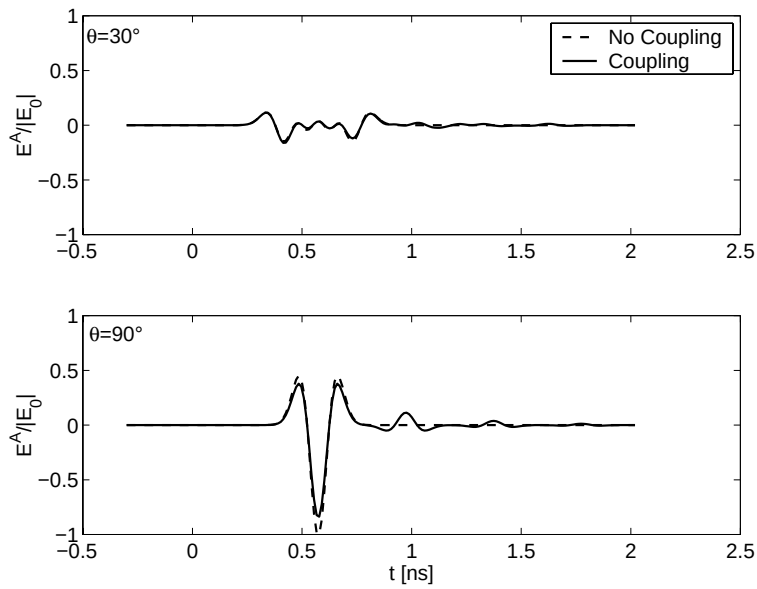

FIGURE 6.7. Array fields from Fig.6.6 at observation line $\theta = 30°$ (up) and $\theta = 90°$ (bottom), comparing the radiated dynamics with and without array coupling in the case of beam steering at $\theta_0 = 90°$.

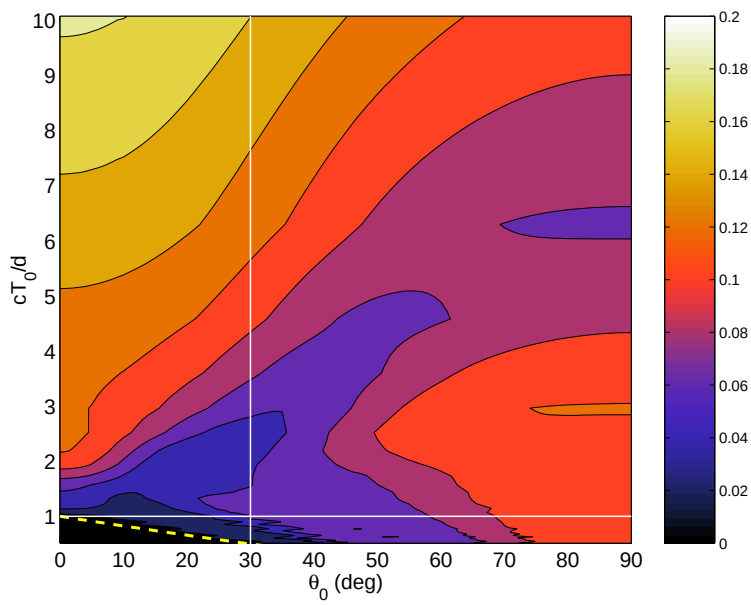

FIGURE 6.8. Variation of the indicator $a(\theta_0, T_0)$ v.s. the scanning angle and the pulse duration for an array of N=4 isotropic elements with second order ($n = 2$) differentiation as time dependence.

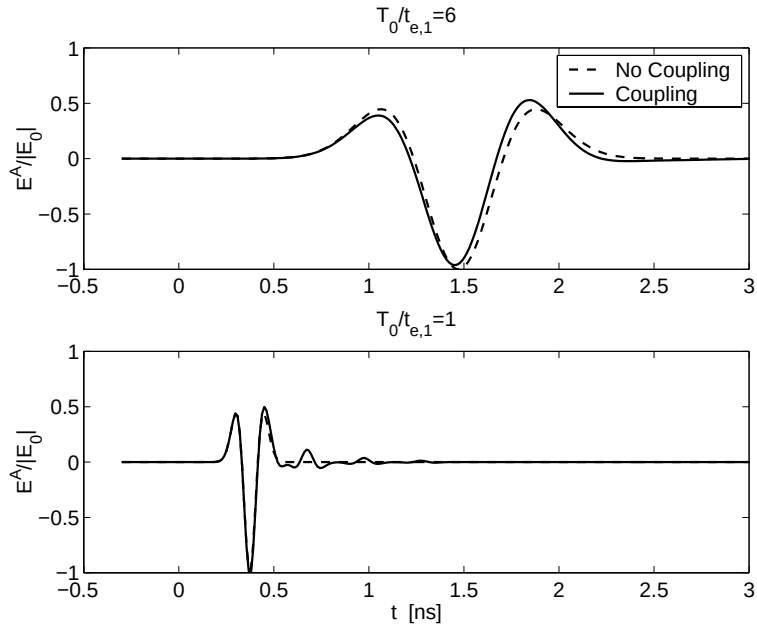

FIGURE 6.9. Radiated field along the main beam (at $\theta_0 = 30°$) for an $N = 4$ element array with and without the inclusion of the coupling effects, for two different durations T_0 of the gaussian pulse.

appear delayed with respect to the direct pulse. As $T_0/t_{e,1}$ increases the resulting signal is more distorted (Fig.6.9, up) since the echoes approach the main part of the direct signal.

If a larger array is considered, for instance having N=20 elements (Fig.6.10) a greater distortion is apparent in the main wavepacket of the radiated signal for long-duration pulses. Instead, only a longer ringing is produced in the late transient in the case of very short input pulses (Fig.6.10, bottom) since each oscillation belongs to different element echoes.

For real arrays, the antenna effective height and antenna-generator mismatch play an important role on the signal distortion due to coupling. The generator mismatch causes a distortion of the radiated signals, with a broadening of its duration. This effect is however taken into account in both the antenna effective height (which includes the antenna-generator mismatch) and in the expression of the active array factor through the embedded reflection operators $\gamma_{L,n}(\tau)$ applying to incoming current echoes. As a consequence, the signal distortion in the array will be relevant for narrow-band and unmatched antennas since the broad coupling echoes will be easily overlapped to the direct signal.

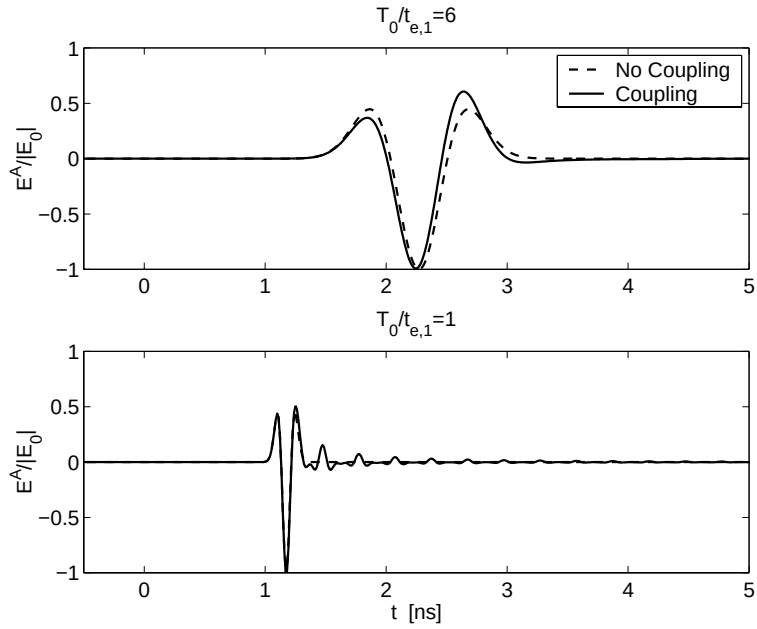

FIGURE 6.10. Radiated field along the main beam (at $\theta_0 = 30°$) for an array of $N = 20$ elements with and without the inclusion of the coupling effects, for two different gaussian pulse durations T_0.

6.5 A fullwave example

The coupling models introduced in previous sections are now employed to discuss the radiation from a realistic linear array of N=4 square bow-tie antennas of $4cm$ side and $6cm$-spaced (Fig.6.11). The antennas are fed in the gap by a voltage generator having 50Ω internal resistance and producing a gaussian pulse, $v_0(t)$, of duration T_0.

The structure has been modelled by the Finite-Difference Time-Domain method [39], [83]. The time-variant surface current density $\boldsymbol{J}(\rho, t) = \hat{n} \times \boldsymbol{H}_0(\rho, t)$, $\boldsymbol{H}_0$ being the time-dependent magnetic field evaluated on the array conductors, has been then used to calculate the radiated far field via the application of the Radon Transform [37].

$$\boldsymbol{r}\boldsymbol{E}^{\boldsymbol{A}}(\boldsymbol{r}, \tau) = -\frac{\mu}{4\pi}\frac{\partial}{\partial t}\int \boldsymbol{J}_{||}(\boldsymbol{\rho}, \tau + \frac{\hat{\boldsymbol{r}} \cdot \boldsymbol{\rho}}{c})dS \tag{6.13}$$

with $\boldsymbol{J}_{||} = \boldsymbol{J} - \hat{\boldsymbol{r}}(\hat{\boldsymbol{r}} \cdot \boldsymbol{J})$. Numerical results therefore account for all the coupling mechanisms among antennas. The field obtained is compared with that predicted as convolution between the time-domain coupling-free array factor and the TD effective height of the isolated bow-tie (Fig.6.12). Additionally, it

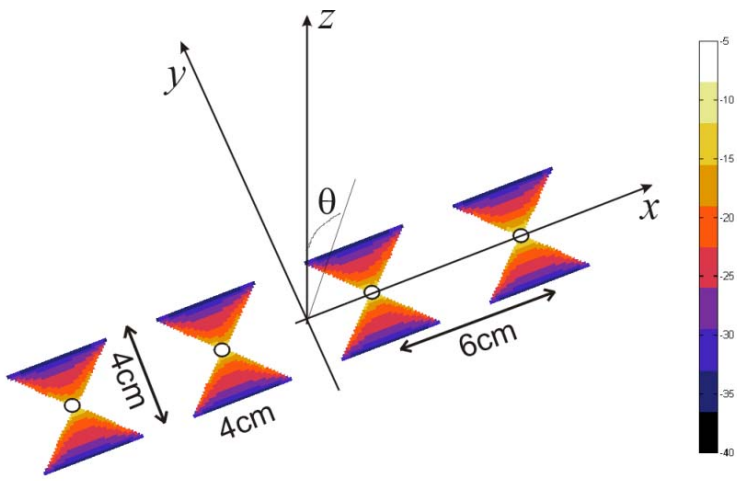

FIGURE 6.11. Linear array of four-elements bow-ties. Antennas are sourced in the gap. The shadowed pattern is the energy norm of the induced currents used for the Radon transform.

is also shown the transient field obtained as $\mathcal{F}_A * \boldsymbol{h}^t * v_0(t)$ where the simplified expression of the active array factor in (6.6) and the fullwave computed effective height in Fig.6.12 are used. More in detail, having observed that the average reflection coefficient of the standalone bow-tie in the 2-10 GHz band is -8 dB and that the average coupling factor among contiguous elements is of the order of -8.5 dB, the global factor $G_0 = S_0\Gamma_0/d$ in (6.6) has been set to $G_0 = 0.15$. Accordingly, Fig.6.13 shows the space-time patterns, obtained by the different models, when the input signal $v_0(t)$ has a duration $T_0 = 0.3ns$ and the array is timed to produce end-fire radiation.

It can be possible to observe that the effect of the time-domain coupling appears, in both the fullwave model (Fig.6.13,b) and in the simplified one (Fig.6.13,c), as a broadening of the third oscillation in the endfire direction and as additional oscillations along side lobes for $\theta < 0$.

Cuts in Fig.6.14 of the transient fields in Fig.6.13 at $\theta = 30°$ show a good agreement between the fullwave results and the simplified models, in particular for what concerns the 20% reduction of the signal peak due to interference of coupling echoes . Finally, Fig.6.15 shows the radiated field when the array is focused at $\theta_0 = 30°$. For this case the input signal $v_0(t)$ has short duration compared with the time delay of first echo ($T_0/t_{e1} = 1$) and, as expected from the qualitative analysis in the previous Section, the distortion is nearly negligible since the echoes begin to overlap the direct signal after the third oscillation.

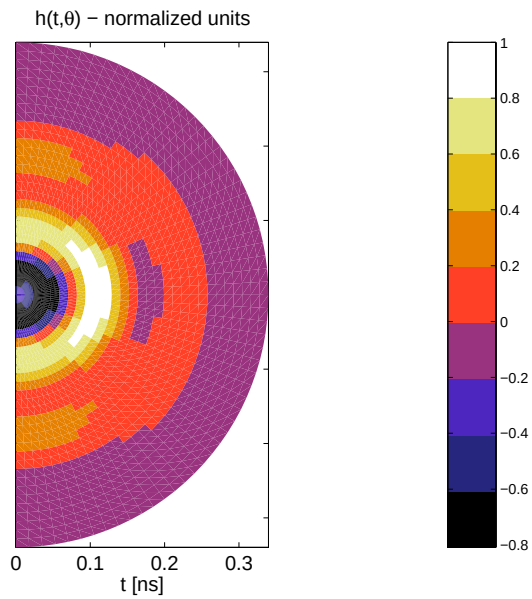

FIGURE 6.12. Fullwave-computed time-domain effective height in (t-θ) plane for the standalone bow-tie .

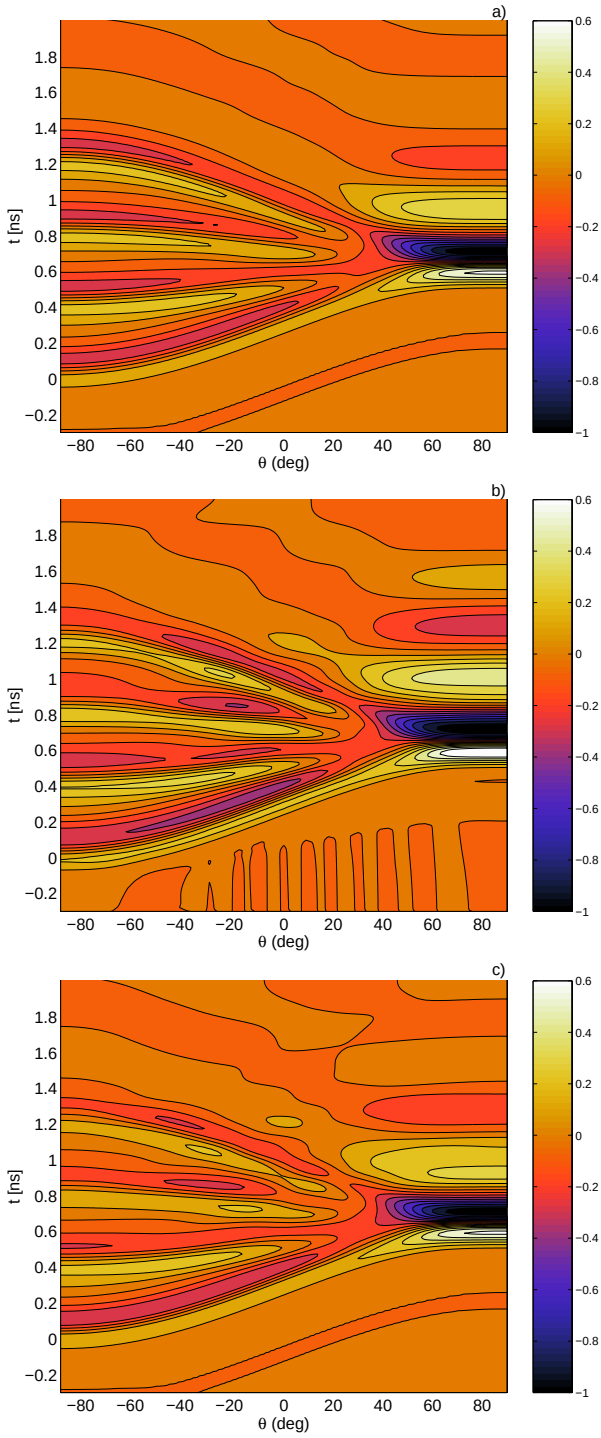

FIGURE 6.13. Bow-tie array sourced by $T_0 = 0.3ns$ gaussian pulses timed to produce endfire focusing: a) array field neglecting coupling; b) fullwave array field including coupling; c) approximated array field with coupling computed by the active array factor in (6) with $G_0 = 0.15$.

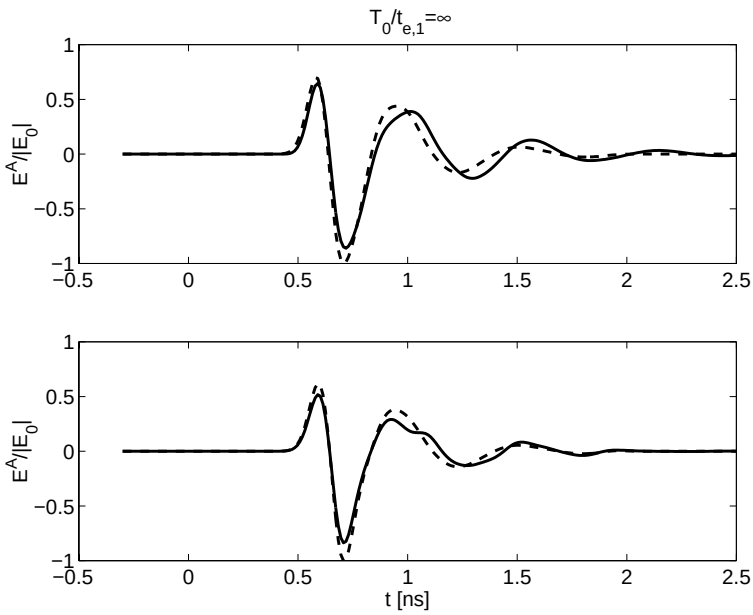

FIGURE 6.14. Cuts of the transient field in Fig.6.13 at $\theta = 90°$, comparing the array response with (continuous lines) and without coupling (dashed lines) for the fullwave simulation (up) and for the simplified model (down).

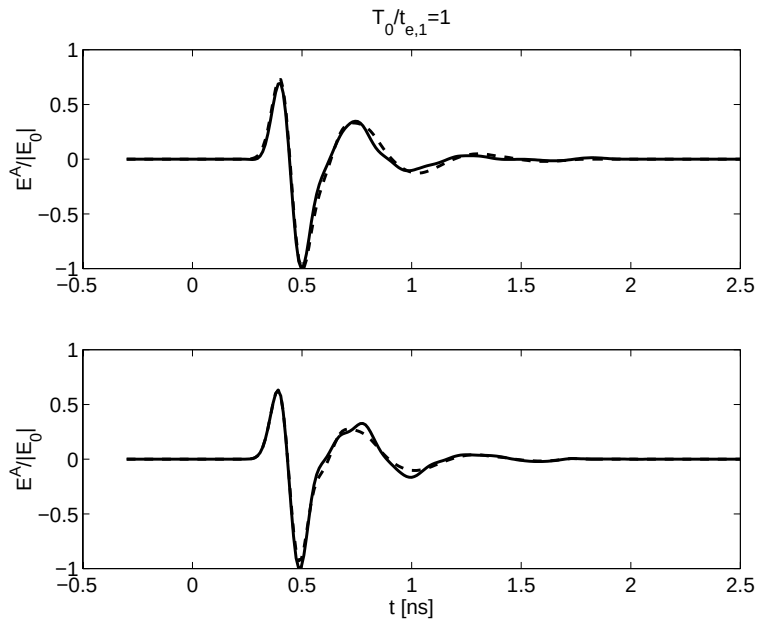

FIGURE 6.15. Radiated field for an $N = 4$ bow-tie array along the main beam at $\theta_0 = 30°$ with (continuous line) and without (dashed lines) the inclusion of the coupling effects, for the fullwave simulation (up) and for the model (down) .

Chapter 7

Synthesis of Pulsed Arrays

7.1 Introduction

Typical applications of pulsed arrays in literature adopt very simple excitation signals: Gaussian, modulated Gaussian or Hermite-Rodriguez pulses are weighted in amplitude either uniformly or with constant coefficients [27] and properly delayed to have a frequency-independent beam steering. Such an excitation synthesis closely resembles the one adopted in conventional narrowband applications (with phase shifters instead of delay lines), where each radiating element is excited by a quasi-monochromatic long pulse weighted by a complex coefficient in order to control some radiation parameters (SLL, gain, beamwidth, beam shape, scan angle, nulls...) in the angular domain and for a small set of frequencies. Nevertheless actual and future pulsed arrays applications can exploit not only the angular domain, but also the temporal domain in order to shape, discriminate or multiply the transmitted or radiated pulses required by the application. Thus, pulsed radiation phenomenology differs from the conventional narrow-band one, since the temporal domain, replacing the frequency domain, adds a new degree of freedom to array excitation design: the input signals' waveform. In [28] and [29] two methods have been proposed to compute transient input waveforms in order to optimize array performances. The techniques consist of: i) specification of the bandwidth of the input signal; ii) retrieval of array impedance matrix using Pocklington's integral equation and a moment method; iii) proper expansion of the far zone electric field, using the array impedance matrix; iv) definition of a variational expression to find the FD voltages that satisy the desired array performances. The methods were applied to linear arrays of dipoles, considered the array mutual couplings and optimized performances like the amplitude of the transient radiated field at a specified time and angular position [28], or the transmitted energy in a specified time interval [29], eventually with sidelobe constraints. Microwave-imaging Space-time beamforming (MIST) has been recently proposed in breast

cancer early detection; the first UWB radar techniques in medicine sought to identify the presence and location of significant scatterers in the breast by means of an array with proper time shifting among antenna elements in order to align the returns from a hypothesized scatterer at a candidate location. This technique has been improved by passing the time-aligned signals through a bank of finite-impulse response filters, one in each antenna channel. The weights in the filters are designed using a least squares technique so the components of the backscattered signal originating from the candidate location are compensated for frequency-dependent propagation effects, artifacts and noise [84].
In both cases, the existing techniques can't be applied to perform a synthesis of an array with complex radiating performances (like a shaped beam).
A different synthesis technique is here proposed which computes the amplitude, the transient behavior and the relative delay of the input signals of the array in order to shape the radiated field in accordance to a given mask in the angular and temporal domains. As in the frequency domain [34], the array synthesis problem can be initially approached as an inversion problem. Once the desired far field of the array has been decided (a mask of the radiation pattern), the radiation equation, which relates the input currents to the radiated field, can be inverted in order to retrieve the array excitations. The radiation equation is the Fourier Transform of Eq.4.3 in the monochromatic case and the Radon Transform of Eq.4.1 and Eq.4.2 in the UWB case. In both cases, the relative inverse tranforms can be efficiently applied to solve the synthesis process. Since the retrieved excitations probably will be hardly realizable, they can be then mapped onto a set of physical excitations in order to satisfy beamforming constraints. This topic will be deeply addressed in the next sections.
This first idea of synthesis can be improved by means of successive iterations of the inversion technique, extending to TD the formulation of Alternating Projections presented in [85] for monochromatic arrays: it consists of iterative projections of the radiated pattern onto the desired pattern mask and of the obtained excitations onto a physical set of excitations. It can be proved that the synthesis problem is hence reduced to the problem of finding the intersection of sets, in particular, as it will be later explained in details, among the set of all far fields which can be radiated by the given array using realizable excitation currents and the set of all the functions which fulfil a given mask requirement. After the formulation of the technique, some numerical examples are presented in order to check the performances of the method when applied to possible pulsed arrays applications.

7.2 Definition of the TD synthesis problem

Given a linear array of N elements at positions x_n sourced by a set of currents $\{i_n(\tau)\}_{n=1..N}$, the time-domain array factor can be expressed as in Eq.4.2.

$$\mathcal{AF}(\theta,\tau) = \sum_{n=1}^{N} i_n^+(\tau + t_n(\hat{\boldsymbol{r}})) \tag{7.1}$$

where the mutual couplings among radiating elements in the array are neglected, as in pulsed arrays they can be constrained to very low values as stated in the previous chapter and in [26]. It is also supposed that all the radiating elements of the array have the same radiation pattern, hence the total radiated field of the array is the convolution between the array factor and the element factor.

Equation 7.1 is the discrete version of the Radon Transform

$$\mathcal{R}\{i^+(x,\tau)\}(\theta,\tau) = \int i^+(x,\tau + t(x,\theta))dx \tag{7.2}$$

sampled at positions $x_n = nd$, where d is the inter-element distance. The time derivative of the previous expression is proportional to the field radiated by a continuous line source $i^+(x,t)$ deployed along the $x-$axis.

The synthesis problem can be defined as the problem of retrieving the excitation currents $\{i_n^+(\tau)\}_{n=1..N}$ once the array elements, array geometry and desired radiation pattern have been fixed. In our case the synthesis problem includes also a constraint on the shape of the currents to be retrieved. In the following, the co-polar component of the desired radiation pattern is defined in the time-angular domain in terms of an upper and a lower mask $M_{U,E}(\theta,\tau)$ and $M_{L,E}(\theta,\tau)$ (see Fig.7.1). The desired radiation pattern is related to the desired array factor by the deconvolution operation

$$\mathcal{AF}(\theta,\tau) = \boldsymbol{h}^T(\theta,\cdot) \otimes \boldsymbol{E}(\theta,\cdot)(\tau) \tag{7.3}$$

The desired array factor masks $M_{U,AF}(\theta,\tau)$ and $M_{L,AF}(\theta,\tau)$ are then retrieved by Eq.7.3 and the synthesis technique will work on the desired array factor. The array factor and radiated pattern associated to the retrieved currents are called the *realized pattern* and *realized array factor*. The co-polar component of the realized radiation pattern should be included within the two masks $M_U(\theta,\tau)$ and $M_L(\theta,\tau)$, while the realized array factor should be included within the two masks $M_{U,AF}(\theta,\tau)$ and $M_{L,AF}(\theta,\tau)$. Since the cross-polar component is neglected in the synthesis process (as in the monochromatic case), in the rest of the chapter the term radiated field will address the only its co-polar component.

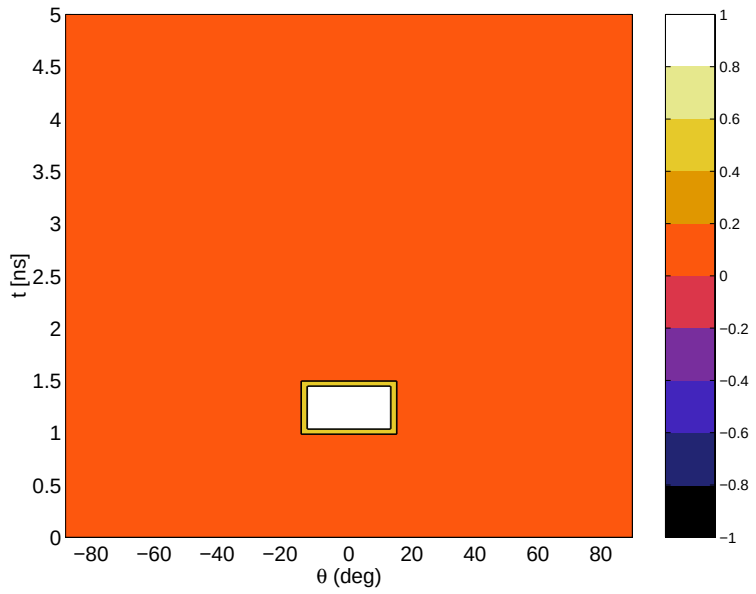

FIGURE 7.1. Example of the desired radiation pattern

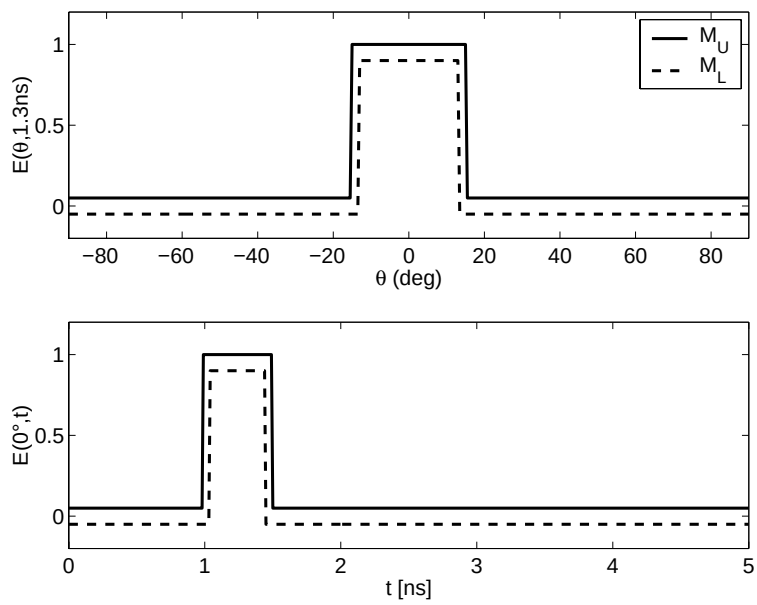

FIGURE 7.2. Example of cuts of the desired radiation pattern

Fig.7.1 and Fig.7.2 show an example of pulse-like desired radiated field, in which the field should be mostly included between 1ns and 1.5ns in time and -15 and +15 degrees in angle, with oscillations below 5% of its peak outside the pulse region and 50ps of slope front.

7.3 Intersection finding problem

This section closely follows [85] in order to extend the method of Alternating Projections to time-domain arrays. Let $\mathcal{B}$ be the set of all the array factors which can be radiated by the considered array (with fixed geometry and radiating element).

$$\mathcal{B} = \left\{ AF(\theta,\tau) : AF(\theta,\tau) = \sum_{n=1}^{N} i_n^+(\tau + t_n(\theta))] \right\} \tag{7.4}$$

All the array factors in this set can be only generated from Eq.4.2. If constraints are put on the excitations, for example in order to make the currents feasable, they define a subset of $\mathcal{B}$, i.e. $\mathcal{B}_C$, to which the realized array factor must belong. For example, in order to have a simple beamforming network, we can impose that the excitations must be a linear combination of derivated gaussian waveforms. Once the desired radiation pattern (the mask) is established, another set of functions can be defined

$$\mathcal{M} = \{G(\theta,\tau) : M_{L,AF}(\theta,\tau) \leq G(\theta,\tau) \leq M_{U,AF}(\theta,\tau)\} \tag{7.5}$$

which includes all the time-angular functions which fulfill the mask constraints. The solution to the synthesis problem is an array factor which belongs to the intersection

$$\mathcal{B}_C \bigcap \mathcal{M} \tag{7.6}$$

The time domain synthesis problem is hence formulated in a very general way.

7.4 Alternating projections

The most effective method of solution of the intersection problem is based on the concept of projection operator. The projector P_A over the closed subset $\mathcal{A}$ of a normed space $\mathcal{H}$ is the operator defined by

$$P_A : x \in \mathcal{H} \rightarrow y_0 \in \mathcal{A} : \|x - y_0\| \leq \|x - y\|, \forall y \in \mathcal{A} \tag{7.7}$$

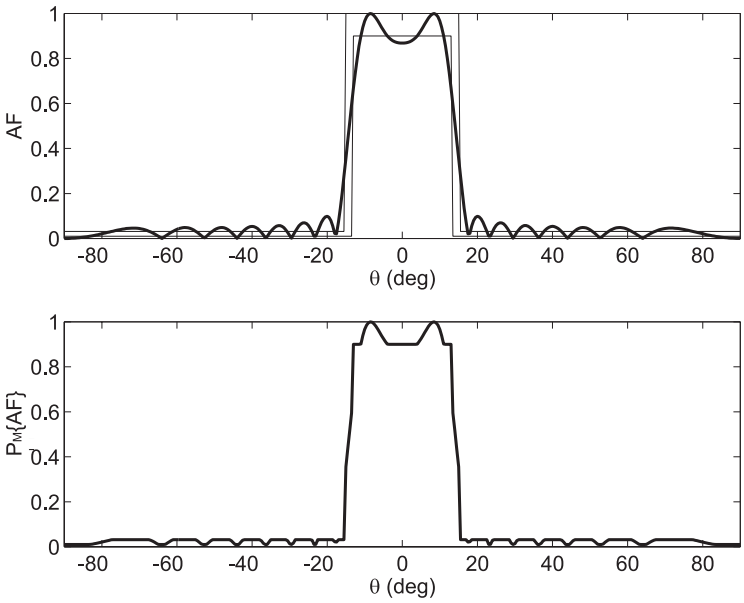

FIGURE 7.3. Example of projection operation $P_{\mathcal{M}}$ top) initial array factor and desired mask; bottom) projected function

The point y_0, which is the point of $\mathcal{A}$ nearest to x, is called the projection of x over $\mathcal{A}$.

Hence it is needed to define two projection operators, $P_{\mathcal{B}_C}$ and $P_{\mathcal{M}}$ over $\mathcal{M}$ and $\mathcal{B}_{\mathcal{C}}$, to respectively project a function in the set of realizable array factors $\mathcal{B}_{\mathcal{C}}$ and an array factor in the set of the masks $\mathcal{M}$. In particular,

$$P_{\mathcal{B}_C} = \mathcal{R} F_C \mathcal{R}^{-1} \tag{7.8}$$

where $\mathcal{R}$ and $\mathcal{R}^{-1}$ represent the Radon transform and inverse Radon Transform respectively; F_C represents a mapping of the excitations onto the set of physical excitations. Both the inverse Radon Transform and the excitation mapping will be described later. The second projection operator $P_{\mathcal{M}}$ is instead defined as

$$P_{\mathcal{M}}\{AF(\theta,\tau)\} = \begin{cases} M_{U,AF}(\theta,\tau) & |AF(\theta,\tau)| > M_{U,AF}(\theta,\tau) \\ AF(\theta,\tau) & M_{L,AF}(\theta,\tau) < |AF(\theta,\tau)| < M_{U,AF}(\theta,\tau) \\ M_{L,AF}(\theta,\tau) & |AF(\theta,\tau)| < M_{L,AF}(\theta,\tau) \end{cases} \tag{7.9}$$

Fig.7.3 shows an example of application of the projection operation $P_{\mathcal{M}}$ to an array factor: the initial array factor and the desired mask are shown at the top of the figure, while at the bottom the projected function is presented.

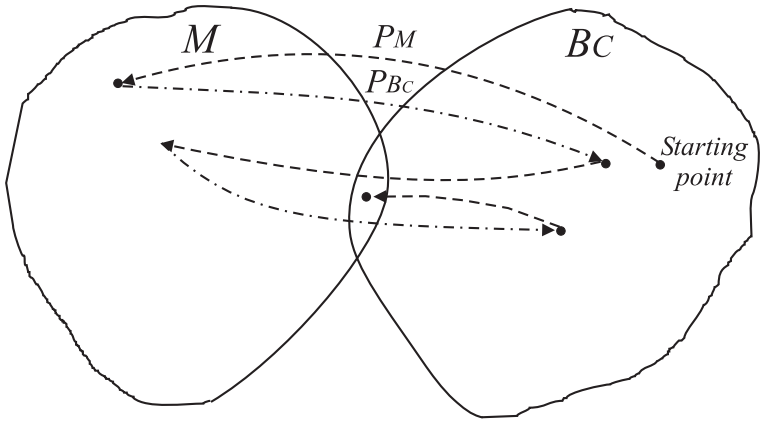

FIGURE 7.4. Alternating projections applied between the sets $\mathcal{M}$ and $\mathcal{B}_C$

Starting from an initial array factor (or equivalently a set of array excitations), the iteration of the two projection operations permits to progressively approach the optimum excitation solution, as shown in Fig.7.4. Hence the name of the method, alternating projections or successive projections.

A flowchart of the proposed synthesis method is shown in Fig.7.5. After the definition of the input parameters, as the array factor masks and the starting array factor, the method consists in successive projections $P_{\mathcal{M}}$ and $P_{\mathcal{B}_C}$ of the array factor. After each iteration it can be checked if the maximum number of iteration has been reached or if the retrieved array factor satisfies the mask requirements.

The first iteration uses as the initial array factor the upper user-defined mask: hence the first step of the synthesis algorithm performs a simple Radon inversion of the desired mask with a proper mapping of the excitations.

This method can be simply extended to planar and non planar arrays.

The inverse Radon Transform and the Hermite Rodriguez (HR) mapping of the excitations will be described in the next two sections.

7.5 Radon inversion

As already stated when the Radon Transform has been introduced, the Radon Transform satisfies the Projection Slice Theorem [19], which relates the Fourier Transform of a projection with a slice of the two-dimensional Fourier Transform of the line source current or of the array input currents. The theory in [33] can be applied to the array case as follows

$$\mathcal{F}_{x\to\theta} \circ \mathcal{F}_{t\to\omega} \circ i_n^+(x,t) = \mathcal{F}_{t\to\omega} \circ [\mathcal{R} \circ i_n^+(x,t)] \tag{7.10}$$

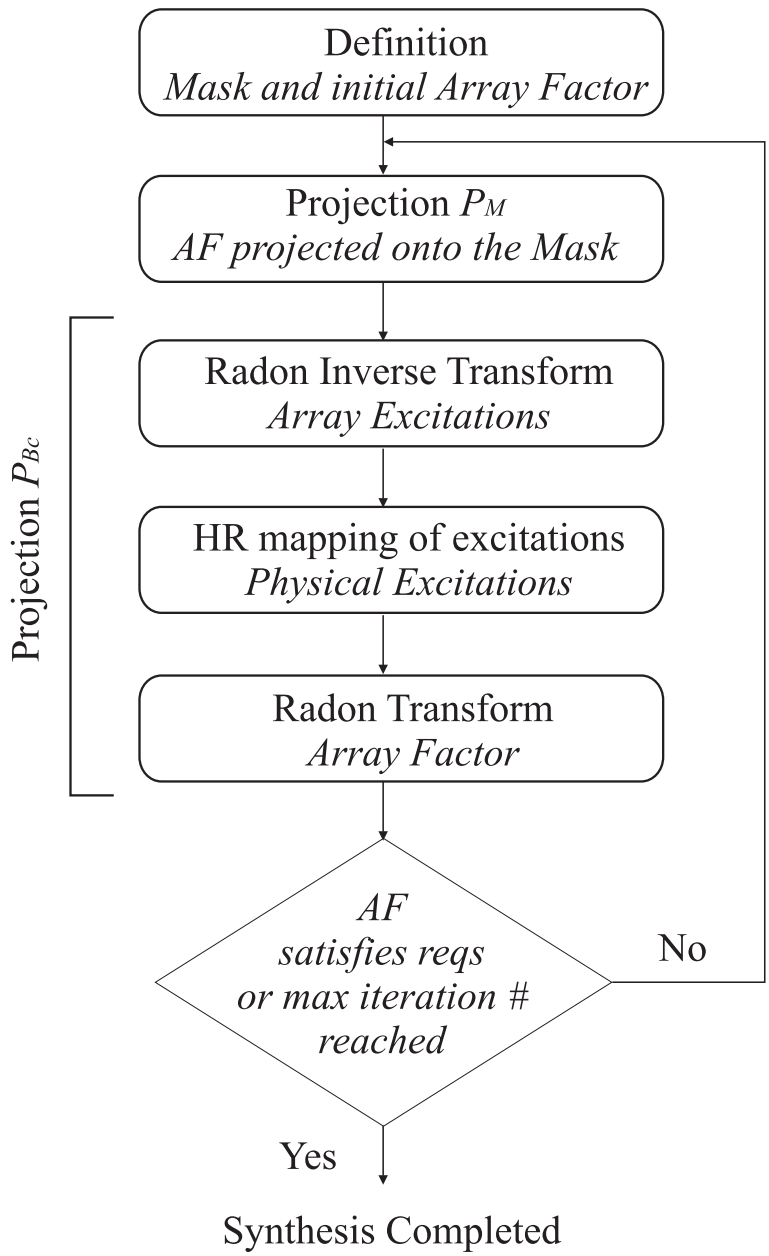

FIGURE 7.5. Flow chart of the presented synthesis method

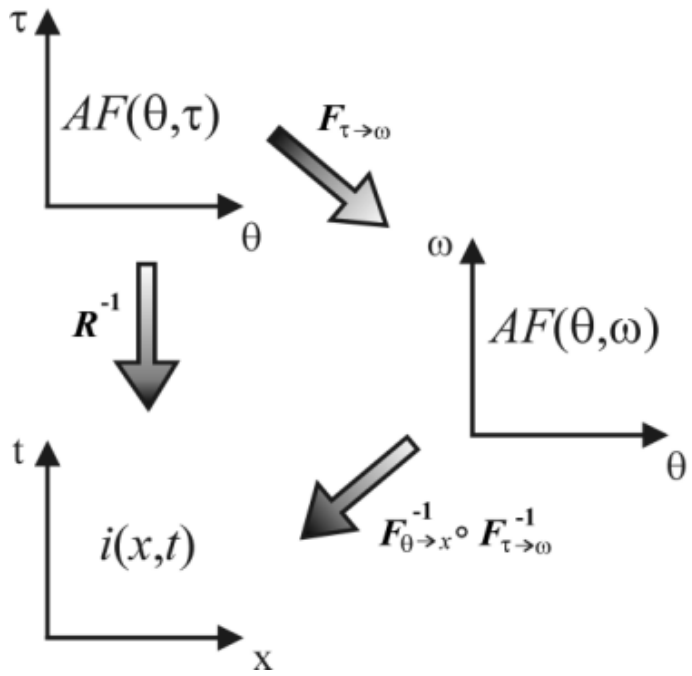

FIGURE 7.6. Relation between currents domain and array factors domain by Radon and Fourier Transforms

where $\mathcal{F}_{a\to b}$ represents the discrete Fourier Transform from a-domain to b-domain, whereas $\mathcal{R}$ represents the discrete Radon Transform of the current. The term between square brackets represents the array factor.

The Projecton Slice Theorem can be used in the array synthesis process, in order to retrieve the excitation currents from the projected array factor $P_{\mathcal{M}}\{AF(\theta,\tau)\}$, requiring a sequence of Direct and Inverse Discrete Fourier Transforms.

$$i_n^+(x,t) = [\mathcal{F}^{-1}_{\omega\to t} \circ \mathcal{F}^{-1}_{\theta\to x} \circ \mathcal{F}_{t\to\omega} \circ (P_{\mathcal{M}}\{AF(\theta,\tau)\})](t) \tag{7.11}$$

Fig.7.6 gives a pictorial view of Eq.7.10 in the case of absence of the projection $P_{\mathcal{M}}$, in order to better understand the inversion method. This formulation permits to simply invert the Radon Transform.

7.6 Excitation Mapping

The excitation mapping consists in a suitable representation of the synthetized signals $i_n^+(\tau)$ in order to obtain physically realizable waveforms. For each it-

eration of the synthesis process, the obtained excitations have to be projected onto this set. Input signals to UWB systems are often expressed as superposition of derivated gaussian signals using Hermite Rodriguez functions [2], [16]. The synthetized currents at each iteration of the proposed synthesis process can thus be represented by a small set of coefficients of a HR representation [14]

$$\alpha_{\lambda_n,k} =< i_n^+(\tau), w_{\lambda_n,k}(\tau) >= \frac{1}{\sqrt{2^k k!}} \int_{-\infty}^{+\infty} i_n^+(\tau) H_k(\tau/\lambda_n) d\tau \tag{7.12}$$

where $\{w_{\lambda_n,k}(t)\}_{k=0..\infty}$ is the set of basis functions (Hermite Rodriguez functions), $\{\alpha_{\lambda_n,k}\}_{n=1..\infty}$ is the set of coefficients of the representations, λ_n is a scale parameter and $H_k(\tau)$ is the Hermite polynomial of order k.

The proposed signal representation

$$i_n^+(\tau) = \sum_{k=0}^{K} \alpha_{\lambda_n,k} w_{\lambda_n,k}(\tau - \tau_{0,n}) \tag{7.13}$$

is sensible to the scale parameter λ_n, to the temporal shifting of the basis functions $\tau_{0,n}$, to the temporal behavior of the input functions and to the representation order K. Some suggestions for the choice of these parameters are here provided in order to speed up the convergence of the representation.

As suggested in [14], the scale parameter can be roughly fixed to 30% of the signal support, defined as the practical duration of the input currents [37].

$$T_n = \frac{||\tau i_n^+(\tau)||}{||i_n^+(\tau)||} \tag{7.14}$$

Usually all the computed currents have roughly the same practical duration, since they share the same bandwidth (defined from the desired radiated far field). If the λ_n related to the most energetic radiating element is chosen as the common λ, a single scale parameter can be used for the whole array, implying a single pulse generator for the whole system.

The Hermite Rodriguez functions are defined symmetrically with respect to the temporal origin, thus each basis function has to be shifted in time by $\tau_{0,n}$

$$\tau_{0,n} = \frac{\int \tau |i_n^+(\tau)| d\tau}{\int |i_n^+(\tau)| d\tau} \tag{7.15}$$

which is the expected value [38] of the variable τ with a probability density function $|i_n^+(\tau)|$. This temporal shift permits a faster convergence of the representation with respect to other shifts, as for example the position of the

TABLE 7.1. Parameters of the representation

Parameter	Value
λ_n	$0.3T_n$
$\tau_{0,n}$	barycentre $(i_n^+(\tau))$
Filter	$0.1max_n(i_n^+(\tau))$
K	10-15

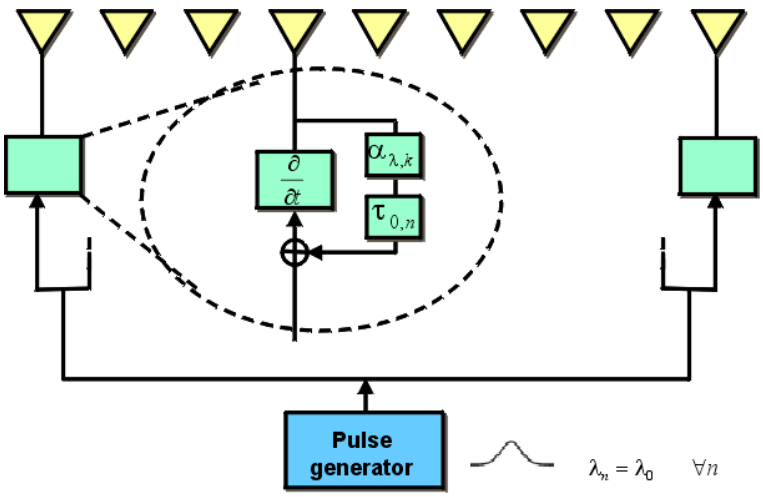

FIGURE 7.7. Beamforming network

geometric mean. It can be interpreted as the position of the barycentre of the current.

If the input currents exhibit rapid variations, the representation in Eq.7.13 has a slow convergence and a large number of terms K are required in the sum. A proper low-pass filtering of the input currents can speed up convergence: for example, in the proposed method, the oscillations with amplitude lower than 10% of the peak amplitude have been filtered out. In this way the main information content of the signal is preserved and the convergence of the representation has been further improved.

If the presented parameters are set to the suggested values (resumed in Tab. 7.1), the order K of the representation can be fixed to about 10-15 terms.

Using this representation, the beamforming network is simplified, since it can use a Gaussian pulse generator and a set of differentiators and modules which permit the control of amplitude and delay of signals, as shown in Fig.7.7.

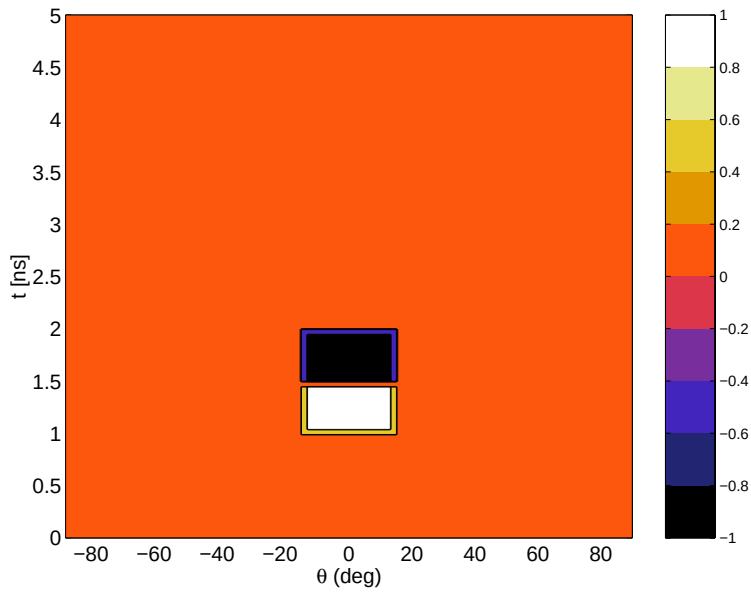

FIGURE 7.8. Time domain desired radiated field of Example 1.

7.7 Numerical Examples

In the following sections the synthesis of desired radiated fields is addressed in some numerical examples using the proposed method. In each example, the considered linear array includes $N = 20$ equispaced radiating elements with interelement distance $d = 5cm$.

7.7.1 Single monocycle pulse

The first objective radiated field is shown in Fig.7.8, consisting of two consecutive pulses of opposite sign, defined in the interval $|\theta| < 15°$ and $1ns < t < 2ns$. The effective height of the single radiating element was supposed to be a single differentiation $h^T(\hat{\boldsymbol{r}}, \tau) = \delta'(\tau)$ and Eq.7.11 was used to retrieve the necessary transient currents.

The proposed synthesis method has been applied using the HR input current representation with $K = 9$.

Fig.7.9 and Fig.7.10 show the realized pattern and currents after the very first iteration of the synthesis process, showing a large disagreement with the desired radiation pattern and with the final realized pattern after 20 iterations (see Fig.7.11), which is in good agreement with the masks of Fig.7.8. Also the currents obtained from the first iteration present a complex transient behavior which vanishes applying the alternating projections.

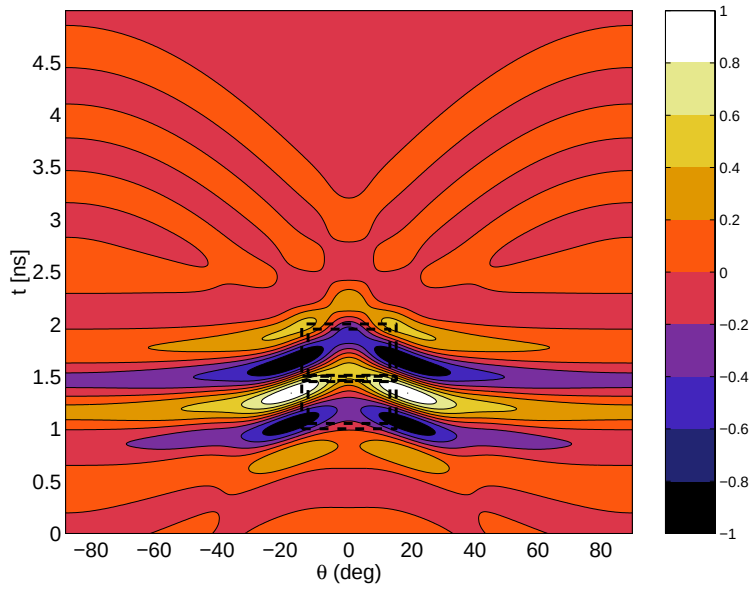

FIGURE 7.9. Realized radiation pattern after the 1st iteration of Example 1.

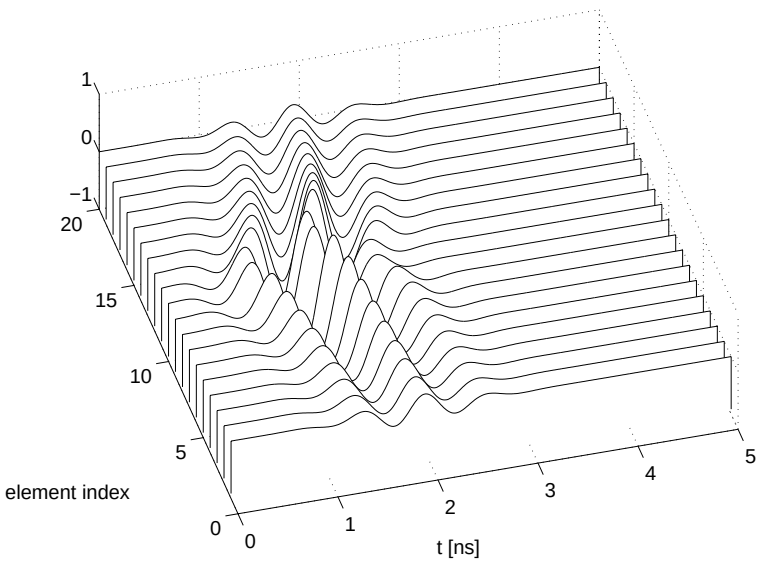

FIGURE 7.10. Realized currents after the 1st iteration of Example 1.

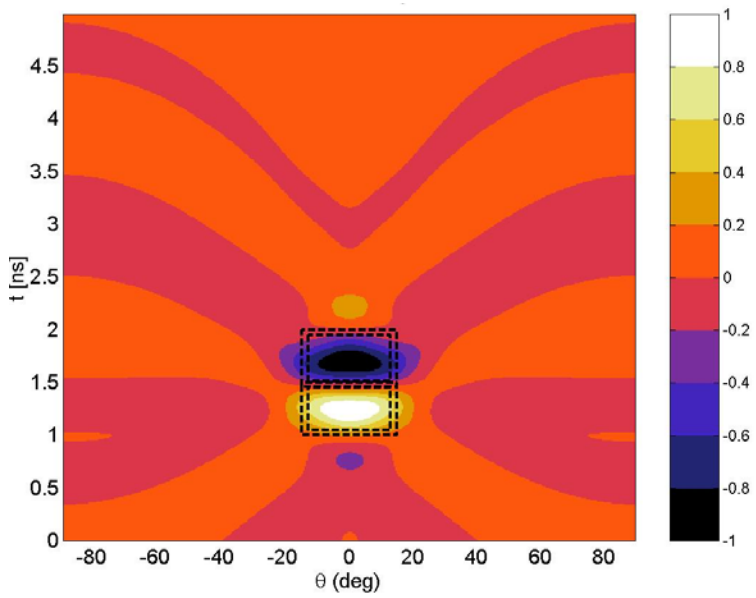

FIGURE 7.11. Realized time domain radiated field of Example 1.

The coefficients used in the final excitation projection and the final synthetized currents are shown in Fig.7.12 and Fig.7.13 respectively.

Because of the odd symmetry of the radiated field with respect to time and of the differentiating effect of the radiating elements, the desired array factor (and the related excitation currents) presents an even symmetry, and hence mostly the 2nd and 4th order of the coefficients contribute to the representation of the excitations. Although the simple shape in time and angle of the desired far field mask, the realized input currents are not very similar to each other in their transient shape. It can also be noted from Fig.7.13 a progressive tapering in the amplitudes of the input currents, from the centre of the array to its borders, which is typical in monochromatic arrays when reducing side lobe levels.

Tilted single monocycle pulse

The method was tested using the same objective radiated field tilted to an angle of 30 degrees. The results in terms of realized pattern and currents are shown in Fig.7.14 and Fig.7.15.

As for the non-tilted case, the realized far field is in good agreement with the mask. As expected, the realized currents present a progressive time shift with respect to each radiating element position, in order to have the pattern tilted to the desired angular position.

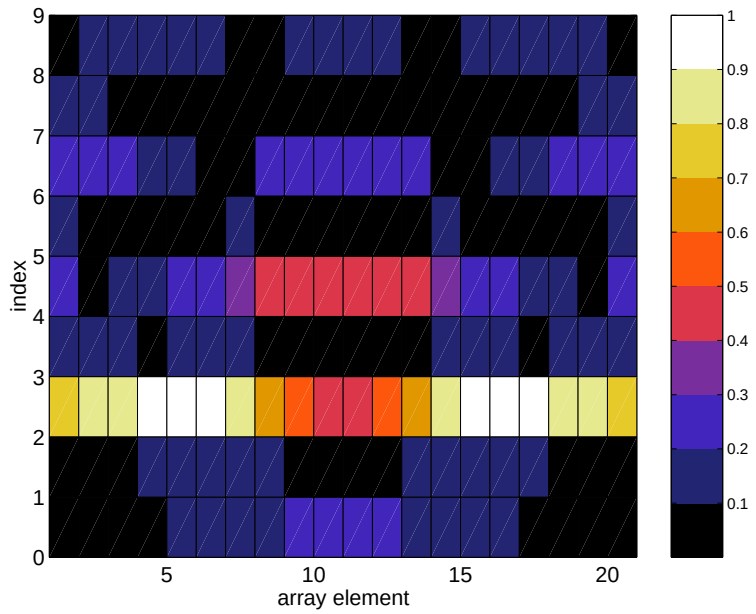

FIGURE 7.12. Set of Coefficients used for the synthesis process of Example 1.

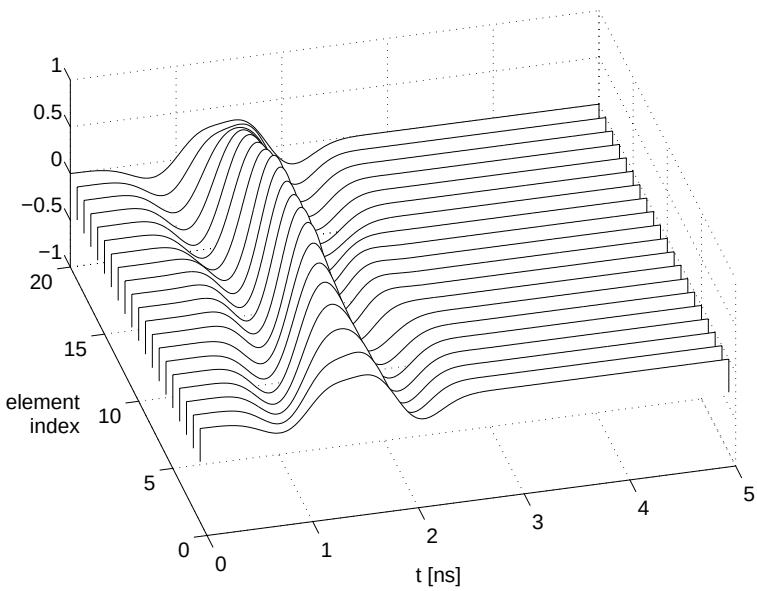

FIGURE 7.13. Realized TD input currents of Example 1.

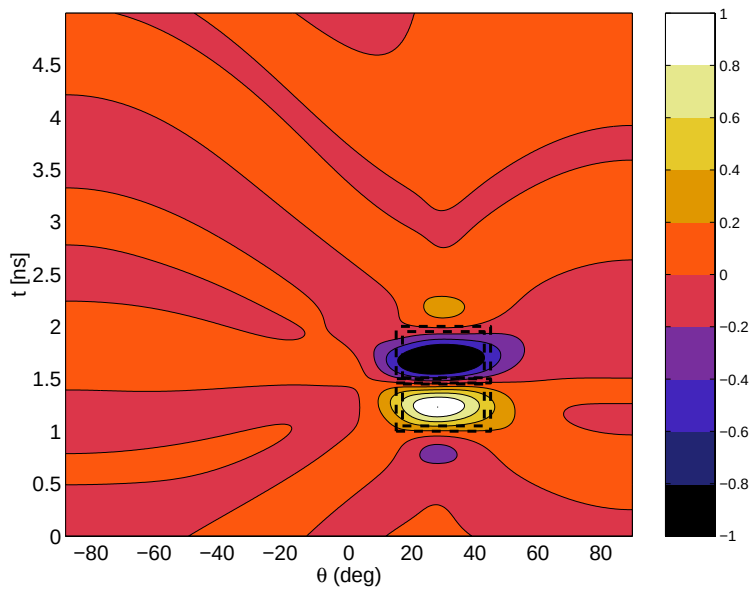

FIGURE 7.14. Realized radiation field for the mask of Example 1 tilted to an angle of 30 degrees.

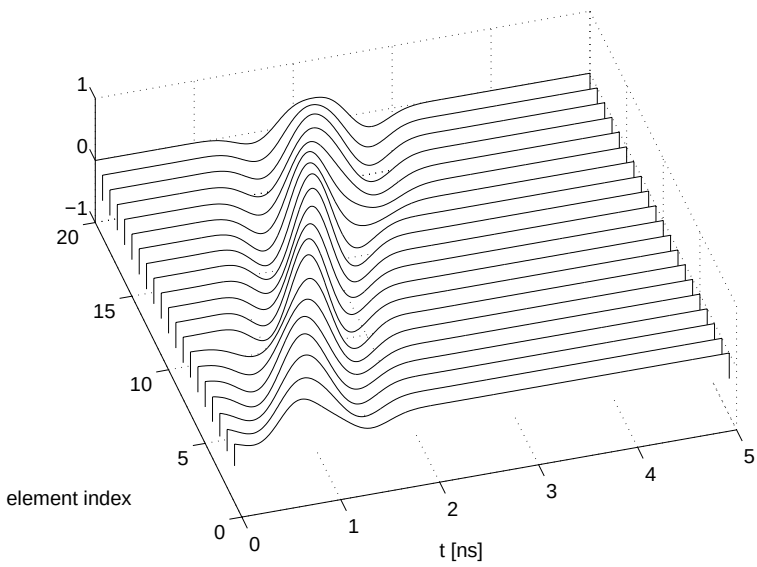

FIGURE 7.15. Realized currents for the mask of Example 1 tilted to an angle of 30 degrees.

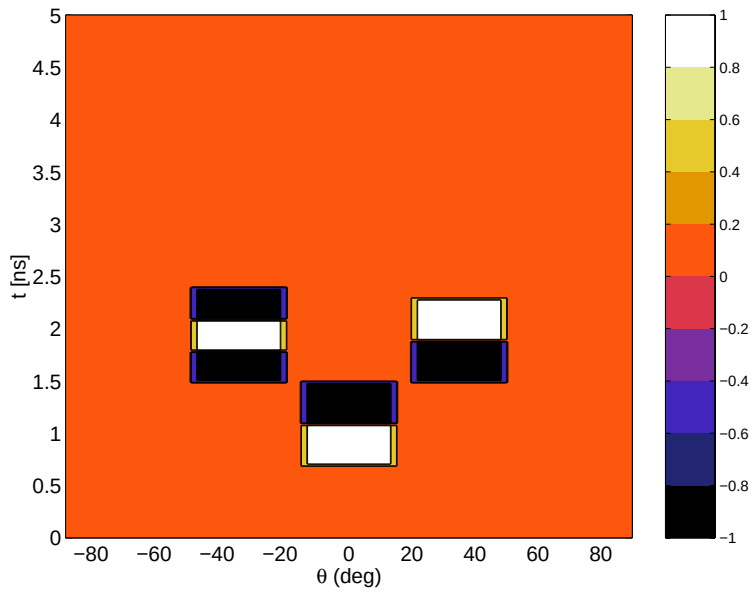

FIGURE 7.16. Time domain desired array factor of Example 2.

7.7.2 Simultaneous monocycle pulses

In the second example the synthesis addresses the only array factor (hence requiring a convoltuion operation with the element effective height to consider the radiated field). The objective array factor is shown in Fig.7.16.

The objective array factor is more complex with respect to the field of the previous example, including three groups of pulses of different shape and angular width: in fact, for some applications, it may be useful to radiate simultaneously more pulses, which can be distinguished in reception by the transient shape of the pulses themselves. Using the proposed signal representation with $K = 15$, the realized array factor is shown in Fig.7.17.

A quite good agreement can be noted with respect to the mask in Fig.7.16, despite the presence of extra oscillations with respect to the previous case, due to the increased complexity in the shape of the desired far field.

The coefficients of the final excitation projection are shown in Fig.7.18 and the related synthetized currents are presented in Fig.7.19. It can be noted that each element has a different temporal behavior and coefficient set because of the asymmetry of the desired pattern.

As for the previous example, Fig.7.20 and Fig.7.21 show the realized pattern and currents after the very first iteration of the synthesis process. In contrast with the previous example, the results of the first iteration are pretty close to the ones of the last (20th) iteration. Also the currents present a very similar transient shape. This different convergence behavior between the two example

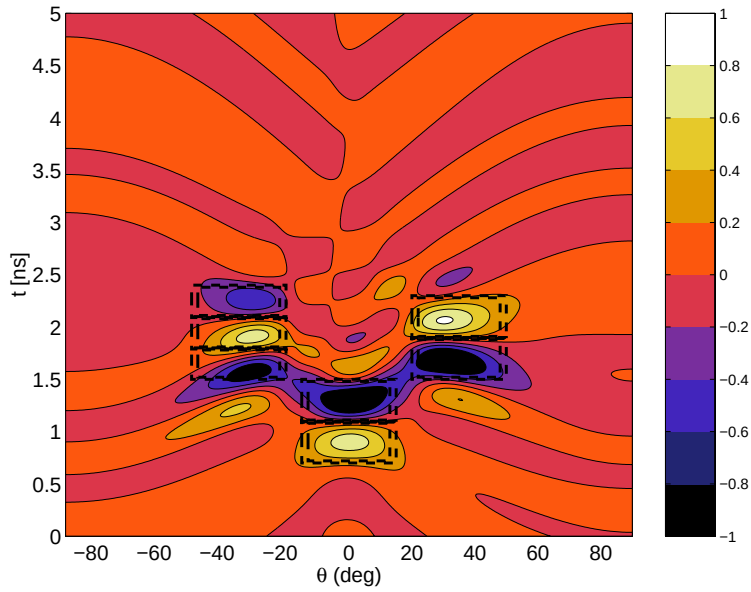

FIGURE 7.17. Realized time domain array factor of Example 2.

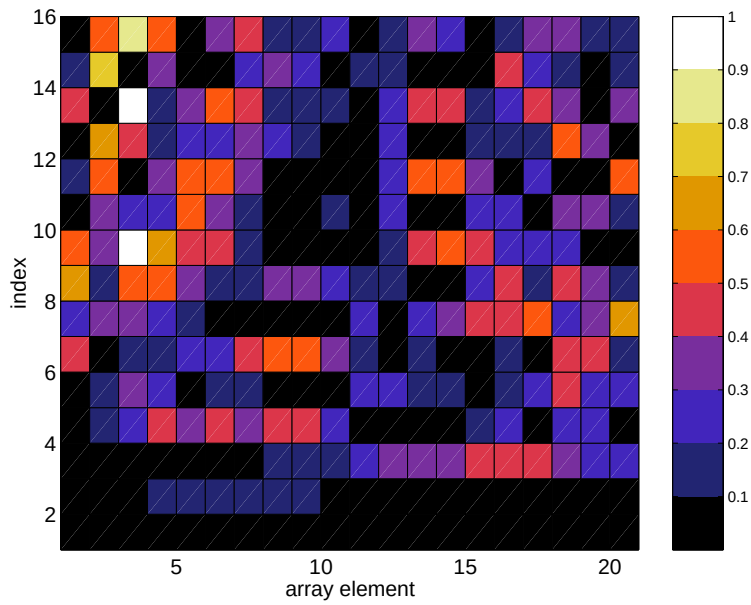

FIGURE 7.18. Set of Coefficients used for the synthesis process of Example 2.

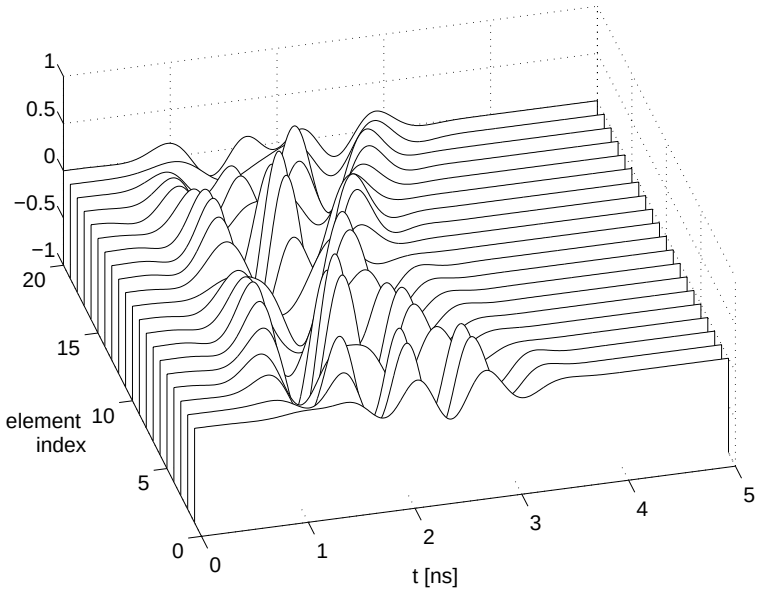

FIGURE 7.19. Realized TD input currents of Example 2.

permits to perform some assertions:

- the increased complexity of the mask in the second example probably leads to two sets $\mathcal{M}$ and $\mathcal{B}_C$ which are quite far from each other, and the solution of the first iteration already represent an element of $\mathcal{B}_C$ which is almost the closest to the set $\mathcal{M}$.
- the presence, in the first example, of the effective height of the radiating element slows down the convergence of the synthesis method, requiring more iterations to include the effects of the radiating element into the realized far field.

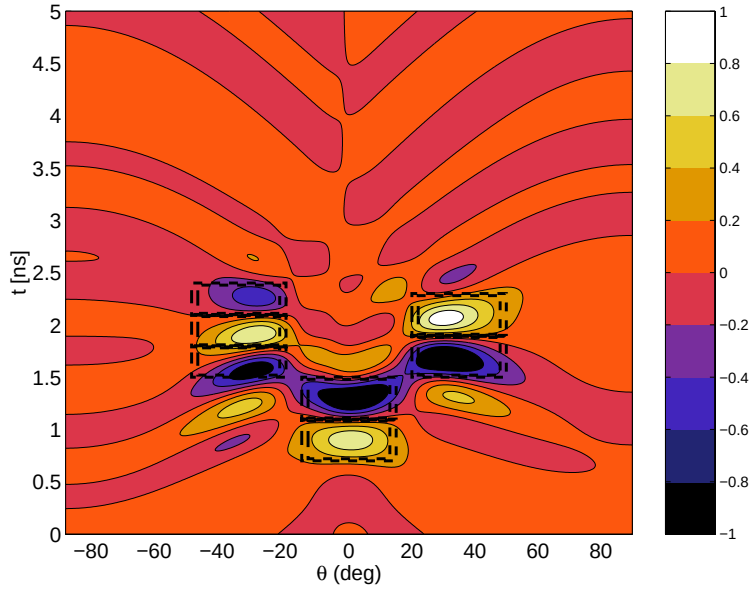

FIGURE 7.20. Realized array factor after the 1st iteration of Example 2

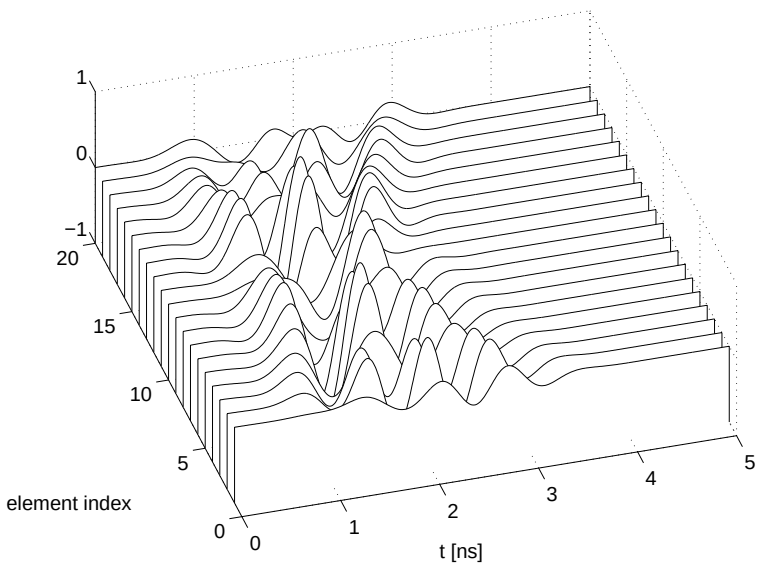

FIGURE 7.21. Realized currents after the 1st iteration of Example 2

Chapter 8

Conclusions

This report includes the work developed at the University of Rome Tor Vergata in the field of analysis and synthesis of UWB arrays, in particular in terms of efficient characterization of UWB antenna effective height, coupling among radiating elements aned synthesis of input currents in UWB arrays. The innovative results of this PhD work are summarized in this last chapter.

Effective Height The approximate numerical calculation of time-domain effective height for UWB antennas has been addressed and two new approximate compact space-time-frequency field representations for aperture antennas and moderately-directive UWB antennas have been presented. The proposed methods are fully automated combined procedures involving a local electromagnetic solver (typically FDTD) and signal processing for the manipulation of the computed near field of the antenna. By the use of suitable time- and space-fitting models (singularity expansion method for the time dependence, aperture modal eigenfunctions and Associate Hermite functions for the spatial dependencies), the burden of the effective height computation has been greatly reduced, since the coupling of temporal and spatial variables in the Radon Transform has been eliminated. The complete spatial and temporal filtering behavior of the antenna is therefore captured by a small set of parameters, expressing the antenna impulse response and transfer function by semi-analytical formulas. The proposed numerical procedures are mainly post-processing and hence they are suited to strengthen any existing time-domain numerical solver, e.g. without the need to affect the electromagnetic computation core. Due to the simplicity of the effective height formulas, the convolution with real input signals can be performed in a very efficient way, thus allowing a more efficient characterization of pulsed arrays.

Time-domain Couplings The phenomenology and the effects of ultra-wideband array couplings have been investigated through a new physical model

of the time domain coupling and expressions for the time domain active array and element patterns heve been retrieved. Under some simplifications, the interaction among multiple radiators has been described, in the case of short pulse, as superposition of multiple echoes, scattered by the antennas and superimposed to the direct signals, therefore producing distortion. This investigation has permitted to point out that the strength of the couplings depends not only on the inter-element spacing and on the scan angle but also on the antenna bandwidth and on transmitted waveforms. In particular, the distortion is more relevant for wide signals with fast repetition rate, and also increases with the reduction of the antenna bandwidth. The time-domain coupling models proposed in this work have yielded some useful relationships among the geometrical parameters (array spacing), the system bandwidth (e.g. the duration and repetition rate of the transmitted signal) and the scan angle, which could be considered in order to reduce the coupling even in the case of very dense arrays. The coupling phenomena in UWB arrays can be considered rather modest since coupling echoes generally appear at different times and therefore the overall summation is less effective than in the case of monochromatic arrays.

Time-domain synthesis of pulsed arrays A new synthesis technique to compute the amplitude, the transient behavior and the relative delay of the input signals of UWB arrays has been proposed, in order to shape the radiated field in accordance to a given mask in the angular and temporal domains. This synthesis problem is reduced to the problem of finding the intersection of sets and, in particular, the intersection among the set of all far fields which can be radiated by the given array using realizable excitation currents and the set of all the functions which fulfil a given mask requirement. In order to solve this intersection problem, the technique extends the method of alternating projections to the time domain array synthesis: in particular it consists of iterative projections of the radiated pattern onto the desired pattern mask and of the obtained excitations onto a physical set of excitations. Thanks to this second projection, the proposed technique provides input currents which are physically realizable by means of a beamforming network which will be shown in the chapter.

Appendix A

Details on aperture effective height

A.1 Details on the definition of TD aperture effective height

According to [58], the TD far-field radiation corresponding to $\boldsymbol{E}_a^{\delta}(\boldsymbol{\rho},\tau)$ aperture field is:

$$\begin{aligned}\boldsymbol{E}(\boldsymbol{r},t) = \frac{1}{2\pi rc}\hat{\boldsymbol{r}}\times \\ \frac{\partial}{\partial t}\iint\limits_{S_a}\boldsymbol{E}_a^{\delta}(\boldsymbol{\rho},t-\frac{r-\hat{\boldsymbol{r}}\cdot\boldsymbol{\rho}}{c})ds\times\hat{\boldsymbol{z}}\end{aligned} \tag{A.1}$$

Equalling (A.1) with (5.1) for $v_{in}(t) = 2R_g\delta(t)$, the expression of $\boldsymbol{h}^T$in (5.20) is formally obtained.

A.2 Calculation of the $\boldsymbol{h}_{p,\infty}^R$ integral in (5.10)

For the case of a rectangular aperture of size $a \times b$, the integral in $\boldsymbol{h}_{p,\infty}^R$ is of the form

$$\psi(\tau) = \int_{-b/2}^{b/2}\int_{-a/2}^{a/2}\delta(\tau'+\alpha x+\beta y)f(x,y)dxdy \tag{B.1}$$

with $\tau' = \tau - t_p$, $\alpha = c^{-1}\cos\phi\sin\theta$, $\beta = c^{-1}\sin\phi\sin\theta$ and $f(x,y)$ is any Cartesian component of the basis function $\boldsymbol{e}_p$. By using the properties of the Dirac function [73] and performing integration with respect to x variable, the surface integral is reduced to the following line integral:

$$\psi(\tau) = \frac{1}{|\alpha|}\int_{y_1(\tau)}^{y_2(\tau)} f(-\frac{\tau'}{\alpha} - \frac{\beta}{\alpha}y, y)dy \tag{B.2}$$

where the time-dependent integration limits are:

$$y_1(\tau) = \max\left\{-\tfrac{b}{2}, -\tfrac{\tau'}{\beta} - \tfrac{\alpha a}{2\beta}\right\} - \max\left\{-\tfrac{b}{2} - \tfrac{\tau'}{\beta} - \tfrac{\alpha a}{2\beta}, 0\right\} \tag{B.3}$$

$$y_2(\tau) = \min\left\{\tfrac{b}{2}, -\tfrac{\tau'}{\beta} + \tfrac{\alpha a}{2\beta}\right\} + \max\left\{-\tfrac{b}{2} + \tfrac{\tau'}{\beta} - \tfrac{\alpha a}{2\beta}, 0\right\} \tag{B.4}$$

Simpler expressions are anyway obtained for observation points along the principal cuts $\phi = \{0, \frac{\pi}{2}\}$. For instance, it is easy to show that in the case of $\phi = 0$ (B.1) becomes:

$$\psi(t) = \begin{cases} \frac{c}{\sin\theta}\int_{-b/2}^{b/2} f(-\frac{c\tau'}{\sin\theta}, y)dy & |\tau'| < \frac{a\sin\theta}{2c} \\ 0 & \text{otherwise} \end{cases} \tag{B.5}$$

As an example, the integral $\boldsymbol{h}_{p,\infty}^R$ at $\phi = 0$, corresponding to the TE_{10} basis function $\boldsymbol{e}_p(\boldsymbol{\rho})_{10} = \sqrt{\frac{2}{ab}}\sin(\frac{\pi}{a}x)\mathbf{y}$ is:

$$\boldsymbol{h}_{10,\infty}^R(\hat{\boldsymbol{r}}, \tau) = -\frac{1}{\mu_0}\sqrt{\frac{2b}{a}}\sin(\frac{\pi c(\tau - t_p)}{\sin\theta})\cot\theta\hat{\boldsymbol{\theta}} \tag{B.6}$$

A.3 Modal space factors

A.3.1 Modal space factors for rectangular apertures

For rectangular apertures of $a \times b$ sides, the transverse component of modal space factor, as obtained in [45] is, for TE_{mn} eigenvectors:

$$\boldsymbol{F}_{t,mn} = -4(j)^{m+n-1}T_{mn}\frac{\sin(\frac{k_x a + m\pi}{2})}{(k_m^2 - k_x^2)}\cdot\cdot\frac{\sin(\frac{k_y b + n\pi}{2})}{(k_n^2 - k_y^2)}\begin{bmatrix} k_n^2 k_x\hat{\boldsymbol{x}} \\ -k_m^2 k_y\hat{\boldsymbol{y}} \end{bmatrix} \tag{A.1}$$

with $k_m = \frac{m\pi}{a}$, $k_n = \frac{n\pi}{b}$, $k_x = k_0 r_x$, $k_y = k_0 r_y$, $r_x = \hat{\boldsymbol{x}}\cdot\hat{\boldsymbol{r}}$, $r_y = \hat{\boldsymbol{y}}\cdot\hat{\boldsymbol{r}}$ and T_{mn} is a normalization factor. Similar expressions hold for TM modes with $F_{x,mn}^{TM} = -\frac{k_m}{k_n}F_{x,mn}^{TE}$ and $F_{y,mn}^{TM} = \frac{k_n}{k_m}F_{y,mn}^{TE}$.

By taking into account the substitution of ω with $-js_{pk}$ and by using the properties $\sin(jz) = j\sinh z$ the modal space factor in spherical coordinates becomes

$$\boldsymbol{F}_{mnk} = -(j)^{m+n}\varphi_{mnk}\begin{bmatrix} \frac{k_n^2 r_x\cos\phi - k_m^2 r_y\sin\phi}{\cos\theta}\hat{\boldsymbol{\theta}} \\ -(k_n^2 r_x\sin\phi + k_m^2 r_y\cos\phi)\hat{\boldsymbol{\phi}} \end{bmatrix} \tag{A.2}$$

where:

$$\varphi_{mnk} = 4(ab)^2 \frac{s_{mnk}}{c} T_{mn} \frac{\sinh(\frac{u_{mnk}}{2} + j\frac{m\pi}{2})}{[u_{mnk}^2 + (k_m a)^2]} \cdot \cdot \frac{\sinh(\frac{v_{mnk}}{2} + j\frac{n\pi}{2})}{[v_{mnk}^2 + (k_n b)^2]})$$

with $u_{mnk} = s_{mnk} r_x a/c$ and $v_{mnk} = s_{mnk} r_y b/c$. Real-valued radiated modal field $\boldsymbol{\mathcal{E}}_{mnk} = \boldsymbol{E}_{mnk} + \boldsymbol{E}_{mn,-k}$ can be obtained by the property $\sinh(z^* + j\frac{m\pi}{2}) = (-1)^m \sinh^*(z + j\frac{m\pi}{2})$ which permits to calculate $\varphi_{mn,-k} = (-1)^{m+n} \varphi_{mnk}^*$ and finally

$$\begin{aligned} \boldsymbol{\mathcal{E}}_{mnk}(\boldsymbol{r}, t) = (-1)^{\frac{m+n+3-q}{2}} |A_{mnk}(\theta, \phi)| \frac{e^{-\alpha_{mnk}(t - \frac{r}{c})}}{\pi r c} \cdot \\ \cdot \sin\left[\omega_{mnk}(t - \tfrac{r}{c}) + \Phi_{mnk}(\theta, \phi) - \tfrac{q\pi}{2}\right] \cdot \\ \cdot \begin{bmatrix} (k_n^2 r_x \cos\phi - k_m^2 r_y \sin\phi)\hat{\boldsymbol{\theta}} \\ -(k_n^2 r_x \sin\phi + k_m^2 r_y \cos\phi)\cos\theta \hat{\boldsymbol{\phi}} \end{bmatrix}, \qquad t > t_r \end{aligned} \tag{A.4}$$

where we have posed
$s_{mnk} = -\alpha_{mnk} + j\omega_{mnk}$, $\varphi_{mnk}(\theta, \phi) a_{mnk} s_{mnk} = |A_{mnk}(\theta, \phi)| e^{j\Phi_{mnk}(\theta, \phi)}$ and $q = 1$ or 0 for even or odd $(m + n)$ respectively.

It is worth noticing that the contribute of each pole to the radiated real-valued field still shows a damped sinusoidal dependence. The field attenuates along with the distance and with time according to the pole real part. The amplitude and the oscillating phase depend on the observation points and on the pole. Nevertheless, the full separability of temporal and spatial variables is lost when moving from a complex representation $\boldsymbol{E}_{mnk}$ to real-valued $\boldsymbol{\mathcal{E}}_{mnk}$.

A.3.2 Modal space factors for circular apertures

For circular aperture antennas of radius A, the computation of pattern space factors can be derived from [59]:

$$\begin{aligned} \boldsymbol{F}_{mn}(k_0, \theta, \phi) = -j2\pi A T_{mn} \Bigg\{ \frac{1}{\cos\theta} [b_{mn} j^m m J_m(p'_{mn}) \frac{J_m(u)}{u} \\ -(b_{mn} - 1) j^m p_{mn} J'_m(p_{mn}) \frac{u J_m(u)}{p_{mn}^2 - u^2}] \sin m\phi \hat{\boldsymbol{\theta}} + \\ + [b_{mn} j^m p'^2_{mn} J_m(p'_{mn}) \frac{J'_m(u)}{p'^2_{mn} - u^2}] \cos m\phi \hat{\boldsymbol{\phi}} \Bigg\} \end{aligned} \tag{A.5}$$

with $u = k_0 A \sin\theta$, $b_{mn} = \left\{ \begin{smallmatrix} 1 & TE \\ 0 & TM \end{smallmatrix} \right.$, T_{mn} is a normalization constant, p_{mn} the n-th zero of Bessel function J_m and p'_{mn} the n-th zero of its first derivative. Substitution of ω with $-js_{mnk}$ (and therefore $u_{mnk} = -j\frac{s_{mnk}}{c} A \sin\theta$) gives the radiated TE modal field:

$$E_{mnk,\theta} = L_{mnk}\frac{e^{s_{mnk}(t-\frac{r}{c})}}{r}\frac{\sin m\phi}{\sin\theta}J_m(u_{mnk})U(t-\frac{r}{c}) \tag{A.6}$$
$$E_{mnk,\phi} = M_{mnk}\frac{e^{s_{mnk}(t-\frac{r}{c})}}{r}\cos m\phi\cos\theta\cdot\frac{J'_m(u_{mnk})}{p'^2_{mn}-u^2_{mnk}}U(t-\frac{r}{c})$$

with $M_{mnk} = -j^{m+1}s_{mnk}a_{mnk}/cAT_{mn}p'^2_{mn}J_m\left(p'_{mn}\right)$, and $L_{mnk} = mj^mT_{mn}s_{mnk}a_{mnk}/cJ_m\left(p'_{mn}\right)$. The property $J_m(-jz^*) = (-1)^mJ^*_m(-jz)$ permits to obtain a real-valued expression similar to (A.4). The extension to TM is straightforward.

Bibliography

[1] K. Siwiak, D. McKeown, "Ultra-wideband radio technology", John Wiley & Sons, 2004

[2] M. Ghavami, L.B. Michael, R. Kohno, "Ultra-wideband signals and systems in communication engineering", John Wiley & Sons, 2004

[3] K. Siwiak, "Ultra-Wide Band Radio: Introducing a New Technology", ...

[4] C.L. Bennett, G.F. Ross, "Time-Domain Electromagnetics and Its Applications", Proceedings of the IEEE, Vol.66, N.3, 1978, pp.299-321

[5] R.J. Fontana, "Recent System Applications of Short-Pulse Ultra-Wideband (UWB) Technology", IEEE Transactions on Microwave Theory and Techniques, Vol.52, N.9, 2004, pp.2087-2104

[6] FCC First Report and Order, ET Docket 98-153

[7] http://www.aetherwire.com/

[8] http://www.ubisense.net

[9] I.Y. Immoreev, J.D. Taylor, "Ultrawideband Radar Special Features & Terminology", IEEE A&E Systems Magazine, May 2005, pp.13-15

[10] K.S. Yee, "Numerical solution of initial boundary value problems involving Maxwell's equations in isotropic media", *IEEE Trans. Antennas Propagat.* vol. 14, N.5, pp. 302-307, May. 1966.

[11] A. Taflove, Advances in Computational Electromagnetics: The Finite Difference Method, Norwood, MA, Artech House, 1998

[12] J. B. Martens, "The Hermite transform: Theory", *IEEE Trans.on Acustic Speech and Signal Processing,* Vol.38, pp.1595-1606, Sept. 1990.

[13] J. B. Martens, "The Hermite transform: Applications", *IEEE Trans.on Acustic Speech and Signal Processing,* Vol.38, pp.1607-1618, Sept. 1990.

[14] L.R. Lo Conte, R. Merletti, G.V. Sandri, "Hermite Expansions of Compact Support Waveforms: Applications to Myoelectric Signals", *IEEE Trans. on Biomedical Engineering*, Vol.41, N.12, pp.1147-1159, 1994.

[15] A. Bogush JR., R. Elkins, "Gaussian field expansions for large aperture antennas", *IEEE Trans. Antennas Propagat.* vol. 34 N.2, pp. 228-243, Feb. 1986.

[16] L.E. Miller, "Autocorrelation functions for Hermite-polynomial ultra-wideband pulses", *Electronics Letters*, Vol.39, N.11, pp.870-871, 2003.

[17] P.Toft, "The Radon Transform - Theory and Implementation", Ph.D. Thesis, Technical University of Denmark, 1996

[18] G. Beylkin, "Discrete Radon Transform", *IEEE Trans. on Acoustics, Speech and Signal Processing*, Vol.35, N.2, pp.162-172, 1987.

[19] R.M. Mersereau, A.V. Oppenheim, "Digital Reconstruction of Multidimensional Signals from Their Projections", Proc. of the IEEE, Vol.62, N.10, 1974, pp.1319-1347

[20] G. Marrocco, F. Bardati, "FDTD computation of a microwave device impulse response", Electronics Letters, vol.35, n.3, 1999, pp.223-224

[21] D. Lamensdorf, L. Susman, "Baseband-pulse-antenna techniques", IEEE Antennas Propagation Magazine, vol.36, n.1, pp.20-30, 1994

[22] M. G. M. Hussain, "Principles of space-time array processing for ultrawideband impulse radar and radio communications," IEEE Trans. Veh. Technol., vol. 51, no. 3, pp. 393-403, 2002

[23] A. Shlivinski, E. Heyman, "A unified kinematic theory of transient array," in Ultra-Wideband, Short-pulse Electromagnetics 5, P.D Smith and S.R. Cloude Eds., Kluwer Academic/Plenum Publishers, NY, 2002, pp.11-20

[24] L. D. DiDomenico, "A comparison of time versus frequency domain antenna patterns," IEEE Trans. Antennas Propag., vol. 50, no. 11, pp.1560-1566, 2002.

[25] J. L. Schwartz, B. D. Steinberg, "Ultrasparse, ultrawideband arrays", IEEE Trans. Ultrason., Ferroelectr. Freq. Control, vol. 45, no. 2, pp.376-393, 1998.

[26] M.Ciattaglia, G. Marrocco, "Investigation on Antenna Coupling in Pulsed Arrays", IEEE Transactions on Ant. and Prop., Vol.54, N.3, 2006, pp.835-843

[27] W. Sorgel, C. Sturm, W. Wiesbeck, "Impulse Response of Linear UWB Antenna Arrays and the Application to Beam Steering", pp.275-280

[28] D.M. Pozar, Y. Kang, D.H. Schaubert, R.E. McIntosh, "Optimization of the Transient Radiation from a Dipole Array", IEEE Transactions on Ant. and Prop., Vol.33, N.1, 1985, 69-75

[29] Y. Kang, D.M. Pozar, "Optimization of Pulse Radiation from Dipole Arrays for Maximum Energy in a Specified Time Interval", IEEE Transactions on Ant. and Prop., Vol.34, N.12, 1986, 1383-1390

[30] R. Prony, "Essai experimental et analytique sur les lois de la dilatabilite de fluides elastiques et sur celles del la force expansive de la vapeur de l'alkool a differentes temperatures", Paris J. l'Ecole Polytech., vol.1, 1795, pp.24-76

[31] Y. Hua, T.K. Sarkar, "Matrix Pencil Method for estimating parameters of exponentially damped/undamped sinusoids in noise", IEEE Trans. Acoust., Speech, Signal Processing, Vol.38, 1990, pp.814-824

[32] C.E. Baum, "The singularity expansion method", in Transient Electromagnetic Fields, L.B. Felsen Editor, Springer-Verlag, Berlin 1976.

[33] B.T. Kelley, V.K. Madisetti, "The Fast Discrete Radon Transform-I: Theory", IEEE Transactions on Image Processing, Vol.2, N.3, 1993, pp.382-400

[34] C. Balanis, *Antenna Theory, Analysis and Design*, New York, J. Wiley & Sons, 1997

[35] M. Ciattaglia, G. Marrocco, "Approximate calculation of time-domain effective height for aperture antennas", IEEE Trans. on Antennas and Propagation, Vol.53, N.3, pp.1054-1061, 2005

[36] C.C. Oetting, L. Klinkenbusch, "Near-to-far-field transformation by a time-domain spherical-multipole analysis", IEEE Trans. on Antennas and Propagation, Vol.53, N.6, pp.2054-2063, 2005

[37] A. Shlivinski, E. Heyman, and R. Kastner, "Antenna characterization in the time domain," IEEE Trans. Antennas Propag., Vol. 45, 1997, pp.1140-1149

[38] A. Papoulis, Signal analysis, Mc Graw Hill, NY, 1977

[39] A. Taflove, "Computational electrodynamics: The finite difference time domain method" Artech House, Norwood, MA, 1995.

[40] K.A. Remley, A. Weisshar, S.M. Goodnick, V.K. Tripathi, "Characterization of near- and far-field radiation from ultrafast electronic systems", *IEEE Trans. on Microwave Theory and Techniques*, vol. 46, pp. 2476-2483, 1998.

[41] C. Oetting, L. Klinkenbusch, "Improving the accuracy of numerical results by a spherical-multipole based post-processing", in *Proc. IEEE AP-S - International Symposium*, San Antonio 2002, pp. 44-47.

[42] I.J. Craddock, P.G. Turner, C.J Railton "Reducing the computational overhead of the near-field transform through system identification", *Electronics Letters*, vol. 30, pp. 1609-1610, 1994.

[43] D. Sullivan, J.L. Young, "Far-field time-domain calculation from aperture radiators using the FDTD method", *IEEE Trans.Antennas Propagat*, vol. AP-49, pp. 464-469, 2001.

[44] S. Licul, W.A. Davis, "Unified Frequency and Time-Domain Antenna Modeling and Characterization", *IEEE Trans.Antennas Propagat*, vol. AP-53, N.9, pp. 2882-2888, 2005.

[45] G. Marrocco, "Modal near-field to far-field transformation for FDTD modelling of aperture antennas", *J. of Electromagn. Waves and Appl.*, vol. 17, pp. 79-98, 2003.

[46] G. Marrocco, M. Ciattaglia, Ultra-wide band modelling of transient radiation from aperture antennas", *IEEE Trans. Antennas Propagat.* vol. 52, pp. 2341-2347, Sep. 2004.

[47] D. R. Rhodes, *Synthesis of planar antenna sources*, Clarendon Press, Oxford, 1974.

[48] C.E. Baum, "Toward an engineering theory of electromagnetic scattering: the singulariry and eigenmode expansion methods", in *Electromagnetic Scattering*, P.L.E. Uslenghi editor, Academic Press, New York 1978, pp.571-651.

[49] L.W. Pearson, R. Mittra, "The singularity expansion representation of the transient electromagnetic coupling through a rectangular aperture", *Interaction Notes,* Note 296, June 1976.

[50] C.D. Taylor, T.T. Crow, K.T. Chen, "On the singularity expansion method applied to aperture penetration: Part I theory", *Interaction Notes,* Note 134, May 1973.

[51] B. N. Das, A. Chakraborty, S. Gupta, "Analysis of waveguide-fed thick radiating rectangular windows in a ground plane", *IEE Proc.Microwaves, Antennas and Propag.*, Vol. 138, N.2, pp.142-146, 1991.

[52] R. Bunger, R. Beyer, F. Arndt, "Rigorous combined mode-matching integral equation analysis of horn antennas with arbitrary cross section", *IEEE Trans.Antennas Propagat.*, vol. 47, N. 11, pp. 1641-1648, 1999.

[53] A.Q. Howard Jr, "A comparison of mode match, geometrical theory of diffraction and Kirchhoff radiation", *IEEE Trans.Antennas Propagat.*, vol. 21, N. 11, pp. 100-102, 1973.

[54] E.K. Miller, "Model-based parameter estimation in electromagnetics: part I. Background and theoretical development", *IEEE Antennas and Propagat. Magazine*, Vol.40, N.1, pp.42-52, 1999.

[55] E. Heyman, L.B. Felsen, "A wavefront interpretation of the singular expansion method", *IEEE Trans.Antennas Propagat.*, vol. 33, N. 7, pp. 706 -718, 1985.

[56] L.W. Pearson, "A note on the representation of scattered fields as a singular expansion", *IEEE Trans.Antennas Propagat.*, vol. 32, N. 5, pp. 520-524,1984.

[57] A. Poggio, M. VanBlaricum, E. Miller, R. Mittra, "Evaluation of a processing technique for transient data", *IEEE Trans.Antennas Propagat.*, vol. 26, N. 1, pp. 165-173, 1978.

[58] T. B. Hansen, A. D. Yaghjian, "Planar near-field scanning in the time domain, Part 1: formulation", *IEEE Trans.Antennas Propagat.*, vol. 42, pp. 1280-1291, 1994.

[59] A.C. Ludwig, "Radiation pattern synthesis for circular aperture horn antennas", *IEEE Trans. Antennas Propagat.* vol. 14, pp. 434-440, 1966.

[60] G. Marrocco, F. Bardati, "Broadband Horn-Antenna Launchers Modelling by FDTD and Generalized Scattering Matrix Methods", *IEEE Trans. Antennas Propagat.*, vol. 50, pp. 1688-1696, 2002.

[61] S.D. Gedney, "An anisotropic PML absorbing media for FDTD simulation of fields in lossy dispersive media", *Electromagnetics* vol. 16, pp. 399-415, 1996.

[62] G.A. Lovisolo, M. Adami, G. Arcangeli, A. Borrani, "A Multifrequency Water-filled Waveguide Application Thermal Dosimetry In Vivo", *IEEE Trans. Microwave Theory Tech.*, vol. 32, pp. 893-896, 1984.

[63] W.A. van Cappellen, R.V. de Jongh, L.P. Ligthart, "Potentials of Ultra-Short-Pulse Time-Domain Scattering Measurements", *IEEE Antennas and Propagation Magazine*, vol. 42, pp. 35-45, 2000.

[64] E. G. Farr, C. E. Baum, "Extending the definition of antenna gain and radiation pattern into the time domain", Sensor and Simulation Notes, Note 350, Nov. 1992.

[65] O. E. Allen, D. A. Hill, A. R. Ondrelka, "Time domain antenna characterization", IEEE Trans. Electromagn. Compat., Vol.35, pp.339-345, 1993

[66] B. Scheers, M. Acheroy, A. Vander Vorst, "Time-domain simulation and characterisation of TEM horns using a normalised impulse response", IEE Proc. Microw. Antennas Propagat., Vol.147, pp.463-468, Dec. 2000

[67] W. Sorgel, C. Waldschmidt, W. Wiesbeck, "Electromagnetic characterization of ultra wideband antennas", in Electromagnetics in a Complex World, I.M. Pinto, V. Galdi, L.B. Felsen Eds, Springer-Verlag, Berlin 2004, pp.225-234.

[68] D.V. Giri, C.E. Baum, "Reflector IRA design and boresight temporal waveforms", Sensor and Simulation Notes, Note 365, Feb. 1994.

[69] S. P. Skulkin, V.I. Turchin, "Transient field calculation of aperture antennas", IEEE Trans.Antennas Propagat., vol. 47 N.5, pp. 929-932,1999.

[70] G. Marrocco, F. Bardati, " Time-domain macromodel of planar microwave devices by FDTD and moment expansion", IEEE Trans. Microwave Theory Tech, Vol. 49, pp.1321-1328, 2001.

[71] T.K. Sarkar, O. Pereira, "Using the Matrix Pencil method to estimate the parameters of a sum of complex exponentials", IEEE Antennas and Propagat. Magazine, Vol.37, N.1, pp.48-55, 1995.

[72] W.H. Press, S. Teukolsky, W.T. Vetteriling, B.P.Flannery,"Numerical Recipies in C - the art of scientific computing", Cambrige University Press, Cambrige (MA), 1992

[73] E. W. Weisstein "CRC Concise Encyclopedia of Mathematics", Chapman & Hall/CRC pp.129-179.

[74] Kogelnik H. T. Li, "Laser beams resonators", *Appl. Opt.*, Vol.5, No.10, pp. 1550-1567, Oct.1966.

[75] R.K.Arora, Zhong Lu, "Graphical depiction of the electromagnetic fields of Hermite-Gaussian modes", *IEE Proceed. Microwaves, Antennas and Propagation H*, Vol.139, N.4, pp.369-375, Aug. 1992.

[76] M.M. Rao, T.L. Sarkar, T. Anjali, R.S. Adve, "Simultaneous extrapolation in time and frequency domains using hermite expansions", *IEEE Trans. Antennas Propagat.* Vol. 47, N. 6, pp. 1108-1115, June 1999

[77] F. Bardati, E. Di Giampaolo, A. Durantini, G. Marrocco,"Vertical antenna near-field computation in complex environmentd by an hybrid method", *Proceedings of Applied Computational Electromagnetics Conference (ACES)*, pp.975-980, Monterey (USA) 2000.

[78] A.D. Yaghijan, "An overview of near-field antenna measurements", *IEEE Trans. Antennas Propagat.* Vol.34, pp.30-45, Jan. 1984.

[79] N.P. Agrawall, G. Kumar, K.P. Ray, "Wide-band planar monopole antennas" *IEEE Trans.Antennas Propagat* vol.46, pp.294-295, Feb. 1998.

[80] D.M. Pozar, "The active element pattern", *IEEE Trans. Antennas and Propagat.*, Vol. 42, N.8, pp. 1176-1178, 1994

[81] G. Marrocco, F. Capolino, "Transient Radiation by Periodic Structures: Accuracy of the (Time Domain–Floquet Wave)-FDTD Algorithm", *IEEE Antennas and Propagation Society Symposium*, Vol.3, pp.643-646, San Antonio (USA), 2002.

[82] G. Marrocco, F. Capolino, "A Combined Floquet-Wave - FDTD Algorithm for the Modeling of Transient Radiation from Infinte Periodic Structures", in *Electromagnetics in a Complex World: Challenges and Perspectives*, pp. 249-257, Springer-Verlag, 2004.

[83] G. Marrocco, F. Bardati, "BEST: a finite-difference solver for time electromagnetics", *Simulation Practice Theory* ,vol. 7, pp. 279-293, Jul. 1999.

[84] E.J. Bond, X. Li, S.C. Hagness, B.D. Van Veen, "Microwave imaging via Space-Time Beamforming for Early Detection of Breast Cancer", *IEEE Trans. Ant. Prop*, Vol. 51, N. 8, pp. 1690-1705, August 2003.

[85] O.M. Bucci, G. Franceschetti, G. Mazzarella, G. Panariello, "Intersection approach to array pattern synthesis", *IEE Proceedings*, Vol. 137, Pt. H, N. 6, pp. 349-357, December 1990.

Publications, Conferences, Awards

International Journals Contributions

G. Marrocco, M. Ciattaglia, "Ultra-wide Band modelling of transient radiation from aperture antennas", IEEE Trans. On Antennas and Propagation, Vol.52, N.9, September 2004

M. Ciattaglia, G. Marrocco, "Approximate Calculation of time-domain effective height for aperture antennas", IEEE Trans. On Antennas and Prop., Vol.53, N.3, March 2005

M. Ciattaglia, G. Marrocco, "Investigation on Antenna Coupling in Pulsed Arrays", IEEE Transactions on Ant. and Propagation Vol.54, N.3, March 2006

G. Marrocco, M. Migliorelli, M. Ciattaglia, "Simultaneous Time-Frequency Modeling of Ultra-Wideband Antennas by Two-Dimensional Hermite Processing", Progress in Electromagnetics Research, PIER 68, 317-337, 2007

National Journal Contribution

M. Ciattaglia, G. Marrocco, "Calcolo della altezza efficace di antenne ad apertura per applicazioni UWB", Quaderni di Elettromagnetismo 2005

Book Chapter

M. Ciattaglia, G. Marrocco, "On the efficient numerical time-domain processing of aperture antenna field", to be published on UWB Short Pulse Electromagnetics, Kluwer Plenum Publisher

International congress contributions

G. Marrocco, M. Ciattaglia, "Broadband modelling of waveguide antennas by a combined FDTD and Modal-N2F method", Applied Computational Electromagnetics Conference 2003, Monterey, pp. 217-222

G. Marrocco, M. Ciattaglia, "Modelling of ultra-wide band radiation from horn antennas: a numerical-analytical approach", ICEAA 2003, Torino, pp.233-236

G. Marrocco, M. Ciattaglia, "Ultra-wideband radiation from aperture antennas: a simultaneous time- and frequency-domain modelling", ICECOM 2003, Dubrovnic

G. Marrocco, M. Ciattaglia, "Advanced ultra-wideband numerical-analytical modelling of aperture antennas", 26th ESA Antenna Technology Workshop on Satellite Antenna Modelling and Design Tools 2003, pp.213-219

M. Ciattaglia, G. Marrocco, "Efficient Calculation of Time-Domain Radiation Integral by means of data-fitting and signal processing tools", Progress in Electromagnetics Research Symposium (PIERS), Pisa, 2004

M. Ciattaglia, G. Marrocco, "Fast Calculation of Time Domain Effective Height of Ultra-Wide Band Aperture Antennas", Progress in Electromagnetics Research Symposium (PIERS), Pisa, 2004

M. Ciattaglia, G. Marrocco, "Transient radiation from aperture antennas: efficient calculation of time-domain effective height", URSI, Pisa, 2004

M. Ciattaglia, G. Marrocco "Combining data-fitting and signal processing for efficient time-domain characterization of aperture antennas", 20th Annual Review of Progress in Applied Computational Electromagnetics, Syracuse NY, 2004

M. Ciattaglia, G. Marrocco, "Advanced Time-Domain Processing of Aperture Antenna Field" IEEE AP-S International Symposium, Monterey, California, 2004

M. Ciattaglia, G. Marrocco, "On the efficient numerical time-domain processing of aperture antenna field", EUROEM 2004, Magdeburgh, 2004

M. Migliorelli, M. Ciattaglia, G. Marrocco, "Efficient modeling of Ultra-wideband antennas by two-dimensional Hermite processing", IEEE AP-S International

Symposium, Washington, 2005

M. Ciattaglia, G. Marrocco, "Investigation on Antenna Coupling in Pulsed Arrays", IEEE AP-S International Symposium, Washington, 2005

G. Marrocco, M. Ciattaglia, "Signal Distortion in Ultra-Wideband Arrays", EMC Europe Workshop, Rome, 2005

M. Migliorelli, M. Ciattaglia, G. Marrocco, "Application of the Two-dimensional Hermite Processing to the UWB Antenna Modeling", ICEAA 2005, Torino, 2005

M. Ciattaglia, S. Mosca, "Broadband broadside characterization of periodic arrays with triangular lattice", ICEAA 2005, Torino, 2005

M. Ciattaglia, L. Infante, S. Mosca, M. Albani, A. Crisafulli, "A new near field array focusing technique for radar system testing", AMTA 2006, Monaco, 2006

M. Ciattaglia, G. Marrocco, "Investigation on Antenna Coupling in Pulsed Arrays", IEEE AP-S International Symposium, Albuquerque, 2006

S. Mosca, M. Ciattaglia, "Array Thinning Using Ant Colony Optimization", IEEE AP-S International Symposium, Albuquerque, 2006

S. Mosca, M. Ciattaglia, "Array Thinning Using Ant Colony Optimization", 23rd Annual Review of Progress in Applied Computational Electromagnetics 2007, Verona

M. Ciattaglia, L. Infante, A. Crisafulli, M. Albani, " Near field techniques for radar synthetic environment simulator", ICEAA, Torino, 2007

M.Ciattaglia, G. Marrocco, "Time-Domain Synthesis of Pulsed Arrays", EUCAP, Edinburgh, 2007

D. Tallini, A. Galli, M. Ciattaglia, L. Infante, A. De Luca, "A new low-profile wide-scan phased array for UWB applications", EUCAP, Edinburgh, 2007

National congress contributions

M. Ciattaglia, "Modelli ultra-wideband per la radiazione transitoria da antenne ad apertura", Riunione SIEM, Trento, 2003

M. Ciattaglia, G. Marrocco, "Modelli numerici per la caratterizzazione di antenne a banda ultralarga", II Giornata per la Geoinformazione, 2004

M. Ciattaglia, G. Marrocco, "Calcolo della altezza efficace di antenne ad apertura per applicazioni UWB", XV RiNEm, Cagliari, September 2004

M. Ciattaglia, "Analisi e Sintesi di antenne a banda larga e ultra larga", Riunione SIEM, Torino, 2005

M. Ciattaglia, G. Marrocco, "Sintesi di array UWB nel dominio del tempo", XVI RiNEm, Genova, September 2006

M. Ciattaglia, L. Infante, S. Mosca, M. Albani, A. Crisafulli, "A New Near Field Array Focusing Technique for Radar system testing", XVI RiNEm, Genova, September 2006

Technical Reports

G. Marrocco, M. Ciattaglia, "Advanced FDTD tools for wideband modelling of horn antennas", Tech. Rep., Universit degli Studi di Roma Tor Vergata, RR-02-35, November 2002

Awards

Mario Sannino Award for the best scientific presentation during the XV National Meeting on Electromagnetics, RiNEm, Cagliari, Sept. 2004

Best Student Paper during the First European Antenna Measurement Technique Association (AMTA) Symposium, Monaco, May 2006

Acknowledgments

In questi tre anni e mezzo (nota, parlo ancora del dominio del tempo!) di lavoro di tesi di dottorato, sono stato davvero un tipo casa-chiesa-lavoro-università (l'ordine è *rigorosamente* alfabetico). E in questi luoghi ho conosciuto tante persone, che davvero vorrei ringraziare!

Il primo grazie va a Gaetano Marrocco, per la sua disponibilità e pazienza nell'accettare questa collaborazione anche senza la mia presenza costante lì all'università, per essermi venuto incontro con appuntamenti fuori dagli *orari di lavoro*. E poi grazie perché è un onore ricevere consigli e proposte da te, un piacere scambiare opinioni e idee, di elettromagnetismo, ma anche di letteratura e musica! Il gruppo di antenne dell'università, poi, ha reso piacevole ogni mio passaggio post-lavorativo in laboratorio! Il Prof. Bardati, che, nei rari incontri avuti, con poche parole mi ha saputo sempre incoraggiare (anche se, lo so, non le è mai piaciuto il mio modo di presentare!). Emidio Di Giampaolo, grande!, davvero la persona con cui riesco a parlare (io, che non parlo mai..) di qualsiasi argomento con vero piacere. Lorenzo Mattioni, belle le trasferte fatte insieme, ho sempre un bel ricordo della passeggiata al porto di Cagliari. E poi tutte le persone che sono passate per il laboratorio, da Alessandro Fonte (il boss del laboratorio quando sono entrato da tesista e ora mitico collega), a Maria Pia, Emiliano, Marzia; i tesisti Alessandro (da Messina), Antonio, Federica, Giuseppe, che mi hanno permesso di cambiare un po' argomento (a volte il time domain diventava un'ossessione).

Se da una parte c'era il laboratorio dell'università che mi vedeva passare di tanto in tanto a pomeriggio inoltrato, dall'altra c'era (e c'è tuttora, per fortuna) un altro laboratorio di antenne, presso SELEX-SI, nel quale passo le mie 9-10 ore quotidiane (sabato e domenica esclusi) e dove ho la fortuna di essere a contatto con persone di tutti i tipi, ma ognuna in grado sempre di essere preziosa: per l'interesse mostrato per gli argomenti del mio dottorato, per avermi permesso delle trasferte (che all'università forse mi sarei sognato...), per l'esperienza che tante persone stanno cercando di *passarmi*, per il fatto che le tante equazioni viste all'università in SELEX le sto piano piano vedendo non più solo su carta...

Uscito dal lavoro, dopo un salto all'università, come non si poteva passare in oratorio? Lì, e in Chiesa, naturalmente, è stato possibile ritrovare ogni

volta la volontà di continuare a fare mille cose, cercando di farne ciascuna al meglio. E allora grazie a tutte le persone che sono passate per la parrocchia San Gerardo Maiella, i Don, i parrocchiani (TUTTI!), ma soprattutto l'OSGM, l'oratorio con tutti gli animatori e i bambini: davvero continuo a meravigliarmi come tutti problemi di elettromagnetismo, di antenne, di lavoro possano essere dimenticati così facilmente con un ban! CICORIA!!!!

E poi le persone più care, la mia famiglia! Mamma e papà, grazie!, perchè mi avete permesso di fare tutto questo, aiutandomi continuamente e facilitandomi la vita al di fuori dei miei impegni, e spesso senza ricevere tanti grazie. In particolare... Papà, dal quale penso proprio di aver ereditato questa cavolo di passione per la ricerca (anche se ancora non capisco come si possa ottenere un mondo migliore dalle antenne...). Anche se tra Oxford, Monaco e Aux En Provence, so che ci sei! Mamma, onnipresente!, grazie perchè quotidianamente hai davvero pensato tu a tutto, non facendomi mai mancare niente...che dire, mamma??? Manu, anche se lontano, anche tu come papà sei stata (e sei) sempre presente e interessata e prodiga di consigli per tutto ciò che faccio! Grazie! Laura, mia moglie, dolce sorgente delle mie distrazioni...per fortuna che ci siamo sposati solo pochi mesi fa, altrimenti non sarei di certo riuscito a finire la tesi!!! Grazie, amore!